The Study of Ohmic Contacts to Nitrogen-doped Nanocarbon Layers and Diamond Surfaces

by

Evangeline Abena Amonoo

A Dissertation Presented in Partial Fulfillment
of the Requirements for the Degree
Doctor of Philosophy

Approved April 2023 by the
Graduate Supervisory Committee:

Terry L. Alford, Co-Chair
Trevor Thornton, Co-Chair
Shahriar Anwar
David Theodore

ARIZONA STATE UNIVERSITY

May 2023

ABSTRACT

Over the past few years, research into the use of doped diamond in electronics has seen an exponential growth. In the course of finding ways to reduce the contact resistivity, nanocarbon materials have been an interesting focus. In this work, the transfer length method (TLM) was used to investigate Ohmic contact properties using the tri-layer stack Ti/Pt/Au on nitrogen-doped n-type conducting nano-carbon (nanoC) layers grown on (100) diamond substrates. The nanocarbon material was characterized using Secondary Ion Mass Spectrometry (SIMS), Scanning electron Microscopy (SEM) X-ray diffraction (XRD), Raman scattering and Hall effect measurements to probe the materials characteristics. Room temperature electrical measurements were taken, and samples were annealed to observe changes in electrical conductivity. Low specific contact resistivity values of 8 x 10^{-5} Ωcm^2 were achieved, which was almost two orders of magnitude lower than previously reported values. The results were attributed to the increased nitrogen incorporation, and the presence of electrically active defects which leads to an increase in conduction in the nanocarbon. Further a study of light phosphorus doped layers using similar methods with Ti/Pt/Au contacts again yielded a low contact resistivity of about 9.88 x 10^{-2} Ωcm^2 which is an interesting prospect among lightly doped diamond films for applications in devices such as transistors. In addition, for the first time, hafnium was substituted for Ti in the contact stack (Hf/Pt/Au) and studied on nitrogen doped nanocarbon films, which resulted in low contact resistivity values on the order of 10^{-2} Ωcm^2. The implications of the results were discussed, and recommendations for improving the experimental process was outlined. Lastly, a method for the selective area growth of nanocarbon was developed and studied and the results provided an insight into how different characterizations can be used

to confirm the presence of the nanocrystalline diamond material, the limitations due to the film thickness was explored and ideas for future work was proposed.

DEDICATION

To my beloved late sister, friend, and partner-in-crime.

ACKNOWLEDGMENTS

My greatest gratitude goes to God for the grace he bestowed upon me from the beginning until the completion of this research. A very sincere thank you goes to my supervisors, Dr. Trevor Thornton and Dr. Terry Alford for their tireless guidance and encouragement which made this project a success. I wish you the best of God's blessings. I also wish to express immense appreciation to Dr. Shahriar Anwar for his unwavering support and mentoring ever since I started my graduate study, and to Dr. David Theodore for his recommendations and help with the projects. I am also grateful to all the professors I have crossed paths with over the years especially Dr. Benjamin Agyei-Tuffour of the University of Ghana for believing in me ever since we crossed paths. I also want to thank my colleagues Vishal Jha and Banashree Gogoi whom I have been working with on parallel projects for the entire duration. Finally, my gratitude goes to my family and to my wonderful partner for the support and tremendous encouragement.

This research was supported by DARPA through grant FA8650-22-C-7203 and a heartfelt thank you goes to Dr. Ugonna C. Ohiri of Northrop Grumman Mission Systems, the Nanofab and AEP cores, and Eyring Materials Center of Arizona State University for providing processing facilities and measurement tools. These core facilities at ASU are supported, in part, by NSF award ECCS-2025490.

TABLE OF CONTENTS

Page

LIST OF TABLES ix

LIST OF FIGURES x

LIST OF ABBREVIATIONS xv

CHAPTER

1 INTRODUCTION 1

1.1 Background 1

1.2 Doping of Diamond 3

1.3 The Transfer Length Method 6

1.4 Objectives of the Study 8

1.5 Scope of Dissertation 8

1.6 References 9

2 OHMIC CONTACTS TO NITROGEN-DOPED NANOCARBON LAYERS ON DIAMOND (100) SURFACES 12

2.1 Introduction to Nanocarbons 12

2.2 Materials and Experimental Tools Used 15

2.3 Experimental Process 16

2.4 Results and Discussion 20

2.4.1 SIMS Results 20

2.4.2 SEM Analysis 21

2.4.3 XRD Analysis 22

2.4.4 Raman Analysis 24

2.4.5 Hall Effect Analysis....26

2.4.6 Optical Eicroscopy and SEM of TLM Contacts....28

2.4.7 I-V Characteristics Analysis....29

2.5 Conclusion....39

2.6 References....40

3 LOW CONTACT RESISTIVITY OF LIGHTLY PHOSPHORUS-DOPED DIAMOND LAYER.... 43

3.1 Performance of Phosphorus Doped Diamond....43

3.2 Heavy Versus Light Phosphorus Doping....44

3.3 Materials and Experimental Tools Used....46

3.4 Experimental Procedure....46

3.5 Experimental Results and Discussion....50

3.5.1 SIMS Analysis....50

3.5.2 IV Measurement and Analysis....52

3.5.3 Hall Effect Analysis....61

3.6 Conclusions....62

3.7 References....63

4 HAFNIUM AS A SUBSTITUTE CONTACT TO (100) NANOCARBON SURFACES.... 66

4.1 Introduction to Transition Metal Carbides....66

4.2 Previous Work on Carbide Forming Contacts....68

4.3 The Choice of Hafnium as a Contact....69

CHAPTER Page

4.4 Materials Used 73

4.5 Experimental Tools 73

4.6 Experimental Process 74

4.7 Results and Discussion 78

4.7.1 XPS Results for Deposition of Hafnium 78

4.7.2 SEM Results 84

4.7.3 Hall Effect Measurements 86

4.7.4 Electrical Measurements 87

4.8 Conclusions 92

4.9 References 93

5 CONTACT FORMATION ON SELECTIVELY GROWN NANOCARBON ON DIAMOND 97

5.1 Introduction and Background 97

5.2 Experimental Tools 100

5.3 Experimental Process 101

5.4 Results and Discussion 103

5.4.1 XRT Results 103

5.4.2: EBSD and SEM Results 103

5.4.3 SiO2 Deposition and Etching Process 106

5.4.4 Selective Growth Results 110

5.4.5 Raman Spectroscopy 112

5.4.6 Elemental Analysis (LIBS) 114

CHAPTER Page

5.4.7 FIB-SEM Results 117

5.4.8 HF Dip Studies 120

5.5 Conclusions 123

5.6 References 125

6 SUMMARY AND FUTURE WORKS 127

REFERENCES 129

APPENDIX

A PERMISSION STATEMENT FROM CO-AUTHORS 141

LIST OF TABLES

Table Page

1. 1.1: Table Summarizing Some Electronic Properties of Silicon and Diamond 3

2. 2.1: Parameters Extracted from Room Temperature Hall Effect Measurements 28

3. 2.2: Extracted Values for Transfer Length, Contact Resistance, Sheet Resistance, and Sheet Resistivity....................34

4. 3.1: Extracted Electrical Parameters 59

5. 3.2: Comparison of Extracted Values from Work on Lightly Doped Diamond and Current Work 60

6. 4.1: Enthalpy of Formation for Transition Metal Carbides Found in the Ti-Zr-Hf group. *No Data Found for Rf Carbides 71

7. 4.2: Room Temperature Hall Effect Measurement Parameters....................86

8. 4.3: Table Comparing Extracted Parameters for Ti/Pt/Au and Hf/Pt/Au Contacts on NanoC Diamond 91

LIST OF FIGURES

Figure Page

1. 1.1.1: (A) Silicon Substrate (B) Diamond Substrate 2

2. 1.2.1: Schematic of U-PECVD Reactor 4

3. 1.2.2: Schematic of Ion Implantation System 4

4. 1.2.3: Resistance vs 1/Temperature for Boron Implanted Diamond by Known Distances or Spacings as Shown in Figure 1.3.1 5

5. 1.3.1: Schematic of Sample TLM Structures and Spacings 6

6. 1.3.2: Images of Some Tools Used: (A) Hall Effect System (B) Barrel Asher (C) Dektak (D) Spin Coater (E) SEM Setup (F) X-Ray Diffractometer (G) E-Beam Evaporator (F) Photolithography Aligner 7

7. 2.1.1: Some Examples of Nanocarbons 14

8. 2.3.1: ECOPIA SPCB-001 Testing Mount for Hall Effect Measurements….. 18

9. 2.3.2: Schematic of Process Flow for Development of Contacts for NanoC Sample 18

10. 2.3.3: Schematic of Device Parts 19

11. 2.3.4: TLM Structures after Photolithography..19

12. 2.3.5: SEM of TLM Structures after Metal Deposition...............................19

13. 2.4.1: SIMS of NanoC Layer on Diamond Substrate Showing High Concentrations of Nitrogen..20

14. 2.4.2: SEM Micrograph of NanoC Showing a Needle-Like Microstructure… 21

Figure Page

15. 2.4.3 : XRD Spectrum of NanoC 23

16. 2.4.4: Full Raman Spectrum 25

17. 2.4.5: Raman Spectrum Showing Peaks of Interest 26

18. 2.4.6: I-V Characteristics from the Hall Effect Measuring Tool when Current is Injected 27

19. 2.4.7: Optical Micrograph of TLM Structures..29

20. 2.4.8: Room Temperature I-V Plot for Different TLM Spacings for the Unannealed Sample 30

21. 2.4.9: Room Temperature -V Plot for Different Spacings after Sequential .... Annealing At 500 C 31

22. 2.4.10: Plot of Total Resistance vs. TLM Spacings over the Annealing Temperature Range...32

23. 2.4.11: Contact Resistance vs. Anneal Temperature 36

24. 2.4.12: Sheet Resistance vs Anneal Temperature.......................................37

25. 2.4.13: Specific Contact Resistivity vs. Anneal Temperature 38

26. 3.2.1: Process Flow for Lightly Phosphorus-Doped Diamond Study..........45

27. 3.4.1: Schematic of TLM Structure 48

28. 3.4.2. Device Stack Showing Contact Formation.......................................49

29. 3.4.3: Optical Microscopy of TLM Contacts after Metal Deposition…. 49

30. 3.4,4: SEM Showing TLM Devices..50

31. 3.5.1: SIMS Profile Showing Phosphorus Concentration in Diamond Film.... 51

Figure Page

32. 3.5.2: I-V Plots Showing Different Spacings before the Anneal.................54

33. 3.5.3: I-V Plots Showing Different Spacings after the 700 °C Anneal for 60 Mins 55

34. 3.5.4: Plot of Total Resistance vs Spacing Prior to Annealing....................56

35. 3.5.5: Plot of Total Resistance vs Spacing after A 700 °C Anneal.............57

36. 3.5.6: Plot Comparing Lightly Doped Diamond Measurements with Contact Resistivity Values 61

37. 3.5.7: Van Der Pauw Measurement Sample Holder...................................52

38. 4.1.1: Periodic Table of Elements..67

39. 4.3.1: Plot of Barrier Height vs. ΔH_f for Silicides 70

40. 4.3.2: Schematic of Previous Study of the Contact Ti/Pt/Au on NanoC….72

41. 4.3.3: Schematic of Study of Hf/Pt/Au on NanoC in this Work.................72

42. 4.6.1: Surface of Cleaned Element 6 Diamond Sample 77

43. 4.6.2: Hall Effect ECOPIA SPCB-001 Sample Mount 77

44. 4.7.1: Wide XPS Spectrum before and after Deposition Showing the Presence of Hafnium on the Substrate Surface 79

45. 4.7.2: Wide XPS Spectrum before and after Deposition with Peak Labels Showing the Presence of Hafnium on the Substrate Surface................80

46. 4.7.3: Oxygen 1s XPS Spectrum before and after Hafnium Deposition where Peak Shift Denotes Hafnium Oxide Formation 81

47. 4.7.4: Carbon 1s XPS Spectrum Showing the Bare Diamond Surface before Deposition and the Lowered Peak Due to Hafnium.. 82

Figure Page

48. 4.7.5: Hafnium 4F XPS Spectrum before and after Hafnium Deposition 83

49. 4.7.6: SEM Image of Nanocarbon Diamond Surface 85

50. 4.7.7: SEM Of TLM Contacts after Metal Deposition and Lift Off….........85

51. 4.7.8: Plot of Current-Voltage Measurements of TLM Contacts over Different Spacing..89

52. 4.7.9: Plot of Total Resistance vs Spacing..90

53. 5.1.1: Etching Procedure for First Method of Isolating Nano Underneath Metal Contacts 99

54. 5.1.2; Proposed Process Flow for Selective Growth Method of Isolating NanoC 99

55. 5.4.1: XRT Images of Three Diamond Samples Showing Defect Analysis…. 103

56. 5.4.2: Site Map of Phases Showing the Presence of Diamond on the Sample. 104

57. 5.4.3: Kikuchi Diffraction Pattern of Diamond 105

58. 5.4.4: Site Map of Detected Orientations on Diamond Surface 105

59. 5.4.5: SEM of Diamond Surface..106

60. 5.4.6: Profile of SiO_2 Deposition in PECVD Chamber Showing 400 nm of Deposited Material for Hard Masking 107

61. 5.4.7: Microscopy of Sample after Lithography and after SiO_2 Etching...108

62. 5.4.8: Profile of Photoresist Height after Lithography 109

Figure Page

63. 5.4.9: Profile Comparison before and after Etching of SiO_2 109

64. 5.4.10: Optical Microscopy of As-Received Diamond Surface 110

65. 5.4.11: Optical Micrograph of Cleaned Surface Prior to Growth............. 111

66. 5.4.12: Optical Micrograph after Selective Growth of NanoC.................. 112

67. 5.4.13: Raman Spectroscopy of Sample Surface 113

68. 5.4.14: Elemental Analysis Results Surface Outside Growth Region 115

69. 5.4.15: Elemental Analysis Results of Growth Surface............................ 116

70. 5.4.16: Schematic Diagram of Expected FIB Profile 117

71. 5.4.17: FIB-SEM of Surface Tilted to 70° 118

72. 5.4.18: Location of Profile Measurements.. 119

73. 5.4,19: Profile of FIB Area Showing Different Regions 120

74. 5.4.20: Plot of HF Dip Progression... 121

75. 5.4.21: Optical Microscopy of Sample Surface Prior to Wet Etching....... 122

76. 5.4.22: Optical Microscopy of Sample Surface after 9 Mins Etch. 122

77. 5.4.23: Optical Microscopy of Sample Surface after 15 Mins Etch 123

78. 5.4.23: Optical Microscopy of Sample Surface after 15 Mins Etch 123

LIST OF ABBREVIATIONS

Abbreviation Page

1. CVD: Chemical Vapor Deposition 1

2. PECVD: Plasma-Enhanced Chemical Vapor Deposition 3

3. TLM: Transfer Length Method/ Transmission Line Method 6

4. SIMS: Secondary Ion Mass Spectrometry 7

5. SEM: Scanning Electron Microscopy 7

6. XRD: X-ray Diffraction 7

7. XRT: X-ray Topography 7

8. UNCD: Ultrananocrystalline Diamond 12

9. DI: De-ionized 16

10. FIB-SEM: Focused Ion beam- Scanning Electron Microscopy 17

11. FWHM: Full width at Half Maximum 22

12. t-PA: trans-polyacetylene 24

13. EBSD: Electron Backscattering Diffraction 99

14. LIBS: Laser Induced Breakdown Spectroscopy 102

CHAPTER 1

INTRODUCTION

1.1 Background

Semiconductor devices are pervasive in modern life and metal-semiconductor contacts are an important component of many existing semiconductor devices. Silicon has been the most dominant semiconductor material due to its abundance on the earth, the availability of information on its processing which has largely driven its low costs and large market and also its ability to be thermally stable up to 1100 °C. However, silicon is relatively brittle, has a short life cycle and responds poorly in the high frequency range due to not being able to handle the large amounts of power with its bandgap of 1.12 eV [1]. High frequency applications nevertheless form a large part of systems we use such as radars, air navigation systems, dipole antennas, radio and television broadcasting, military, and local mobile radio transmission and hence there has been the need to find suitable wide band gap materials that can handle such large amounts of power in the high frequency ranges. Recently, diamond has emerged as an appealing alternative semiconductor material due to its superiority in affording some unique properties. Diamond is an allotrope of the element carbon with a diamond cubic crystal structure and can be characterized into natural and synthetic forms usually grown by chemical vapor deposition (CVD). As is widely known, elements in the same group on the periodic table often tend to exhibit similar characteristics because they have the same number of valence electrons hence the interest in diamond is not surprising. Further, in addition to being the hardest material due to its short sp^3 covalent bonds, diamond was found to be able to transmit across the microwave and ultraviolet

range and has a high thermal conductivity which can be exploited in high power devices and high-frequency applications [2]. Unlike the conventionally used silicon which has a bandgap of about 1.12 eV, diamond has a large bandgap of about 5.47 eV which makes it suitable in high temperature and high radiation environments. It also has a negative electron affinity and stable exciton state at room temperature, and a high breakdown field, high thermal conductivity [2 – 9], and finally it does not have a native oxide which could interfere with achieving some of the best material properties.

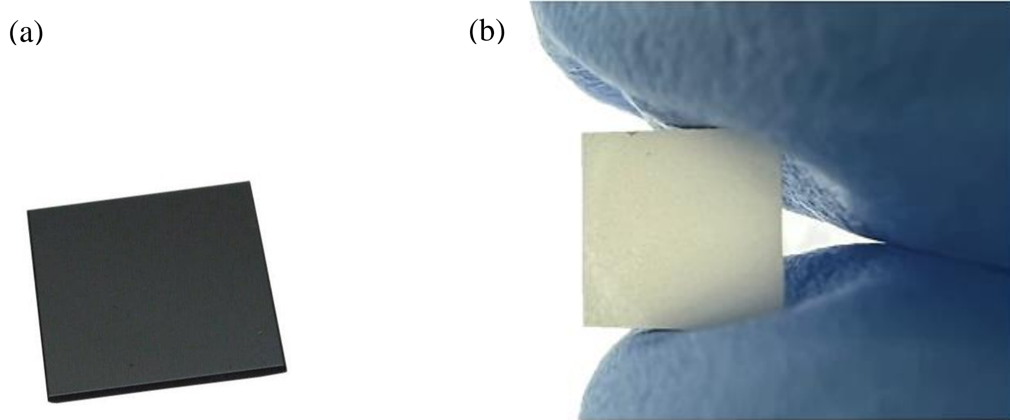

Figure 1.1.1: (a) silicon substrate [10] (b) diamond substrate

Table 1.1: Table Summarizing Some Electronic Properties of Silicon and Diamond [2]

	Silicon	CVD Diamond
Bandgap (eV)	1.12	5.47
Breakdown field ($MVcm^{-1}$)	0.30	10.00
Electron saturation velocity ($x10^7$ cm s^{-1})	0.86	2.00
Electron mobility ($cm^2V^{-1}s^{-1}$)	1450	4500
Hole mobility ($cm^2V^{-1}s^{-1}$)	480	3800
Thermal conductivity ($Wcm^{-1}K^{-1}$)	1.50	24.00

1.2 Doping of Diamond

New successes in p-type and especially n-type doping of diamond with dopants such as boron and phosphorus, respectively [11 – 12], have opened an extensive avenue of possibilities for the creation of sophisticated devices. Boron doping has been achieved by microwave plasma enhanced chemical vapor deposition (PECVD) and ion implantation techniques as shown in *Figs 1.2.1 & 1.2.2* respectively [13, 14] and devices on these p-type diamonds have been extensively studied with contact resistivity values in the $\sim 10^{-5}$ Ωcm^2 ranges as shown in *Fig 1.2.3* [4].

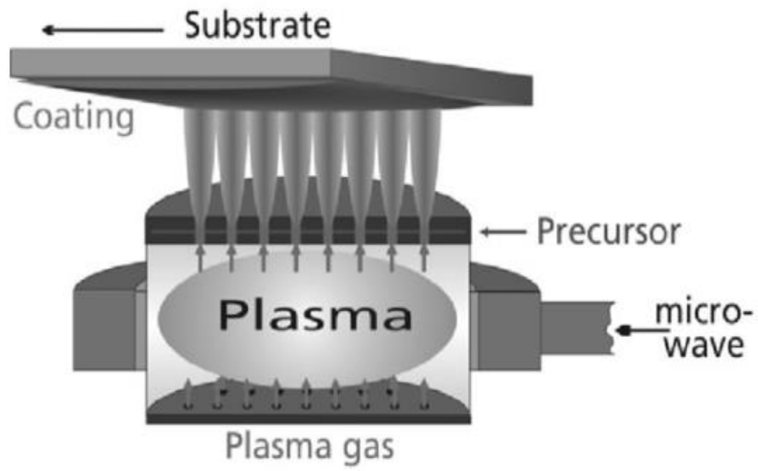

Figure 1.2.1: Schematic of μ-PECVD reactor [13]

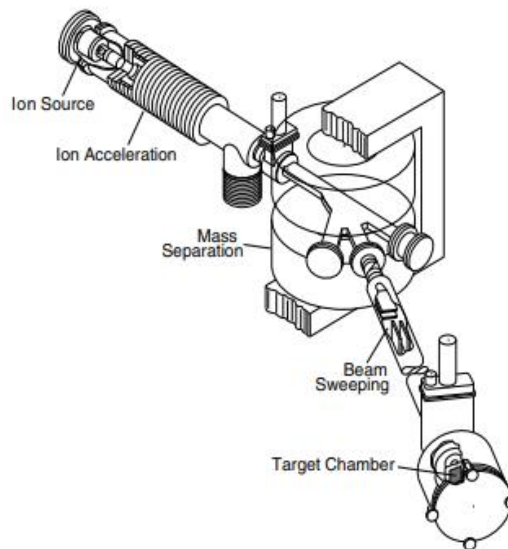

Figure 1.2.2: Schematic of ion implantation system [14]

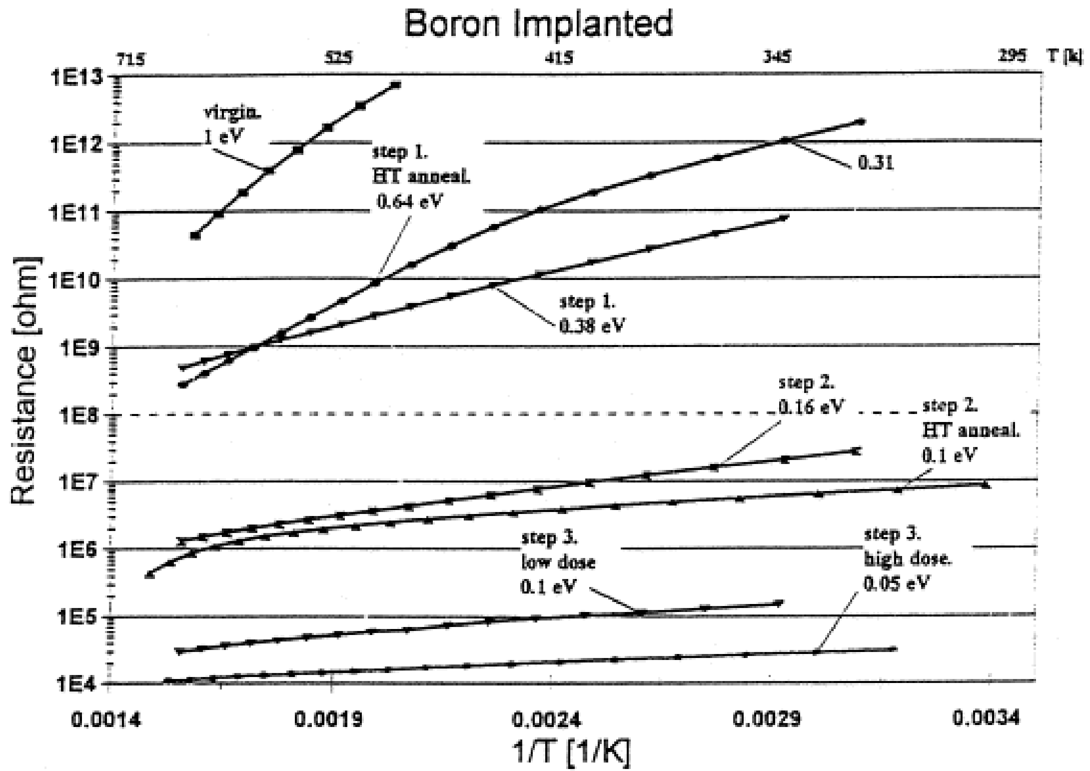

Figure 1.2.3: Resistance vs 1/Temperature for boron implanted diamond [15, 16]

N-type conductivity on the other hand is fairly recent and was first measured from phosphorus doped (P-doped) diamond in 1996 [17]. Prior work by Suzuki *et al.* [18] revealed that was especially problematic to achieve n-type conduction in diamond because of the deep donor states and low carrier concentration in P-doped diamond. As a result, the performance of n-type diamond has been in the early stages due to the high resistivity of n-type films and the poor thermal stability. Further, most of the work done on P-doped diamond has been limited to (111) oriented surfaces even though device (001) surfaces are important and required for better electrical properties and fabrication [19]. In order to improve on the reduction of contact resistance of n-type diamond devices, the two methods employed have been heavy doping or the use of other carbon mased materials called

nanocarbons due to the new and improved capabilities they can afford in diamond-based devices [20-25].

1.3 The Transfer Length Method

The transfer length method or TLM has been one of the best methods of extracting contact resistances between metals and semiconductors over the decades by way of measuring the current over a given voltage range and extracting the total resistance from several metal-semiconductor contacts separated by known distances or spacings as shown in *Figure 1.3.1* [26].

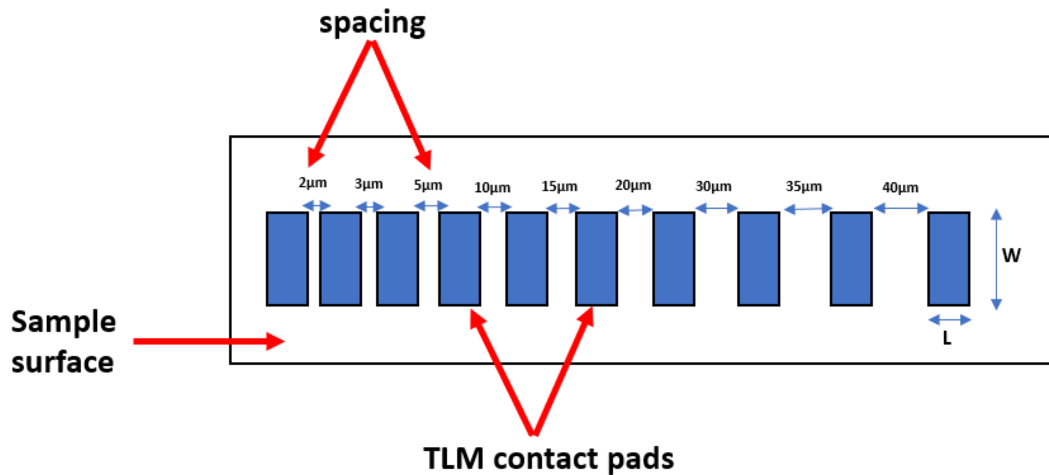

Figure 1.3.1: Schematic of sample TLM structures and spacings

The goal therefore is to test contacts on nitrogen doped nanocarbon layers firstly and on phosphorus doped diamond surfaces using the transfer length method to investigate the materials properties The results from several characterization techniques including Secondary Ion Mass Spectroscopy (SIMS), Scanning Electron Microscopy (SEM), X-ray diffraction (XRD), Raman scattering, Hall effect, Electrical probing and X-ray Topography(XRT) data are presented. In addition, improved values of the contact resistivity, sheet resistance, and specific sheet resistivity are demonstrated.

Figure 1.3.2: Images of some tools used: (a) Hall effect system (b) Barrel asher (c) Dektak profilometer (d) spin coater (e) SEM setup (f) X-ray diffractometer (g) E-beam evaporator (f) Photolithography aligner

1.4 Objectives of the Study

The following are the objectives of the work:

- Materials characterization of phosphorus doped diamond and nitrogen doped nanocarbon using techniques such as SEM, XRD, Raman scattering, Hall effect measurements and SIMS
- To fabricate TLM contacts on the samples using titanium, hafnium, platinum, and gold as contact metals
- To extract the electrical properties of the devices

1.5 Scope of Dissertation

This dissertation prospectus is composed of six chapters. First, the background, scope and objectives of the work are outlined in the Introductory chapter. The second chapter involves contact formation and characterization of heavily doped nanocarbon layers. Chapter three delves into work on lightly phosphorus doped diamond layers, Chapter four looks at the use of hafnium as part of contact metals, and Chapter 5 discusses selective area growth of the nanocarbon as a means to isolate it on the diamond surface. The project is summarized in Chapter six and recommendations for future studies are presented.

1.6 References

[1] Siu, C. (2022). Semiconductor physics. In *Electronic Devices, Circuits, and Applications* (pp. 35-39). Springer, Cham.

[2] Wort, C. J., & Balmer, R. S. (2008). Diamond as an electronic material. *Materials today*, *11*(1-2), 22-28.

[3] Geis, M. W. (1991). Diamond transistor performance and fabrication. *Proceedings of the IEEE*, *79*(5), 669-676.

[4] Matsumoto, T., Kato, H., Tokuda, N., Makino, T., Ogura, M., Takeuchi, D., ... & Yamasaki, S. (2014). Reduction of n-type diamond contact resistance by graphite electrode. *physica status solidi (RRL)–Rapid Research Letters*, *8*(2), 137-140.

[5] Kato, H., Umezawa, H., Tokuda, N., Takeuchi, D., Okushi, H., & Yamasaki, S. (2008). Low specific contact resistance of heavily phosphorus-doped diamond film. *Applied Physics Letters*, *93*(20), 202103

[6] Kato, H., Takeuchi, D., Tokuda, N., Umezawa, H., Okushi, H., & Yamasaki, S. (2009). Characterization of specific contact resistance on heavily phosphorus-doped diamond films. *Diamond and Related Materials*, *18*(5-8), 782-785

[7] Kato, H., Makino, T., Ogura, M., Tokuda, N., Okushi, H., & Yamasaki, S. (2009). Selective growth of buried n+ diamond on (001) phosphorus-doped n-type diamond film. *Applied Physics Express*, *2*(5), 055502.

[8] Teraji, T., Katagiri, M., Koizumi, S., Ito, T., & Kanda, H. (2003). Ohmic contact formation for N-type diamond by selective doping. *Japanese journal of applied physics*, *42*(8A), L882.

[9] Teraji, T., Koizumi, S., & Kanda, H. (2000). Ga ohmic contact for n-type diamond by ion implantation. *Applied Physics Letters*, *76*(10), 1303-1305.

[10] https://www.msesupplies.com/products/10-x-10-x-0-5-mm-n-type-p-doped-prime-grade-silicon-wafer-100-ssp-1-10-ohm-cm?variant=32215176249402

[11] Kalish, R. (1999). Doping of diamond. *Carbon*, *37*(5), 781-785.

[12] Teraji, T., Koizumi, S., Mita, S., Sawabe, A., & Kanda, H. (1999). Electrical contacts for n-type diamond. *Japanese journal of applied physics*, *38*(10A), L1096

[13] Dani, I., Mäder, G., Grabau, P., Dresler, B., Linaschke, D., Lopez, E., ... & Beyer, E. (2009). Atmospheric-Pressure Plasmas for Solar Cell Manufacturing. *Contributions to Plasma Physics*, *49*(9), 662-670.

[14] Nastasi, M. A., & Mayer, J. W. (2006). *Ion implantation and synthesis of materials* (Vol. 80). Berlin: Springer

[15] Kalish, R. (1997). Ion implantation in diamond; damage, annealing and doping. In *The Physics of Diamond* (pp. 373-409). IOS Press.

[16] Ran B. Technion-Israel Institute of Technology, M.Sc. thesis, 1997, unpublished

[17] Koizumi, S., Teraji, T., & Kanda, H. (2000). Phosphorus-doped chemical vapor deposition of diamond. *Diamond and Related Materials*, *9*(3-6), 935-940.

[18] Suzuki, M., Yoshida, H., Sakuma, N., Ono, T., Sakai, T., & Koizumi, S. (2004). Electrical characterization of phosphorus-doped n-type homoepitaxial diamond layers by Schottky barrier diodes. *Applied physics letters*, *84*(13), 2349-2351.

[19] Kato, H., Makino, T., Yamasaki, S., & Okushi, H. (2007). n-type diamond growth by phosphorus doping on (0 0 1)-oriented surface. *Journal of Physics D: Applied Physics*, *40*(20), 6189.

[20] Umeno, M., & Adhikary, S. (2005). Diamond-like carbon thin films by microwave surface-wave plasma CVD aimed for the application of photovoltaic solar cells. *Diamond and Related Materials*, *14*(11-12), 1973-1979.

[21] Dwivedi, N., Kumar, S., Carey, J. D., Malik, H. K., & Govind. (2012). Photoconductivity and characterization of nitrogen incorporated hydrogenated amorphous carbon thin films. *Journal of Applied Physics*, *112*(11), 113706.

[22] Carey, J. D., Smith, R. C., & Silva, S. R. P. (2006). Carbon based electronic materials: applications in electron field emission. *Journal of Materials Science: Materials in Electronics*, *17*(6), 405-412.

[23] Silva, S. R. P., & Carey, J. D. (2003). Enhancing the electrical conduction in amorphous carbon and prospects for device applications. *Diamond and Related Materials*, *12*(2), 151-158.

[24] Carey, J. D., & Henley, S. J. (2007). Clustering in nanostructured carbon: Evidence of electron delocalization. *Diamond and Related Materials*, *16*(10), 1782-1787.

[25] Wang, F. M., Chen, M. W., & Lai, Q. B. (2010). Metallic contacts to nitrogen and boron doped diamond-like carbon films. *Thin Solid Films*, *518*(12), 3332-3336.

[26] Schroder, D. K. (2015). *Semiconductor material and device characterization*. John Wiley & Sons.

CHAPTER 2

OHMIC CONTACTS TO NITROGEN-DOPED NANOCARBON LAYERS ON DIAMOND (100) SURFACES

2.1 Introduction to Nanocarbons

Owing to the increasing development of novel materials for power-electronics, and other semiconductor applications, nanocarbon films have become an interesting prospect due to the new and improved capabilities they can afford in diamond-based devices [1-8]. Nanocarbon films are materials with structures composed predominantly of carbon atoms and small amounts of nitrogen and hydrogen atoms with a structural range on the nanoscale. Some examples of nanocarbons are carbon nanotubes, fullerenes, corannulenes (Fig 2.1.1), and recently ultra-nanocrystalline diamond (UNCD). The latter has some properties that are similar to graphite or diamond and has been frequently used to investigate electrical properties [9-11]. In the field of electronic applications, Williams investigated electrical properties such as Hall Effect data at different temperatures in an attempt to reveal the mode of conductivity in n-type nitrogen-doped UNCD [12]. In this study, the UNCD film had grain sizes in the 3-5 nm range and was grown by plasma-enhanced chemical vapor deposition. It was found that this UNCD material exhibited properties similar to metallic conductivity. Gerbi *et al.* also investigated the contact properties of various metals on doped UNCD and detailed the influence of key parameters on the *I-V* characteristics, which included oxide formation at the metal/diamond interface, acid cleaning, electronegativity, and also delved into the mechanism of grain boundary conductivity for the material [13]. Further, Williams *et al*. also determined the mobilities

and carrier density of doped UNCD films which resulted in values of 1.5 $cm^2V^{-1}s^{-1}$ and $2\times10^{17}cm^{-2}$, respectively, with n-type conductivity [14]. Prior work by Birrell *et al.* investigated the morphology and structure of nitrogen-doped UNCD using TEM and presented the changes to the grain boundaries and grains upon adding nitrogen gas to explain why different nitrogen-doped UNCD films behaved differently [15]. By studying p-i-n diodes, Koeck *et al.* examined a new nanostructured carbon (nanoC) film similarly grown by plasma-enhanced chemical vapor deposition (PECVD), upon which this thesis is based [16,17]. The goal of using this material was to develop a low resistance contact material to phosphorus doped diamond [12,17-20]. In the same report electrical measurements were done in vacuum after annealing the material at 600°C. With the diodes in forward bias, UV light emission was observed which indicated bipolar operation, and efficient electron emission into vacuum was also observed. The improved diode emission was attributed to the reduction in room temperature contact resistivity ~5.5×10^{-3} Ωcm^2 [17].

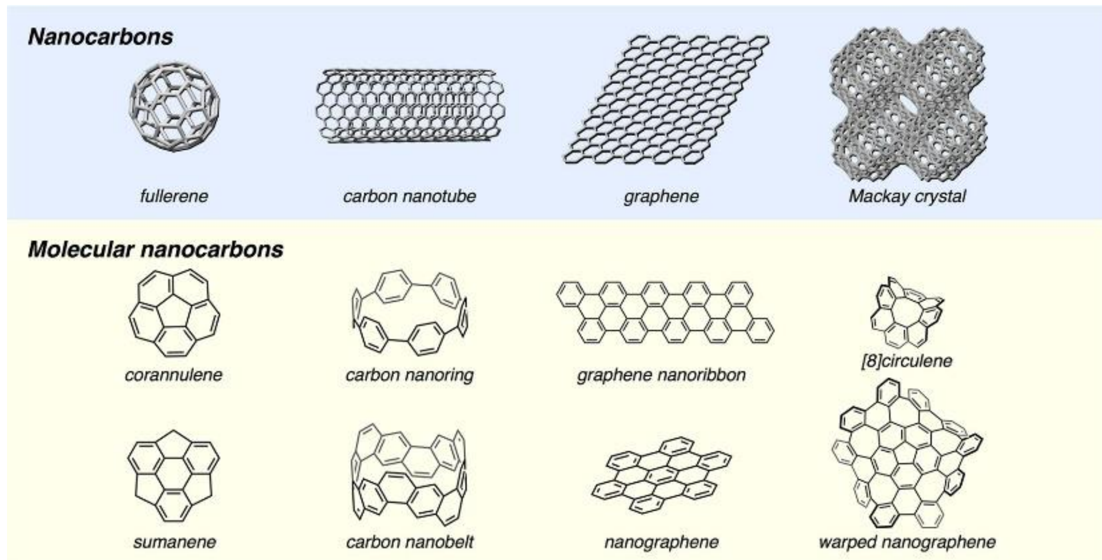

Figure 2.1.1: Some examples of nanocarbons[21]

Therefore, nitrogen doped nanocarbon layers were grown on diamond (001) surfaces and the transfer length method [22] was used to investigate the electrical properties employing a trilayer contact Ti/Pt/Au. The results from several characterization techniques including Secondary Ion Mass Scattering (SIMS), Scanning Electron Microscopy (SEM), X-ray diffraction (XRD), Raman scattering, and Hall effect data are presented. In addition, improved values of the contact resistivity, sheet resistance, and specific sheet resistivity are demonstrated.

2.2 Materials and Experimental Tools Used

The materials used include cleaning chemicals from the Nanofab cleanroom such as sulfuric acid (H_2SO_4), hydrogen peroxide(H_2O_2), hydrofluoric acid (HF), ammonium hydroxide (NH_4OH) and deionized (DI) water. Further, LOR 3A, AZ 3312, MIF 300, and AZ 400T were used for the lithography process and the metals titanium, platinum and gold were used for the deposition process.

Tools used for the fabrication, characterization and testing of the samples include:

- Pyrometer
- PECVD system
- Hall effect measuring system
- Dektak profilometer
- Secondary Ion Mass Spectrometer
- Spin coater
- Photolithography Aligner
- TLM mask
- Barrel asher
- Lesker e-beam evaporator
- Scanning electron Microscope
- Hot plate
- X-ray diffractometer
- Electrical Probe station
- Optical microscope
- Raman spectrometer

2.3 Experimental Process

Intrinsic CVD (100) diamond substrates obtained from Element 6 were cleaned using a boiling mixture of 3:1:1 $H_2SO_4/H_2O_2/H_2O$ at 220°C for 15 min, then a 5 min treatment in HF and finally boiling for 15 min in a mixture of 1:1:5 $NH_4OH:H_2O_2: H_2O$. In between each acid boiling step, the substrate was rinsed in DI water. The nanoC layers were grown using a plasma-enhanced CVD system. The ASTeX AX5000 reactor had an inductively heated sample stage. Samples were grown at a pressure of ~20 Torr, and a microwave power of 900 W. The deposition took place at around 900°C as measured by an optical pyrometer. For the gas flow rates, 10 sccm of argon, 100 sccm of nitrogen, and 20 sccm of methane, and 5 sccm of hydrogen were used. After a 30 min deposition SIMS analysis confirms an actual thickness of ~ 400 nm. The nitrogen incorporation of about ~6×10^{20} cm^{-3} attained SIMS using a Cameca 4F tool. The incident Cs^+ ions were accelerated to an energy of 10 keV. The ion beam had an incident angle of 24.5° from the surface normal and a beam current of 1 µA. The raster scan area was approximately 220µm by 220µm.

Samples were measured with an Ecopia Hall Effect HMS 5000 system to test the initial conductive properties. Van der Pauw measurements were done with the use of gold foil as contacts placed under the electrode pins (ECOPIA SPCB-001 sample mount Fig. 2.3.1). XRD was done using a PANalytical X-pert Pro MRD high-resolution X-ray diffractometer with Cu-Kα radiation with a beam current of 45 mA and anode tension of 45 kV. Raman spectra were measured using a custom Raman spectrometer with an excitation wavelength of 532 nm and laser power of 110 mW to explore the characteristics of phases present.

SEM was done with a Zeiss Auriga FIB-SEM with a beam voltage of 5kV and working distance of about 10 mm to observe the microstructure of the nanoC film.

The TLM metal contact structures were fabricated as shown in Fig 2.3.2. Photolithography was performed by spinning photoresist AZ3312 on the surface of the sample and exposing it for 6 sec in an OAI 808 aligner with a mask containing TLM pad structures with dimensions 101 µm by 50 µm and developing it with MIF 400 reagent. Using a barrel Tegal asher, the sample was treated in oxygen for approximately 1 min to enhance metal contact adhesion. The tri-layer metal stack Ti/Pt/Au was deposited at thicknesses of 50 nm/50 nm/200 nm using a Lesker electron-beam evaporator. Ti served as the adhesion layer, Pt as the diffusion barrier, and Au as the electrical contact (Fig. 2.3.3). After metal deposition, lift-off was done with AZ 400T stripper to remove the remaining photoresist and metal, leaving the metals only at the TLM structures (Figs. 2.3.4 & 2.3.5). Current-voltage *(I-V)* measurements were made using a Cascade probe station system with needle probes. The applied voltage ranged between -5V and 5V, and the current was measured across each spacing. Data acquisition IC-Cap software was used to make the *I-V* measurements. Subsequently, 20 min rapid thermal anneals at 500, 600, and 700° C were done in an AS-One rapid thermal processing system in a forming gas ambient, and the *I-V* characteristics were remeasured to extract the change in contact resistance with anneal temperature.

Figure 2.3.1: ECOPIA SPCB-001 testing mount for Hall effect measurements

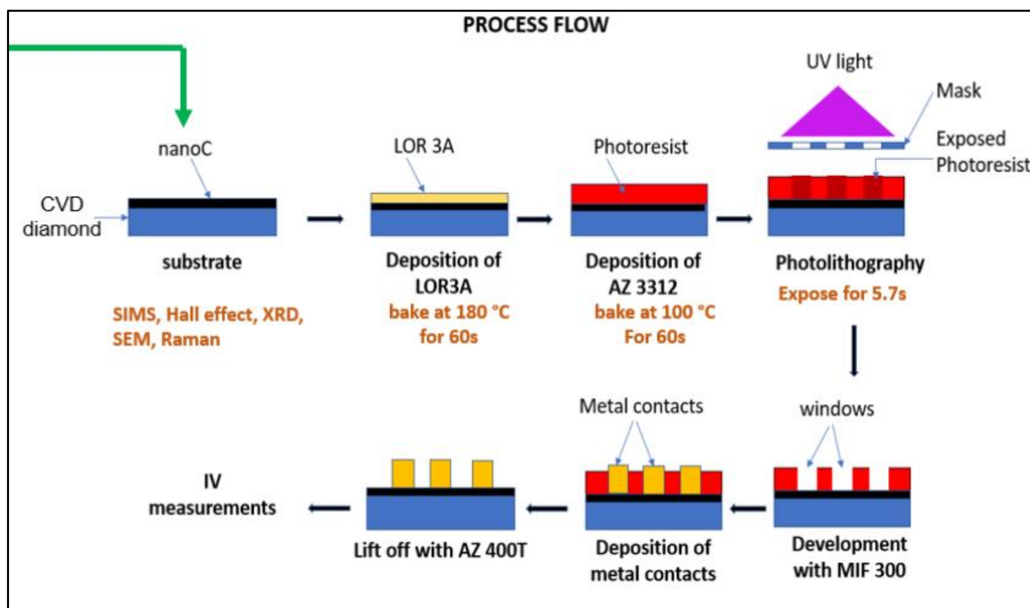

Figure 2.3.2: Schematic of process flow for development of contacts for nanoC sample

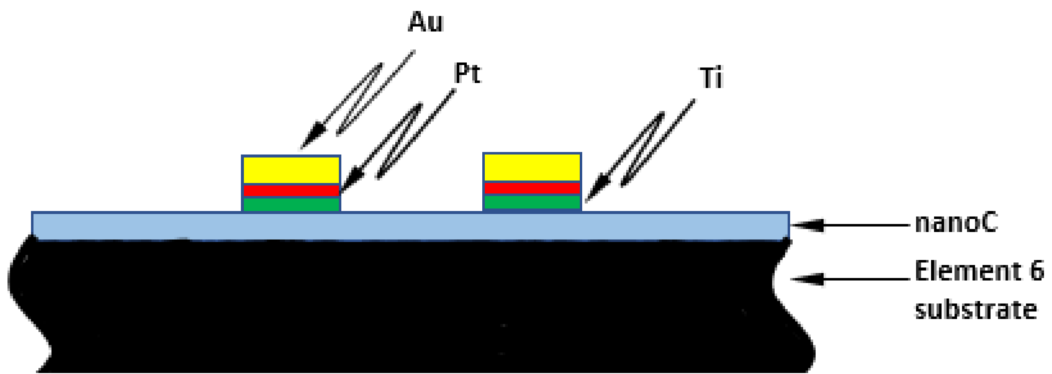

Figure 2.3.3: Schematic of device parts

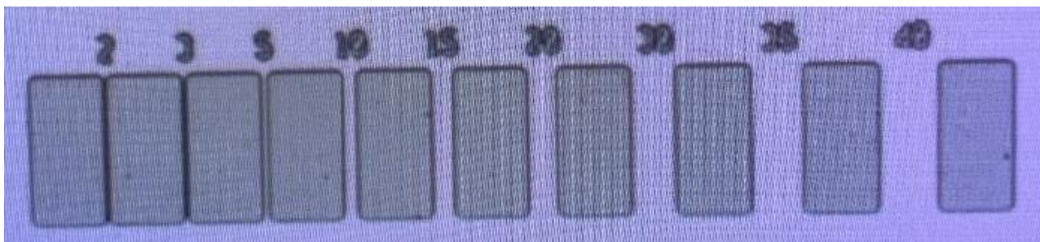

Figure 2.3.4: TLM structures after photolithography

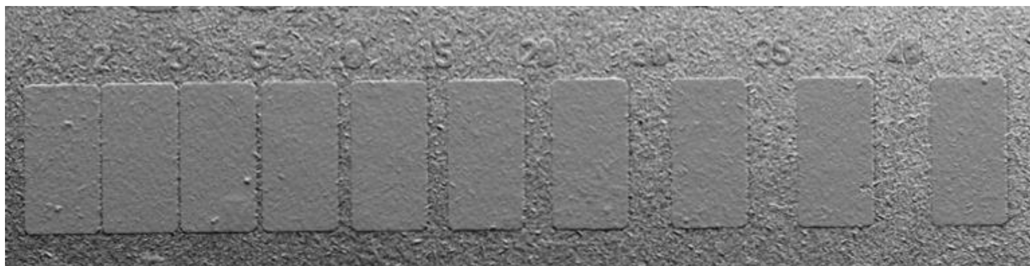

Figure 2.3.5: SEM of TLM structures after metal deposition

2.4 Results and Discussion

2.4.1 SIMS Results

Results from SIMS (Fig. 2.4.1) showed a high concentration of ~6 $\times 10^{20}$ atoms/cm^3 of nitrogen in the nanoC layer, which is among the highest concentrations reported for nano-carbon films. This high concentration enhances the defect states and, consequently, the electronic characteristics of devices.

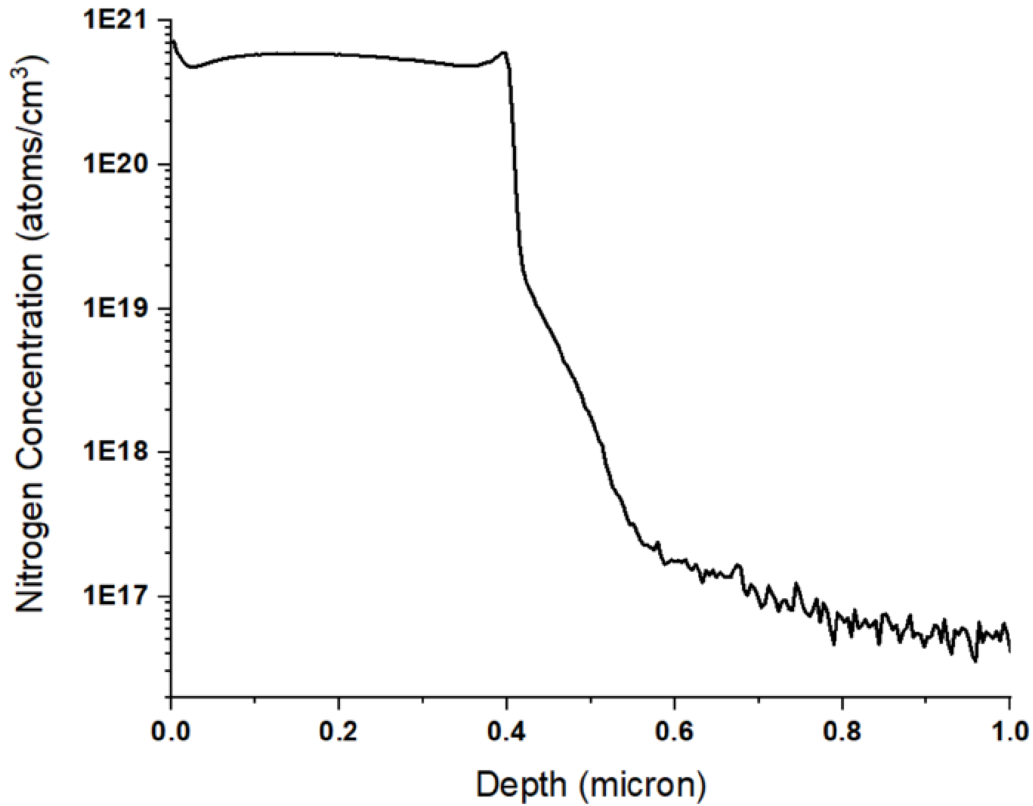

Figure 2.4.1: SIMS of nanoC layer on diamond substrate showing high concentrations of nitrogen incorporation.

2.4.2 SEM Analysis

The resulting image from SEM analysis as shown in Fig. 2.4.2 details a microstructure dispersed randomly with needle-like structures ranging from about 200 nm to 500 nm. This is due to the growth process in the nitrogen rich environment and is typical for many ultra-nanocrystalline and nanocrystalline diamond films [17].

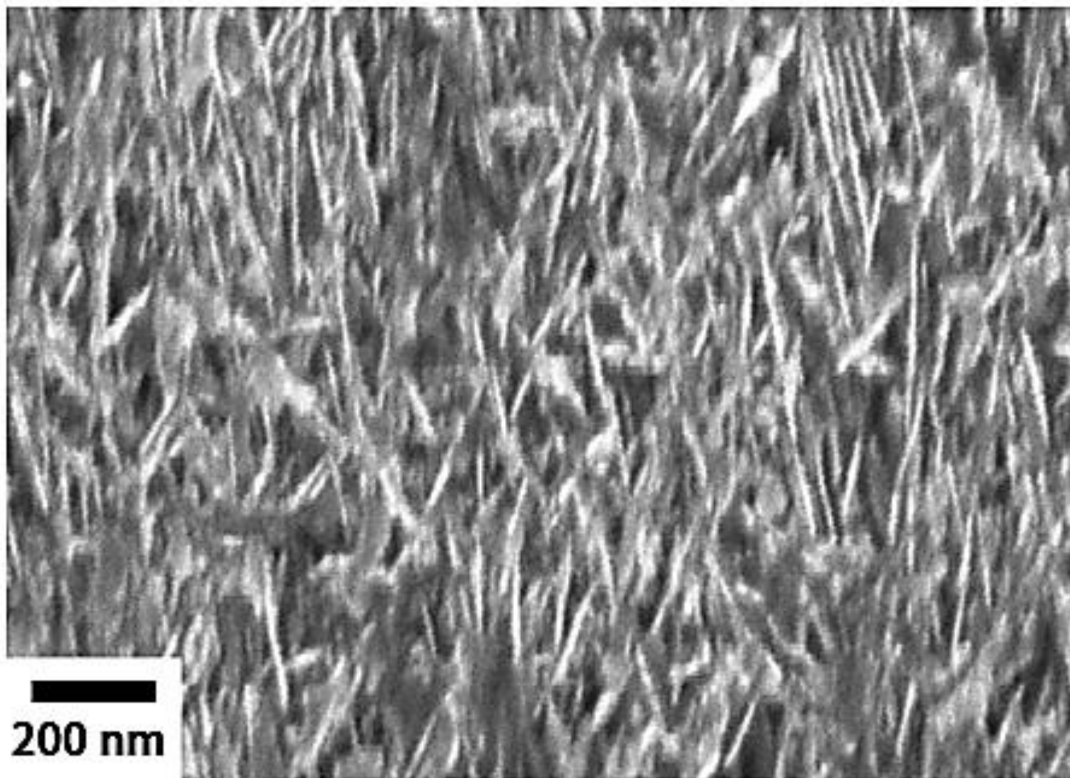

Figure 2.4.2: SEM micrograph of nanoC showing a needle-like microstructure

2.4.3 XRD Analysis

XRD results in Fig. 2.4.3 show that the nano-carbon material exhibits a mixture of crystalline and amorphous behavior, which is expected for these high conductivity samples. A diffraction peak is observed at a 2θ of about 17° and corresponds to a crystallite size of about 3.7 nm when calculated using the Debye Scherrer Equation (Eq. 1) where *D* is the crystallite size, *B* is the full width at half maximum (FWHM) of the diffraction peak, K is Scherrer's constant (K=0.94) and λ is the wavelength of the Cu-Kα radiation (0.1541 nm) [23].

$$D = \frac{K\lambda}{Bcos\theta} \quad \text{.................................Eq. (1)}$$

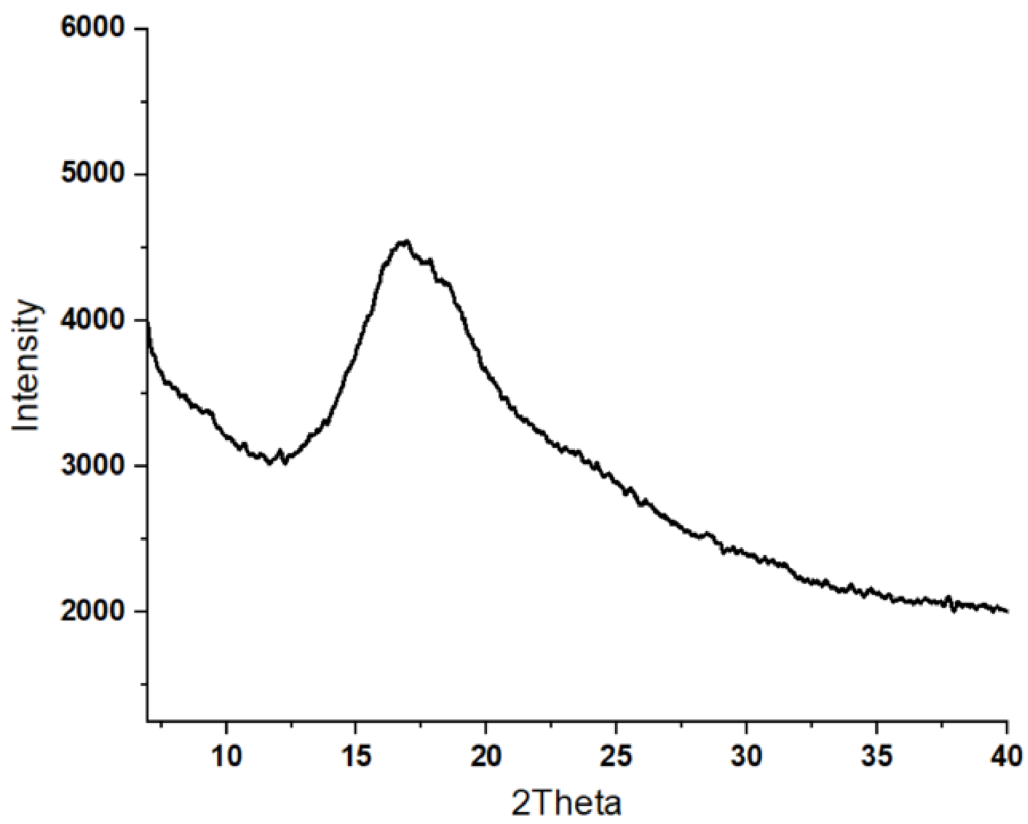

Figure 2.4.3 : XRD spectrum of nanoC

2.4.4 Raman Analysis

The Raman spectrum of the nano-carbon sample (Figs. 2.4.4 & 2.3.5) revealed peaks at Raman shifts of about 1133 cm^{-1}, 1336 cm^{-1}, 1590 cm^{-1}, 2700 cm^{-1}, and 2800 cm^{-1}. The smaller peak at ~2700 cm^{-1} represents the 2D band of second-order Raman scattering which is present for most diamond-like and carbon-based materials [24-26]. The peak at 1590 cm^{-1} represents a combination of the graphitic G peak and the disordered G' modes [17, 24, 27, 28]. Whereas the peak at 1336 cm^{-1} represents a combination of the crystal diamond mode (~1332 cm^{-1}) and the disorder induced D band, the broadening is attributed to the small size of grains, defects, and the presence of a large amount of nitrogen impurities from the growth process [17,24,28]. The peak at 1133 cm^{-1} represents the dispersed sp^3 bonding phase and the vibrational modes of trans-polyacetylene (t-PA) at the grain boundaries, which is known to decrease in intensity as the nitrogen content increases [17,24]. The second order peak at ~ 2800 cm^{-1} is attributed to a combination of the D and G' bands. The small size of the nanoC crystals, the large concentration of impurity nitrogen atoms, and the presence of defects give rise to an abundance of free electrons. It is these electrons that become active and play a key role in n-type conduction.

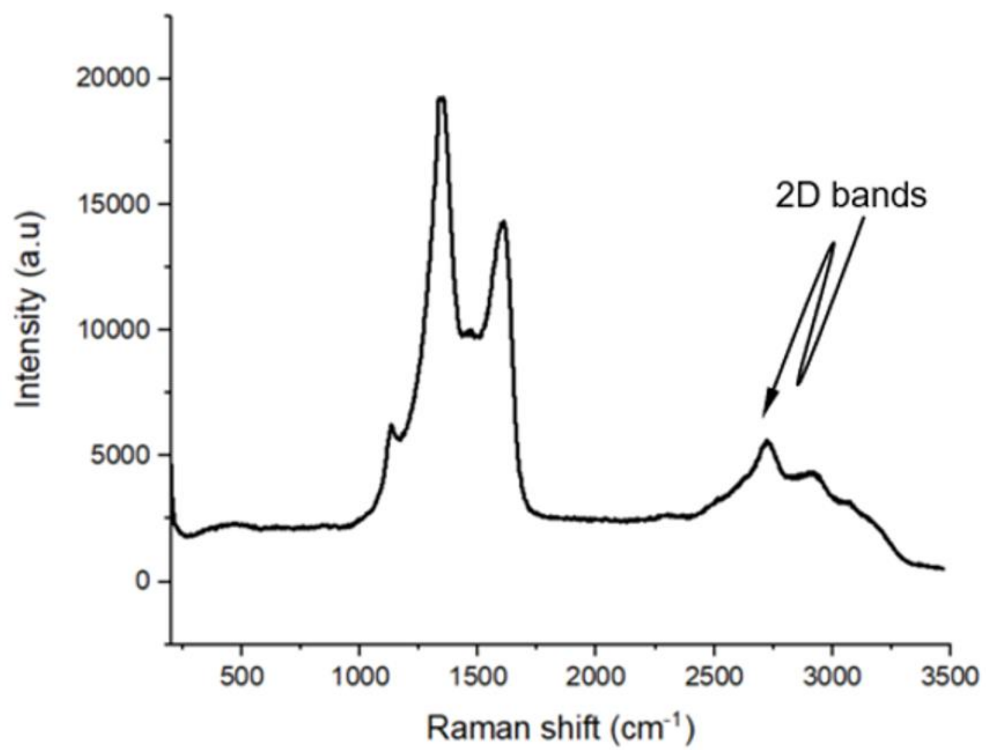

Figure 2.4.4: Full Raman spectrum

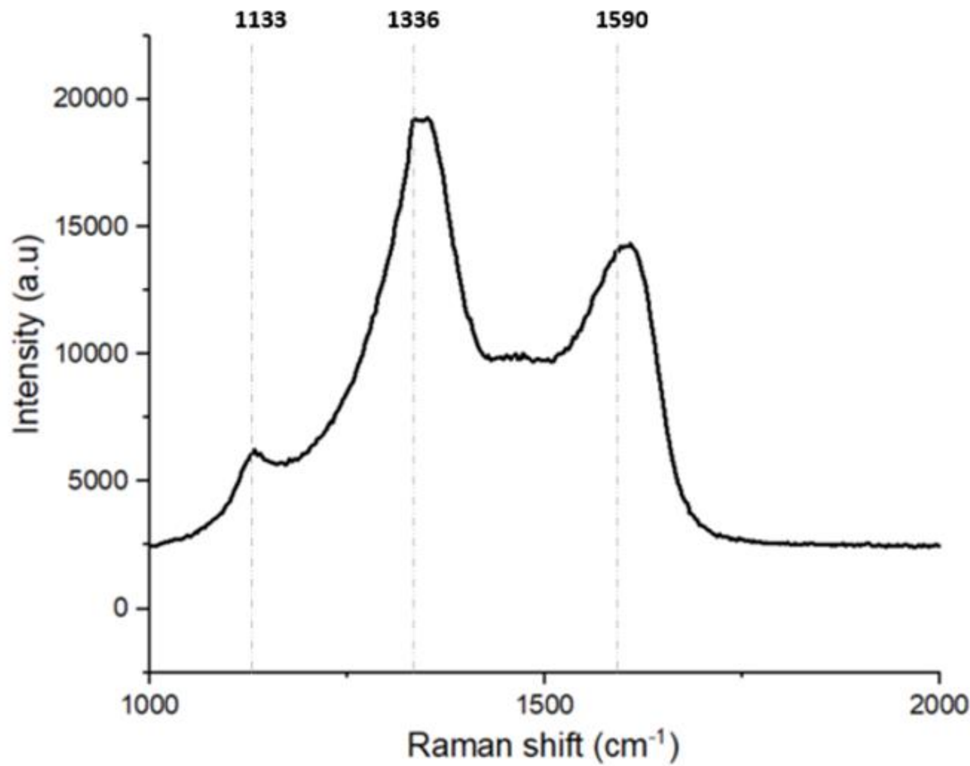

Figure 2.4.5: Raman spectrum showing peaks of interest

2.4.5 Hall Effect Analysis

From the results shown in Fig. 2.4.6, room-temperature Hall effect measurements confirm that the nano-carbon surface showed Ohmic behavior to about 10V which was the limit of the ECOPIA HMS 5000 system. Several Hall effect measurements were taken for repeatability, as shown in Table 2.1. The average bulk concentration of free electrons was derived to be 3.07×10^{20} cm^{-3}. The resistivity of the nanocarbon film was 1.52×10^{-2} Ωcm with a corresponding sheet resistance of 380 $\Omega\square^{-1}$. The room-temperature mobility was deduced to be 1.79 $cm^2V^{-1}s^{-1}$.

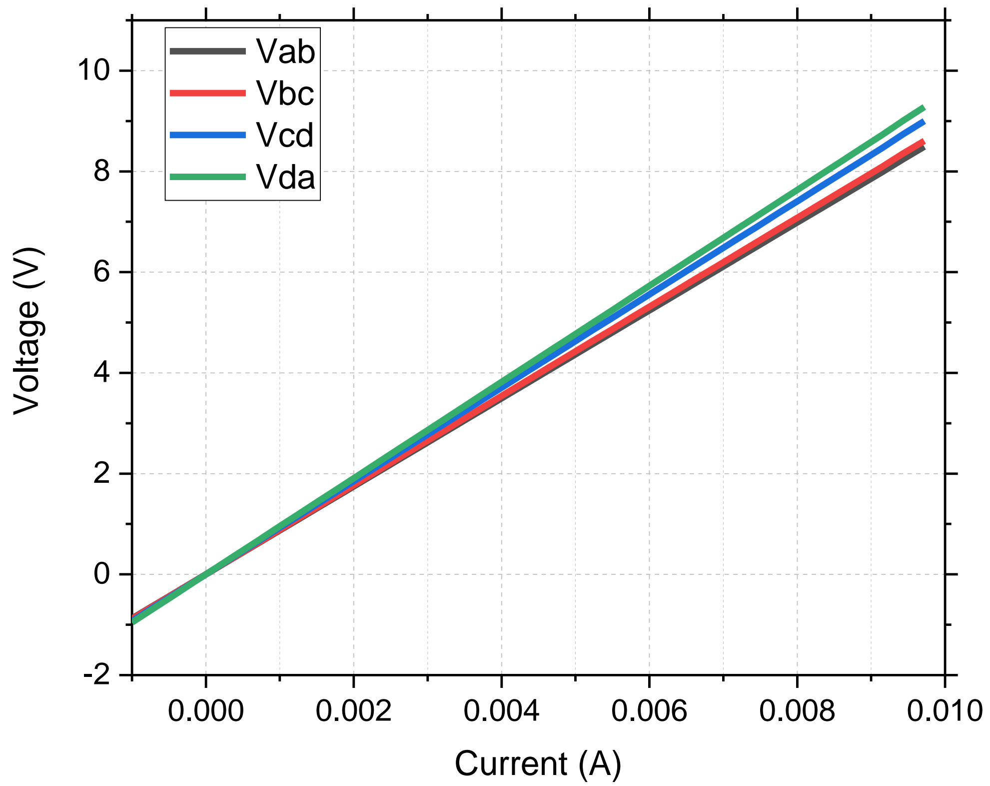

Figure 2.4.6: I-V characteristics from the Hall effect measuring tool when current is injected and measured between different pairs of terminals.

Table 2.1: Parameters Extracted from Room Temperature Hall Effect Measurements.

Parameter	**Average value**
Bulk electron concentration (cm^{-3})	3.07×10^{20}
Sheet electron concentration (cm^{-2})	9.22×10^{15}
Sheet resistance ($\Omega\square^{-1}$)	380
Resistivity (Ωcm)	1.52×10^{-2}
Mobility ($cm^2V^{-1}s^{-1}$)	1.79

2.4.6 Optical Microscopy and SEM of TLM Contacts

Optical microscopy and SEM images of the TLM structures after photolithography and metal deposition are shown in Figs. 2.3.4, 2.3.5, 2.4.7 and 2.4.2, respectively. The numbers in the images denote the spacing between the pads in microns. From Fig 2.4.7, the gold on the top of the contacts can be seen.

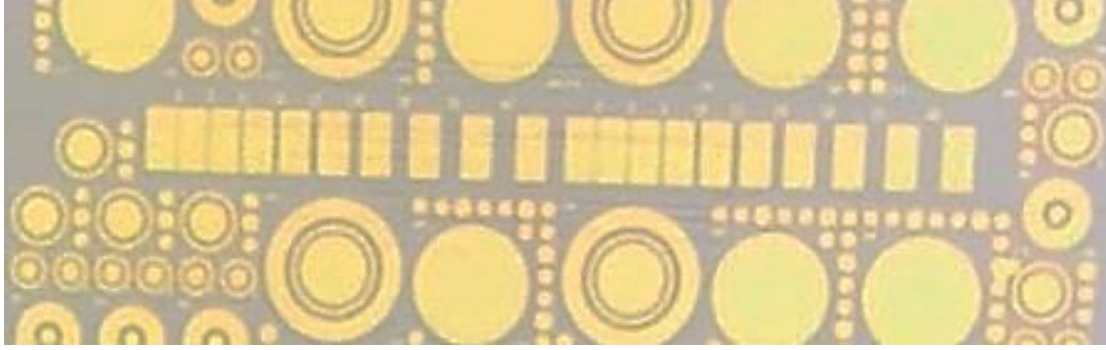

Figure 2.4.7: Optical micrograph of TLM structures

2.4.7 I-V Characteristics Analysis

Results from the current-voltage measurements confirmed linear Ohmic behavior, with the smaller spacings of 3 μm and 5 μm reaching the instrument's current compliance at 100 mA. The amount of current passing for each spacing gradually decreases as the spacing increases as expected and in SIMS indicates uniform current flow between the contact pads on the nano-carbon layer. After anneals of 500° to 700° C there were no significant changes in the *I-V* characteristics after each annealing step. Representative *I-V* plots with no annealing and after annealing at 700° C are shown in Figs. 2.4.8 and 2.4.9, respectively. There was no delamination of the gold contacts after annealing, indicating a strong adhesion via the titanium film. From these results, the total resistance of the contacts was extracted for each temperature as shown in Fig. 2.4.10. The total resistance increased as the spacing increased and showed little variation after each anneal.

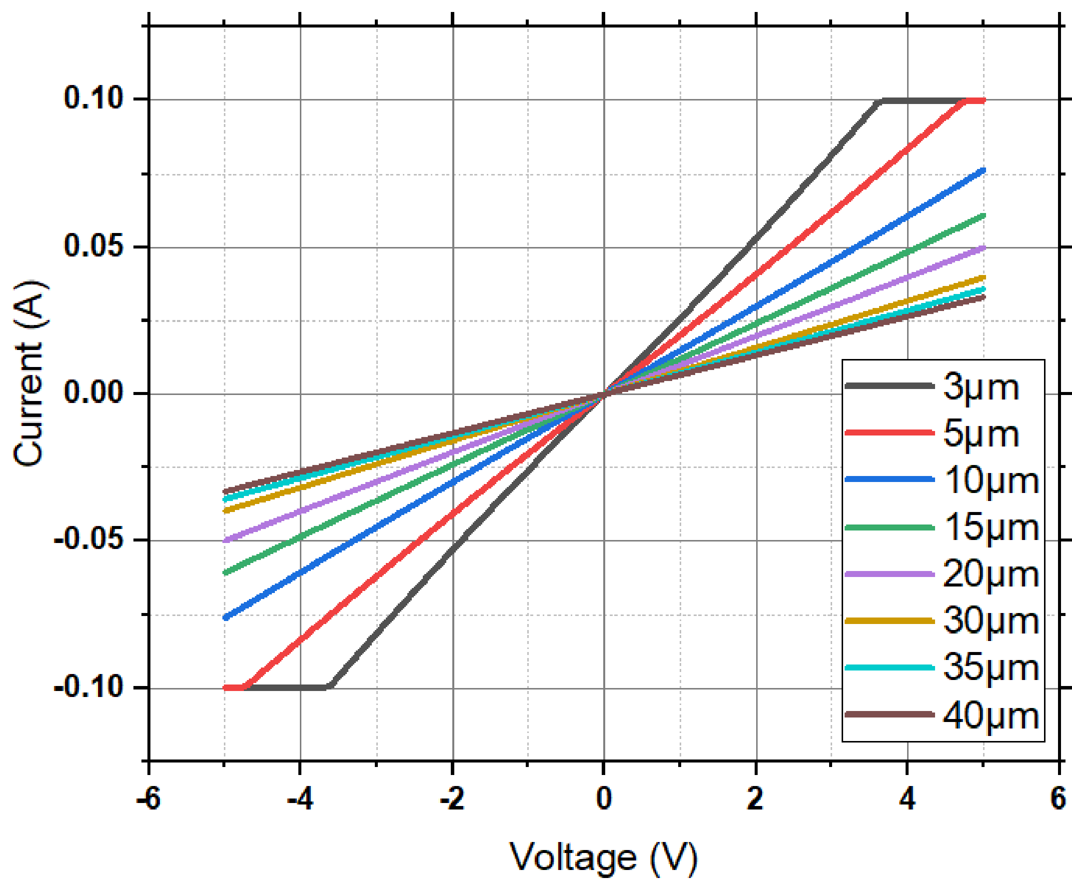

Figure 2.4.8: Room temperature I-V plot for different TLM spacings for the unannealed sample

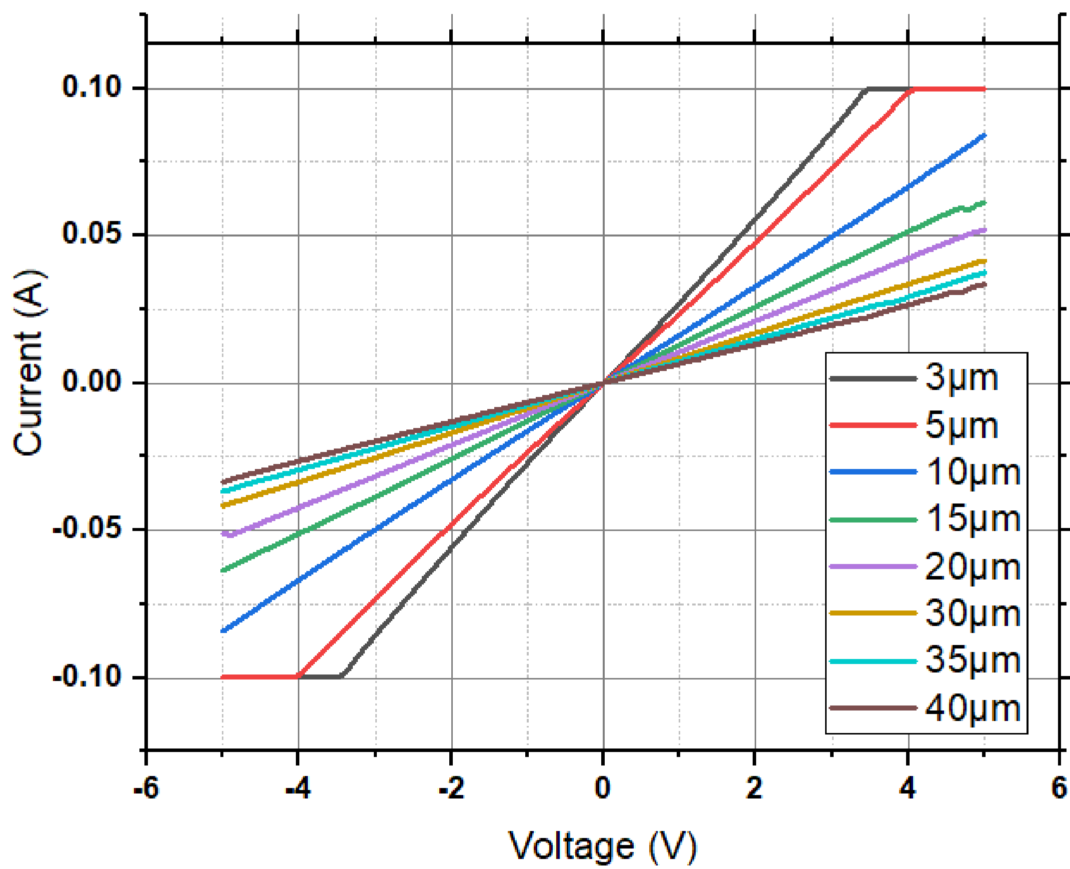

Figure 2.4.9: Room temperature I-V plot for different spacings after sequential annealing at 500° C for 20 mins, 600°C for 20 mins, and 700° C for 20 minutes

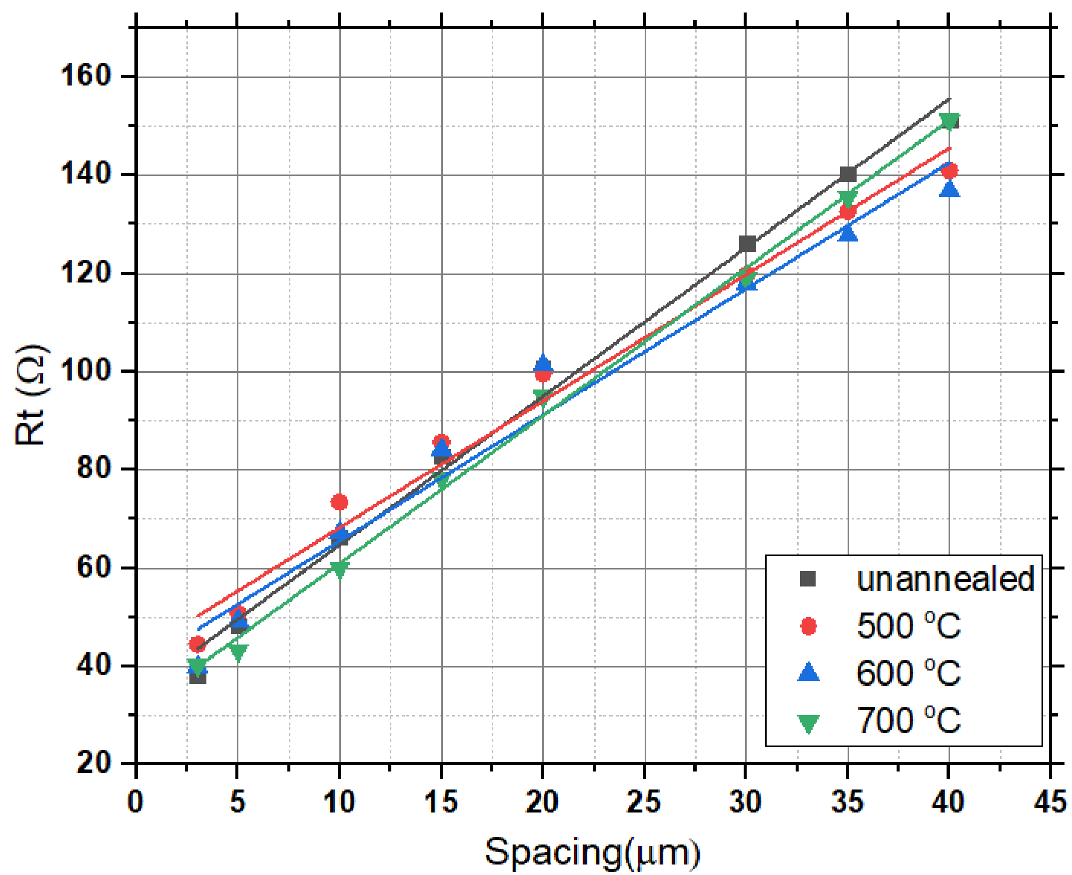

Figure 2.4.10: Plot of total resistance vs. TLM spacings over the annealing temperature range

From the total resistance, values of transfer length, contact resistance, sheet resistance, and sheet resistivity were calculated and tabulated in Table 2.2 below. Also, plots of these extracted values vs. annealing temperature are illustrated in Figs. 2.4.11- 2.4.13. From the table and figures, it can be generally observed that the contact resistance, and consequently the specific contact resistivity increased slightly after the 500° C and 600° C anneals. However, it decreased again after the 700° C anneal to a value closer to the unannealed condition. This was attributed to the onset of reactions between the titanium and the nano-carbon at the interface. After an anneal at 700° C, we expect a highly conducting titanium carbide layer to form between the nanoC layer and the titanium adhesion layer which is enabled by diffusion of oxygen away from the interface [29, 30]. The work of Koeck *et al.* [17] on similar nanoC material to that used in this study, reported a specific contact resistivity of 4.2×10^{-3} Ωcm^2 after a 300° C anneal [16]. In this study, TLM measurements yielded a lower value of 7.98×10^{-5} Ωcm^2 after the higher temperature annealing step at 700° C. This value is also lower than values extracted from previous UNCD material studied by Gerbi *et al.* [13] and Shimoda *et al.* [18] that had specific contact resistivity values of about 200-380 $m\Omega cm^2$. The increased incorporation of nitrogen atoms in the nanoC gives rise to the delocalization of π and π^* bands from the increased number of sp^2 bonded carbon at the grain boundaries. This causes a Fermi level shift upwards closer to the π^* band, which enhances hopping conduction to this band [17]. The high concentration of nitrogen also leads to an increase in graphitization of the nanoC material [31] which explains the attained low values of specific contact resistivity in this study.

Table 2.2: Extracted Values for Transfer Length, Contact Resistance, Sheet Resistance, and Sheet Resistivity

Anneal condition (°C)	**Transfer length (μm)**	**Contact resistance (Ω)**	**Sheet resistance (Ω□$^{-1}$)**	**Specific contact resistivity (Ωcm^2)**
unannealed	5.70	17.24	305.7	9.92×10^{-5}
500	8.20	21.13	260.3	1.75×10^{-4}
600	7.75	19.92	259.5	1.56×10^{-4}
700	5.12	15.42	304.1	7.98×10^{-5}

For TLM measurements it is typical to etch the conducting channel to ensure that the current between a pair of contacts is confined to a mesa channel with parallel, one-dimensional flow lines. However, reactive ion etching of the conducting nanoC layer in test samples proved to be problematic, with complete removal of the nanoC in some areas while other regions had nanoC remaining even after a significant over-etch. To avoid complications due to incomplete nanoC removal a mesa etch was not performed and nanoC covered the entire surface of the insulating diamond substrate. As a result, we expect fringing currents to flow around the periphery of the TLM contacts resulting in a lower total resistance than if the current was confined to a mesa etched channel [32]. To estimate the impact of the fringing currents we have completed a numerical simulation of the conduction between a pair of closely spaced contacts on a channel with the same sheet resistance as the nanoC film, see Supplementary Material. The simulations suggest that the fringing currents reduce the resistance by <20% for contacts with spacings of 5 μm or less,

while the correction can be as much 40% for the largest separations of 40 µm. For this reason, the TLM sheet resistances provided in Table 2.4.2 represent a lower bound to the actual values, which may explain why they are less than the 380 $\Omega\square^{-1}$ sheet resistance determined from the Hall effect measurements. Likewise, the minimum specific contact resistivity of $7.98\text{x}10^{-5}$ $\Omega.\text{cm}^2$ after annealing at 700° C is a lower bound, suggesting that nanoC based contacts to n-channel diamond devices can lower the contact resistance significantly compared to traditional all-metal contacts.

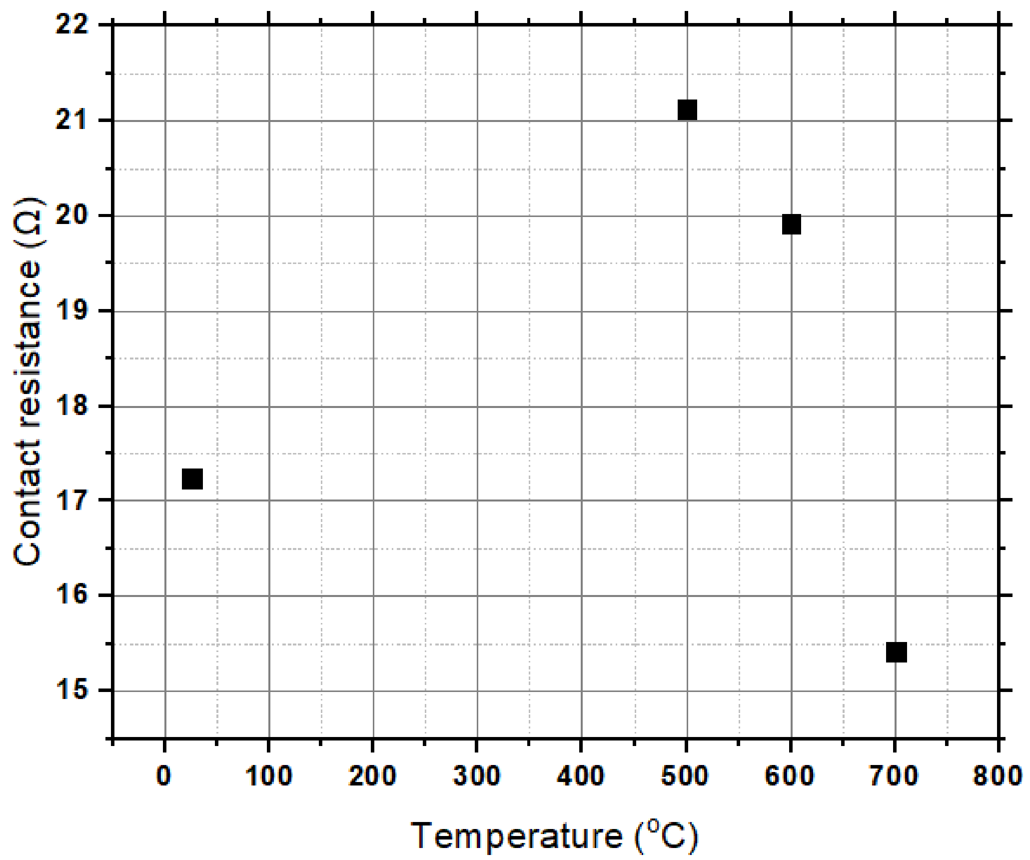

Figure 2.4.11: Contact resistance vs. anneal temperature

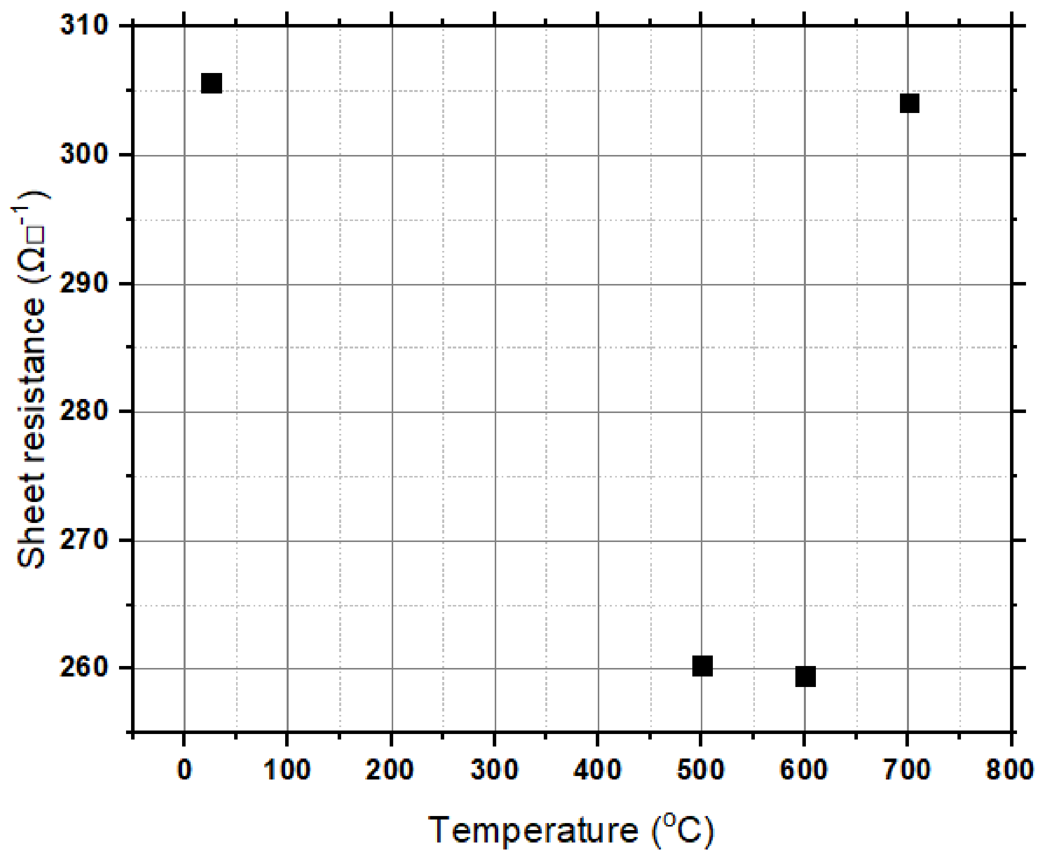

Figure 2.4.12: Sheet resistance vs anneal temperature

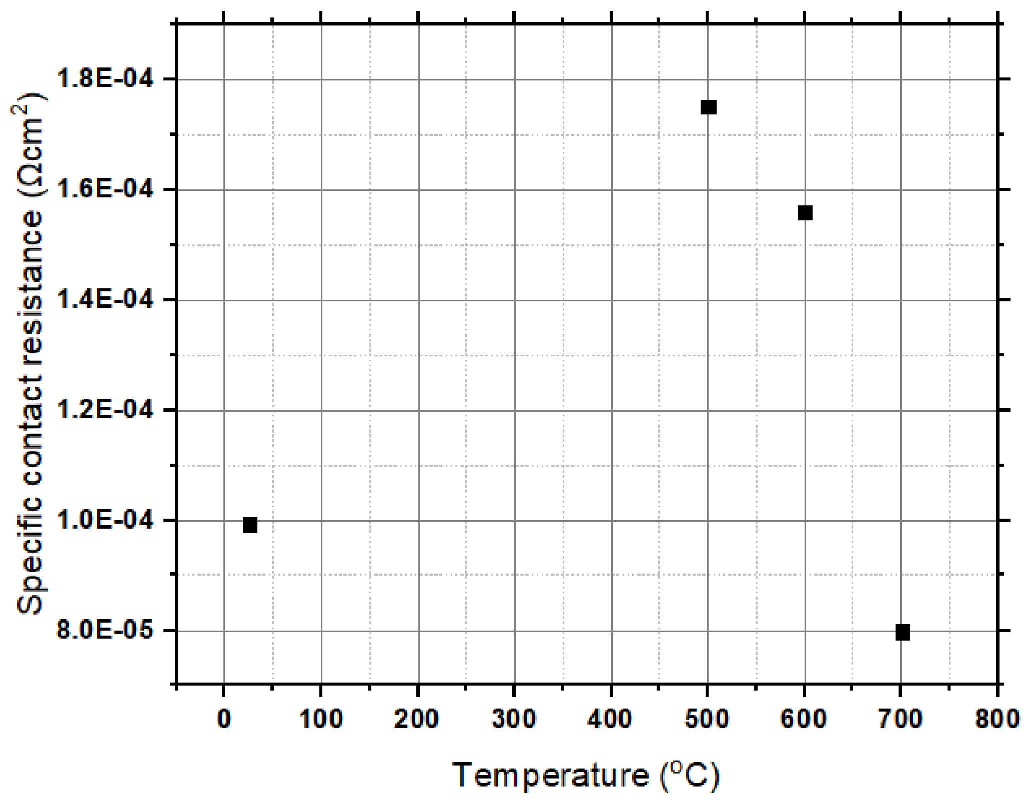

Figure 2.4.13: Specific contact resistivity vs. anneal temperature

2.5 Conclusion

Using the transfer length method, tri-layer metal contacts of Ti/Pt/Au were deposited on a nanostructured carbon film to investigate their electrical properties. SIMS, XRD, and Raman scattering were used to establish the material properties. Hall effect measurements confirmed the highly conductive nature of the nano-carbon with a bulk electron concentration of 3.07×10^{20} cm^{-3} and a room temperature mobility of 1.79 $cm^2V^{-1}s^{-1}$. Electrical *I-V* measurements also showed good Ohmic contact between the metal stack and the nano-carbon surface. After annealing at 700° C, the *I-V* measurement resulted in low specific contact resistivity of ~7.98×10^{-5} Ωcm^2. The TLM results support using nano-carbon material for low resistance contacts on diamond-based devices and in mitigating low phosphorus incorporation in crystalline diamond used in electronic applications.

2.6 References

[1] Umeno, M., & Adhikary, S. (2005). Diamond-like carbon thin films by microwave surface-wave plasma CVD aimed for the application of photovoltaic solar cells. *Diamond and Related Materials*, *14*(11-12), 1973-1979.

[2] Dwivedi, N., Kumar, S., Carey, J. D., Malik, H. K., & Govind. (2012). Photoconductivity and characterization of nitrogen incorporated hydrogenated amorphous carbon thin films. *Journal of Applied Physics*, *112*(11), 113706.

[3] Carey, J. D., Smith, R. C., & Silva, S. R. P. (2006). Carbon based electronic materials: applications in electron field emission. *Journal of Materials Science: Materials in Electronics*, *17*(6), 405-412.

[4] Silva, S. R. P., & Carey, J. D. (2003). Enhancing the electrical conduction in amorphous carbon and prospects for device applications. *Diamond and Related Materials*, *12*(2), 151-158.

[5] Carey, J. D., & Henley, S. J. (2007). Clustering in nanostructured carbon: Evidence of electron delocalization. *Diamond and Related Materials*, *16*(10), 1782-1787.

[6] Wang, F. M., Chen, M. W., & Lai, Q. B. (2010). Metallic contacts to nitrogen and boron doped diamond-like carbon films. *Thin Solid Films*, *518*(12), 3332-3336.

[7] Inaba, M., Seki, A., Sato, K., Kushida, T., Kageura, T., Yamano, H., ... & Kawarada, H. (2017). Vertical edge graphite layer on recovered diamond (001) after high-dose ion implantation and high-temperature annealing (Phys. Status Solidi B 9/2017). *physica status solidi (b)*, *254*(9), 1770249.

[8] Mizuno, Y., Ito, Y., & Ueda, K. (2021). Optoelectronic synapses using vertically aligned graphene/diamond heterojunctions. *Carbon*, *182*, 669-676.

[9] Melezhyk, A. V., Yanchenko, V. V., & Sementsov, Y. I. (2007). Nanocarbon *Materials. In Hydrogen Materials Science and Chemistry of Carbon Nanomaterials (pp. 529-537). Springer, Dordrecht.*

[10] Awasthi, K., Kumar, R., Raghubanshi, H., Awasthi, S., Pandey, R., Singh, D., & Srivastava, O. N. (2011). Synthesis of nano-carbon (nanotubes, nanofibres, graphene) materials. *Bulletin of Materials Science*, *34*(4), 607-614.

[11] Nambo, M., & Itami, K. (2009). Synthesis of new nano-carbon materials. *Access Science*.

[12] Williams, O. A. (2006). Ultrananocrystalline diamond for electronic applications. *Semiconductor Science and Technology*, *21*(8), R49.

[13] Gerbi, J. E., Auciello, O., Birrell, J., Gruen, D. M., Alphenaar, B. W., & Carlisle, J. A. (2003). Electrical contacts to ultrananocrystalline diamond. *Applied Physics Letters*, *83*(10), 2001-2003.

[14] Williams, O. A., Curat, S., Gerbi, J. E., Gruen, D. M., & Jackman, R. B. (2004). n-Type conductivity in ultrananocrystalline diamond films. *Applied Physics Letters*, *85*(10), 1680-1682.

[15] Birrell, J., Carlisle, J. A., Auciello, O., Gruen, D. M., & Gibson, J. M. (2002). Morphology and electronic structure in nitrogen-doped ultrananocrystalline diamond. *Applied Physics Letters*, *81*(12), 2235-2237.

[16] F.A. Koeck, and R.J. Nemanich, "Contact structures for n-type diamond." U.S. Patent 11,380,763.

[17] Koeck, F. A., Benipal, M., & Nemanich, R. J. (2020). Electrical contact considerations for diamond electron emission diodes. *Diamond and Related Materials*, *101*, 107607.

[18] Shimoda, N., Kato, Y., & Teii, K. (2016). Electrical contacts to nanocrystalline diamond films studied at high temperatures. *Journal of Applied Physics*, *120*(23), 235706.

[19] Liu, Y. K., Tso, P. L., Pradhan, D., Lin, I. N., Clark, M., & Tzeng, Y. (2005). Structural and electrical properties of nanocrystalline diamond (NCD) heavily doped by nitrogen. *Diamond and Related Materials*, *14*(11-12), 2059-2063.

[20] Chen, Q., Gruen, D. M., Krauss, A. R., Corrigan, T. D., Witek, M., & Swain, G. M. (2001). The structure and electrochemical behavior of nitrogen-containing nanocrystalline diamond films deposited from CH4/N2/Ar mixtures. *Journal of The Electrochemical Society*, *148*(1), E44.

[21] Segawa, Y., Levine, D. R., & Itami, K. (2019). Topologically unique molecular nanocarbons. *Accounts of chemical research*, *52*(10), 2760-2767.

[22] Schroder, D. K. (2015). *Semiconductor material and device characterization*. John Wiley & Sons.

[23] Cullity, B. D., & Stock, S. R. (2001). *Elements of X-ray Diffraction, Third Edition*. Prentice-Hall.

[24] Yu, J., Liu, G., Sumant, A. V., Goyal, V., & Balandin, A. A. (2012). Graphene-on-diamond devices with increased current-carrying capacity: carbon sp2-on-sp3 technology. *Nano letters*, *12*(3), 1603-1608.

[25] Kaniyoor, A., & Ramaprabhu, S. (2012). A Raman spectroscopic investigation of graphite oxide derived graphene. *Aip Advances*, *2*(3), 032183.

[26] Tuinstra, F., & Koenig, J. L. (1970). Raman spectrum of graphite. *The Journal of Chemical Physics*, *53*(3), 1126-1130.

[27] Kudin, K. N., Ozbas, B., Schniepp, H. C., Prud'Homme, R. K., Aksay, I. A., & Car, R. (2008). Raman spectra of graphite oxide and functionalized graphene sheets. *Nano Letters*, *8*(1), 36-41.

[28] Nemanich, R. J., & Solin, S. A. (1979). First-and second-order Raman scattering from finite-size crystals of graphite. *Physical Review B*, *20*(2), 392.

[29] Tachibana, T., Williams, B. E., & Glass, J. T. (1992). Correlation of the electrical properties of metal contacts on diamond films with the chemical nature of the metal-diamond interface. II. Titanium contacts: A carbide-forming metal. *Physical Review B*, *45*(20), 11975.

[30] H. M. Johnson, J. M. Brown, A. M. Zaniewski, R. J. Nemanich, Cleaning diamond surfaces via oxygen plasma inhibits the formation of a TiC interface, Diamond and Related Materials 126, 109058 (2022).

[31] Achatz, P., Williams, O. A., Bruno, P., Gruen, D. M., Garrido, J. A., & Stutzmann, M. (2006). Effect of nitrogen on the electronic properties of ultrananocrystalline diamond thin films grown on quartz and diamond substrates. *Physical Review B*, *74*(15), 155429.

[32] Grover, S., Sahu, S., Zhang, P., Davis, K. O., & Kurinec, S. K. (2020, May). Standardization of specific contact resistivity measurements using transmission line model (TLM). In *2020 IEEE 33rd International Conference on Microelectronic Test Structures (ICMTS)* (pp. 1-6). IEEE.

CHAPTER 3
LOW CONTACT RESISTIVITY OF LIGHTLY PHOSPHORUS-DOPED DIAMOND LAYER

3.1 Performance of Phosphorus Doped Diamond

Research into phosphorus doped diamond has seen some impressive milestones over the last few years. Early work by Teraji *et al.* [1] delved into Schottky barriers and reported an activation energy of 0.5 eV and a mobility of 28 $cm^2/V.\ s$ for homoepitaxial n-type diamond films among other key electrical properties. Recent successes included the improvement of current amplification at room temperature by optimized phosphorus doping of diamond as a base layer to reduce series resistance by Kato *et al.* [2]. Moazed *et al.* showed that titanium (Ti) and tantalum were good candidates for forming ohmic contacts after anneals [3]. Further, Kato *et al*. formed Ti contacts on heavily doped diamond grown by microwave Plasma-Enhanced Chemical Vapor Deposition (PECVD) using the Transfer Length Method (TLM). From additional studies, resistance was reduced at room temperature which showed that the barrier width was small enough for tunnelling. Ohmic contacts were found to attain high performance when higher phosphorus incorporation (above 10^{19} cm^{-3}) was achieved [4]. Shimaoka *et al.* also employed the use of heavily doped n-layers in metal-semiconductor field-effect transistors to enhance the Ohmic behavior of the drain and source contacts [5]. Work by Kato *et al.* showed that the specific contact resistance of Ti contact on P-doped diamond by circular type TLM was reduced to the order of 10^{-3} cm^2 using P-doped diamonds with a concentration of about 10^{20} cm^{-3} and some ideal Ohmic properties were achieved as well [6].

3.2 Heavy Versus Light Phosphorus Doping

However, in devices such as bipolar junction transistors, where mobility is of optimum importance, heavily doped diamond layers may not be the best option. Notwithstanding that heavy doping may present some advantages, it also gives rise to the prevalence of complex defects in the diamond film which can lead to impurity scattering effects, which are unwanted[7, 8]. Heavy doping is also relatively time consuming and expensive as a result. Owing to this, there is the need to create light to moderate P-doped films with good specific contact resistivities. Nesladek reports the possibility of controlling a phosphorus concentration in the ranges of 10^{16}-10^{19} atoms.cm^{-3} maintaining mobilities above 600 cm^2/V. s [9]. A study by Koizumi *et al.* shares a measured room temperature maximum Hall mobility of 240 cm^2/Vs in P-doped diamond with a concentration of 3×10^{18} cm^{-3} [10]. A phosphorus concentration of 7×10^{16} cm^{-3} also gave rise to a high mobility of about 660 cm^2/Vs in work by Katagiri *et al.* [11]. These works forecast that mobilities will improve with lower doping. Nevertheless, there has been a trade-off in creating lightly doped devices with a relatively good mobility and low contact resistivities close to the values obtained for heavily P-doped diamond layers. Works by Kato *et al.* [12], Teraji *et al.* [13], Teraji *et al.* [14] with light phosphorus concentrations between 10^{18} cm^{-3} and low 10^{19} cm^{-3} have resulted in contact resistivities in the range of 10^6 Ωcm^2 which are very high. With a phosphorus concentration of 5×10^{19} cm^{-3} Takemasa *et al.* reports a contact resistivity in the range of 10^{-1}-10^0 Ωcm^2 for some metal/n-diamond contacts which has been the lowest so far[15].

In view of these challenges and recent breakthroughs, we present the formation of Ohmic contacts Ti/Pt/Au to a lightly phosphorus doped diamond surface using TLM measurements [16]. Secondary Ion Mass Spectrometry (SIMS) results are presented to show the dopant profile, Hall effect measurements are presented to explore the free carrier concentration and mobility and TLM measurements are used to establish the electrical properties and attain contact resistivity of the contacts. We also discuss the temperature dependence of the Current-Voltage (*I*-*V*) characteristics and present a baseline for the formation of Ohmic contacts on a lightly P-doped diamond surface as opposed to a heavily doped surface. A schematic of the process flow is given below in Fig 3.2.1.

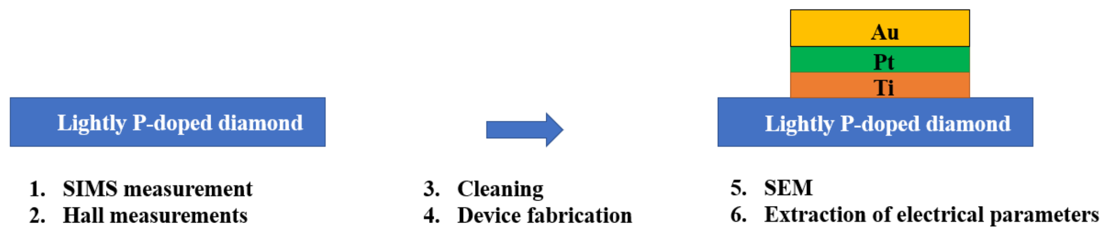

Figure 3.2.1: Process flow for lightly phosphorus-doped diamond study

3.3 Materials and Experimental Tools Used

Nanofab cleanroom reagents included sulfuric acid (H_2SO_4), hydrogen peroxide(H_2O_2), hydrofluoric acid (HF), ammonium hydroxide (NH_4OH) and deionized (DI) water for cleaning and LOR 3A, AZ 3312, MIF 300, and AZ 400T for photolithography. Titanium, platinum, and gold were during the metal deposition process.

Tools used for the fabrication, characterization and testing of the samples include:

- Pyrometer
- PECVD system
- Hall effect measuring system
- Dektak profilometer
- Secondary Ion Mass Spectrometer
- Spin coater
- Photolithography Aligner
- TLM mask
- Barrel asher
- Lesker e-beam evaporator
- Scanning electron Microscope
- Hot plate
- Electrical Probe station
- Optical microscopy

3.4 Experimental Procedure

CVD IIa (111) substrates were obtained from Excellent Diamond Products and loaded into a PECVD system. Before doping began, the substrates were treated in a hydrogen plasma environment for five minutes. The hydrogen flow rate was 400 sccm, microwave power of 2000 W, and a chamber pressure of 60 Torr. The phosphorus source used was a 200 ppm of trimethyl phosphine in a hydrogen gas (TMP/H_2) mixture. The TMP/H_2 cylinder was preheated to 36.7 °C, the mixing rail to 50 °C, and the hydrogen flow line to 74.7 °C before

being introduced to the chamber. The hydrogen flow rate was adjusted to 350 sccm, methane gas was introduced at a flow rate of 0.5 sccm, and a TMP/H_2 flow rate of 50 sccm. The substrate temperature was held at 809 °C, creating the necessary conditions for the phosphorus-doped layers. After about an hour, a film thickness of ~700 nm was obtained. The phosphorus concentration and depth into the epilayer were confirmed by SIMS using a Cameca 4F tool. Cs^+ ions were accelerated to 10 keV at an incident angle of 24.5° from the surface normal. The beam current was 1 µA, and the scan area was 220 µm by 220 µm.

Substrate cleaning started with 30 min HF-dip for 30 mins, followed by a 30-minute acid clean in a boiling mixture of 3:1 H_2SO_4/H_2O_2 solution, then a 30 min dip in a 3:1 boiling mixture of NH_4OH/H_2O_2 solution, and finally a 3:1 mixture of H_2SO_4/HNO_3 solution. For lithography, photoresist AZ3312 was spun onto the surface, and it was exposed for 6 seconds in an OAI 808 aligner with a mask that had TLM pad structures (Fig 3.4.1). After exposure, the sample was developed in MIF developer for 50 s. The sample was then treated in oxygen in a barrel Tegal asher for 60 s to improve metal contact adhesion to the diamond surface.

The metal stack Ti/Pt/Au at 50 nm/50 nm/200 nm thickness was deposited with a Lesker e-beam evaporator. The thick layer of gold was the electrical contact, platinum as a diffusion barrier, and titanium as an adhesion layer, as shown in Figs. 3.4.2 & 3.4.3. Deposition was followed by lift-off in AZ 400T stripper. Current-voltage (*I*-*V*) measurements were done with a Cascade probe station system in the low -1V to 1V region for the different spacings and the ICCap software was used to acquire the data from the measurements. Some samples were annealed at 700 °C for 60 mins in an AS-One rapid thermal processing system and remeasured in the probe station to investigate the changes in contact resistivity after anneals. SEM images of the contacts were taken after subsequent measurements(Fig. 3.4.4). After all measurements were done, the sample was cleaned using gold etchant type TFA (Transene) for 20 mins to remove the metallization, followed by a dip in HF for 30 mins, then cleaning in a boiling mixture of H_2SO_4/HNO_3 solution for 30 mins. The sample was verified to be clean using a light microscope. Van der Pauw Hall measurements were taken using an Ecopia Hall Effect HMS 5000 system to extract the free carrier concentrations and room temperature Hall mobilities.

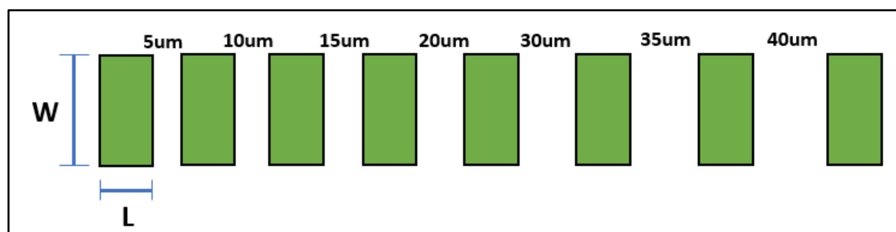

Figure 3.4.1: Schematic of TLM structure

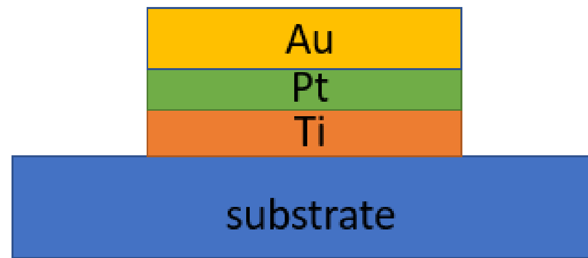

Figure 3.4.2: Device stack showing contact formation

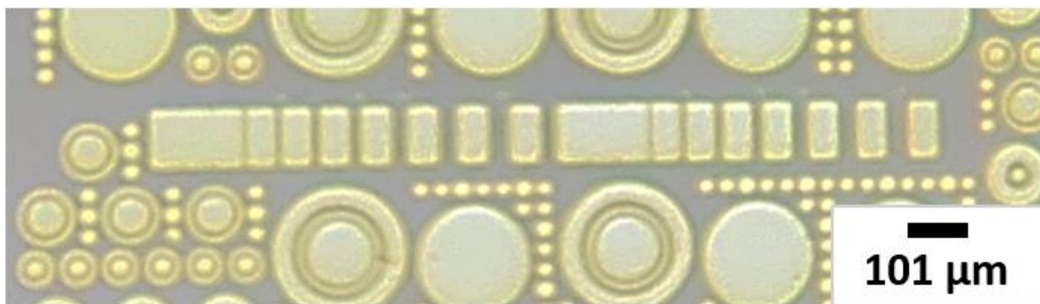

Figure 3.4.3: Optical Microscopy of TLM contacts after metal deposition

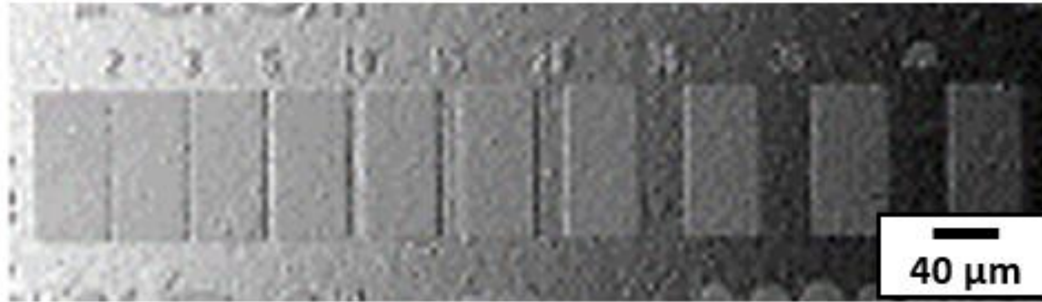

Figure 3.4.4: SEM showing TLM devices

3.5 Experimental Results and Discussion

3.5.1 SIMS Analysis

Results from SIMS analysis showed phosphorus incorporation of ~5E+18 atoms/cm^3 as shown in Fig. 3 and is within the range of values generally considered for light phosphorus doping [10, 12, 13-15]. The doping profile can also be seen to be relatively uniform in the film, and this can be attributed to the fine tuning of the doping process by preheating the TMP cylinder and other gas lines and adjusting the different gas flow rates to ensure that the environment for growth remained constant and optimum throughout. The resulting depth is about 700 nm after which the concentration falls below 1E+15 atoms/cm^3. Uniform doping concentration in the epilayers give rise to better *I-V* measurements and parameters [17-20].

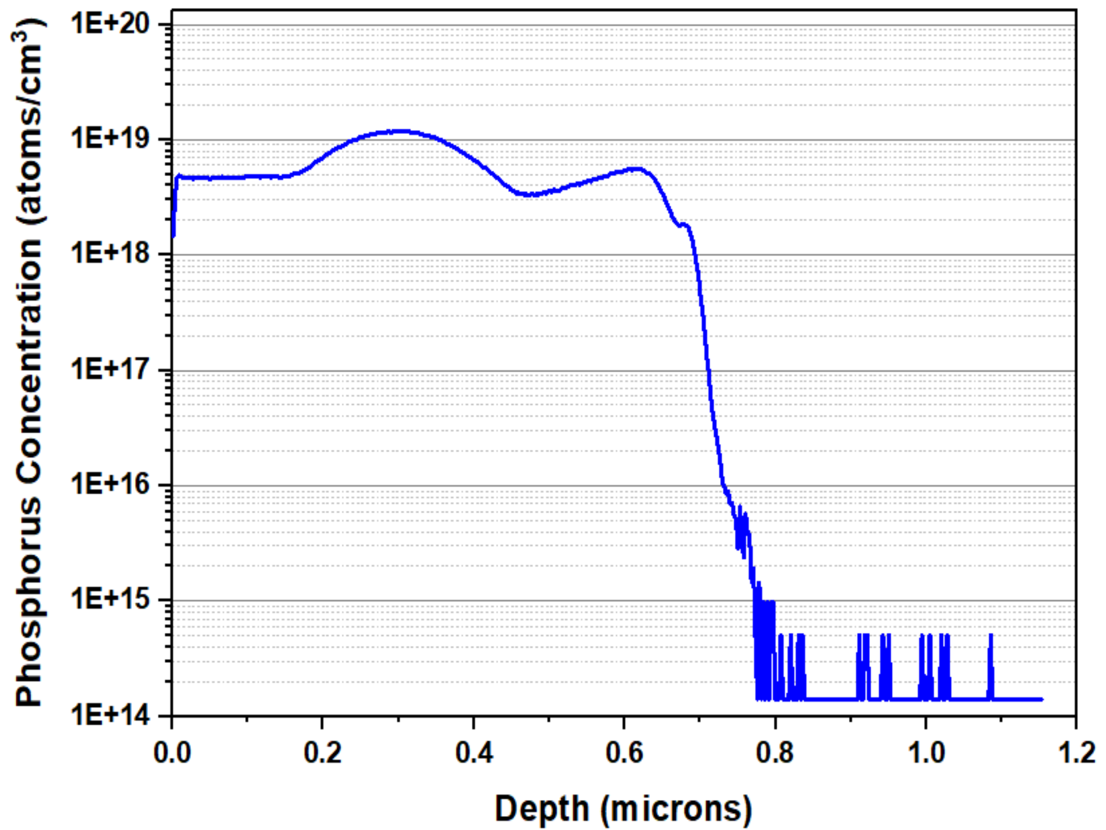

Figure 3.5.1: SIMS profile showing phosphorus concentration in diamond film

3.5.2 IV Measurement and Analysis

Results from the current-voltage measurements prior to annealing (Fig. 3.5.2) showed non-ideal behaviour across all the spacings over the low range of voltages. This non-ideal Ohmic behaviour became more pronounced at higher voltages. However, the parameters extracted were limited to the linear regions using fits with R-squared values greater than 0.9, which indicates a good fit with little variance between the points. This phenomenon of non-ideal behaviour can be attributed to the presence of defects within the deposited layers, residual polymeric photoresist on the surface, the formation of a Schottky contact, and the absence of a good adhesion between the titanium layer and the diamond surface [21-23]. Furthermore, the current passing through the contacts was very small. After annealing at 700 °C for 60 mins, the contacts became Ohmic and linear within the voltage range and showed more consistent behaviour. The current decreased for increasing spacing as shown in Fig 3.5.3. This is due to the possible formation of the very conductive titanium carbide [3, 17, 24-28] at the diamond interface and the removal of point defects. In addition, thermal anneals increase the strength of metal films by reducing dislocation emission, increasing the rate of grain size growth which in turn strengthens the metal grain boundaries from cracks [29-33] The contribution from possible impurities in the titanium metal can also not be ruled out as they can further lead to an increase in conductivity [15]
.

In Figs. 3.5.4 and 3.5.5, the slopes of the *I-V* plots were used to extract the total resistance according to Ohms Law [13, 34] and the resulting total resistance versus spacing for the unannealed and annealed cases, respectively. Linear fits were used to extract the contact resistance (Eqn. 1), transfer length (Eqn. 2), the sheet resistance (Eqn. 3), resistivity (Eqn.

4), and finally the contact resistivity (Eqn. 5) for the unannealed and annealed conditions. The values are tabulated in Table 3.1 and showed a contact resistivity of 2.17E+02 Ωcm^2 before annealing and 9.88E-02 Ωcm^2 after annealing, which is more than two orders of magnitude lower. Just as stated before, the annealing process improved the electrical conductivity, which led to a decrease in contact resistivity. This value after annealing was the lowest among previous values of 1.00E+05 Ωcm^2 reported by Kato *et al.* [12], 4.80E+06 Ωcm^2 by Teraji *et al.* [13], 2.80E+05 Ωcm^2 by Teraji *et al.* [14] and 1.00E-01 Ωcm^2 by Takemasa *et al.* [15]. The high resistivity values prior to annealing are associated with adhesion issues, defect states, and contacts-diamond imperfection at the interface were confirmed with Hall measurements.

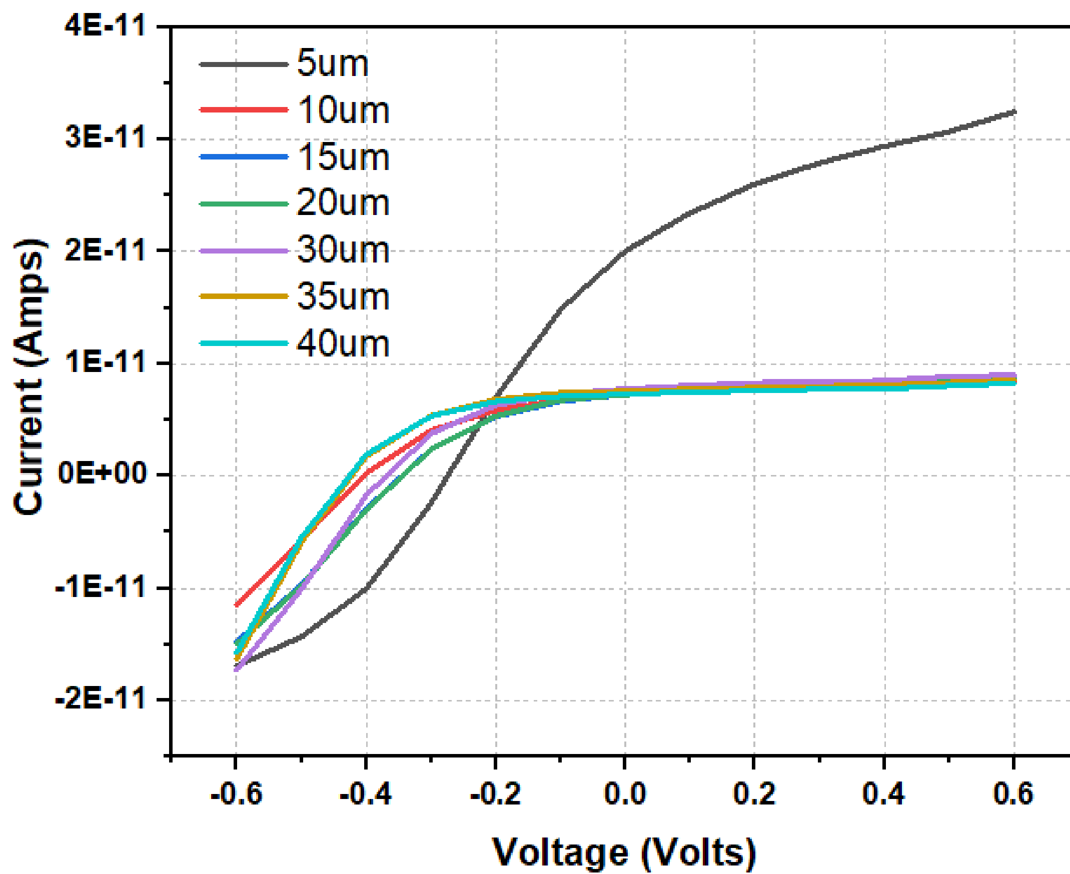

Figure 3.5.2: I-V plots showing different spacings before the anneal

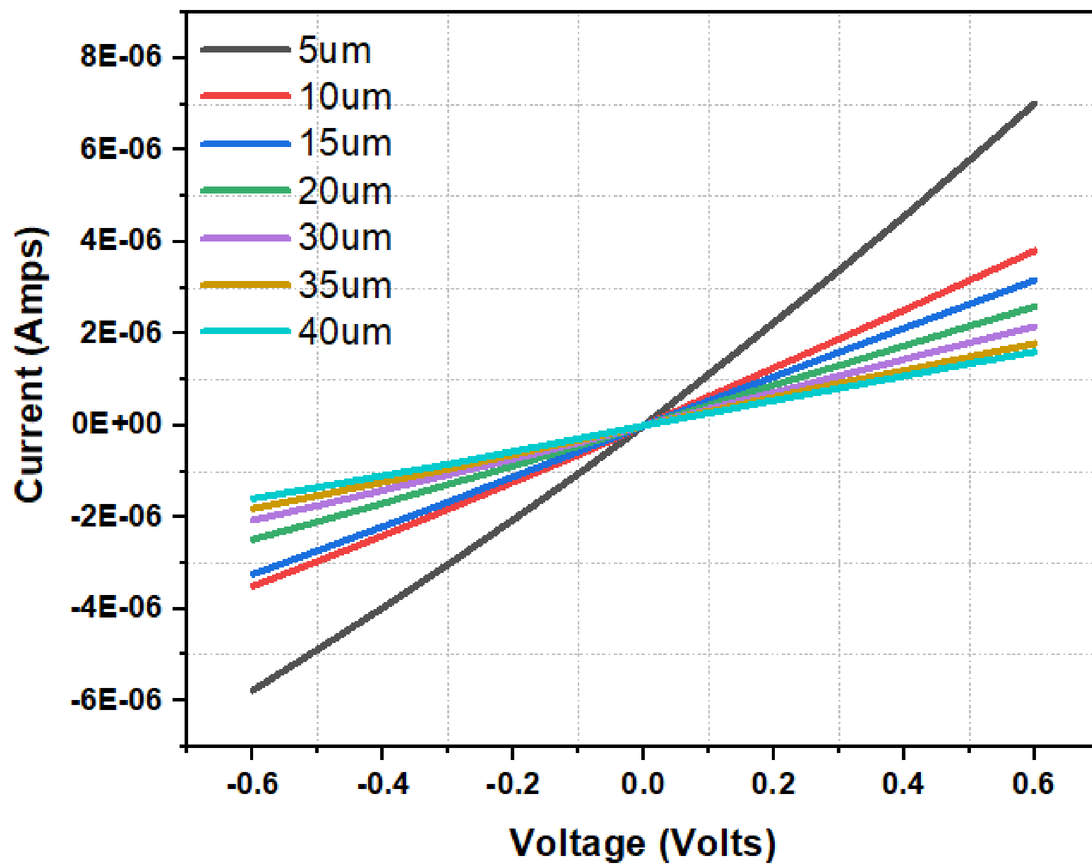

Figure 3.5.3: I-V plots showing different spacings after the 700 °C anneal for 60 mins

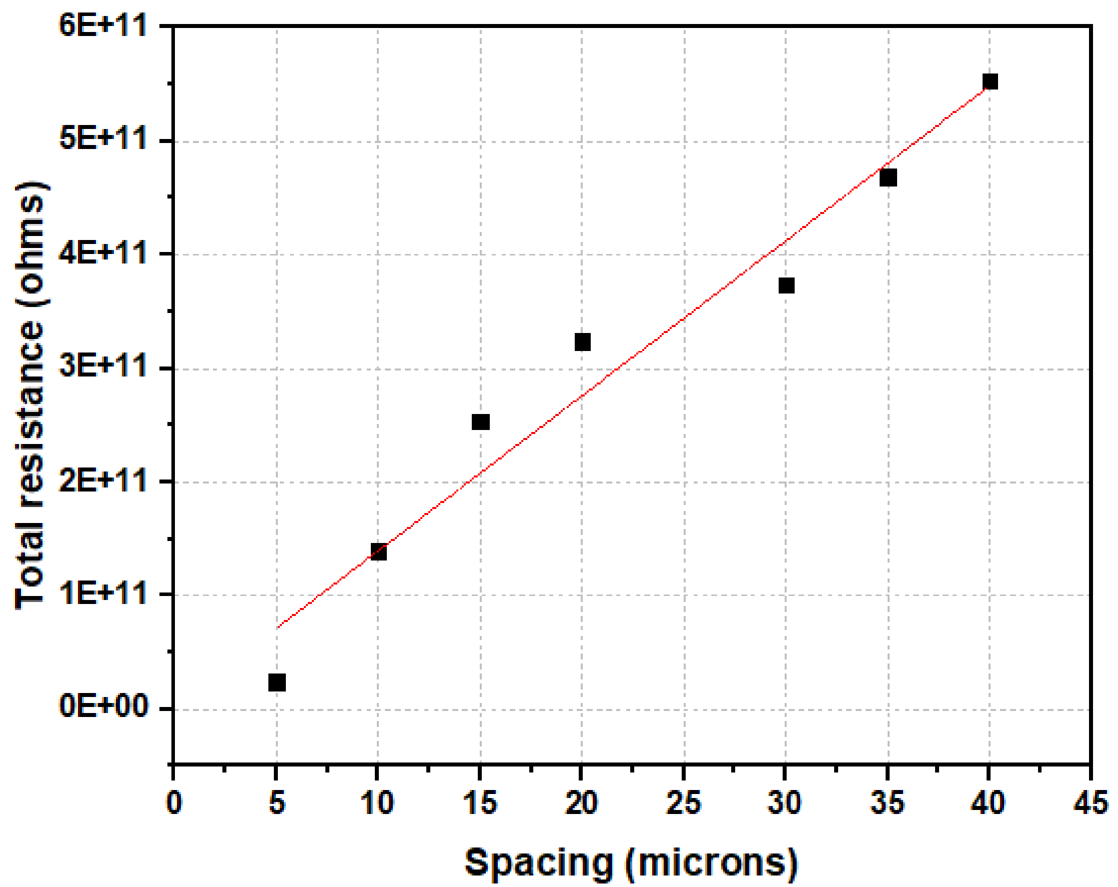

Figure 3.5.4: Plot of total resistance vs spacing prior to annealing

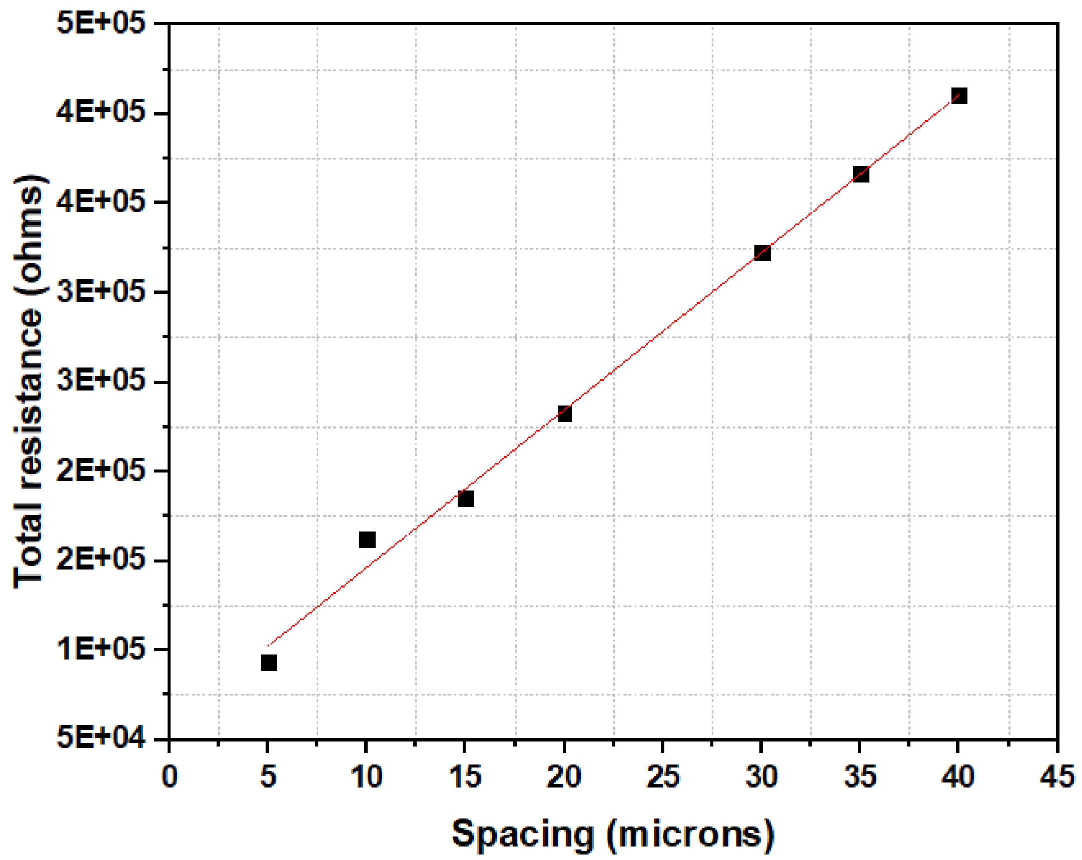

Figure 3.5.5: Plot of total resistance vs spacing after a 700 °C anneal

EQUATIONS:

Contact resistance

$$R_c = \frac{y\ intercept}{2} \qquad (1)$$

Transfer length

$$L_t = \frac{y\ intercept}{2 \times slope} = \frac{x\ intercept}{-2} \qquad (2)$$

Sheet resistance

$$R_s = slope\ \times width\ of\ contact \qquad (3)$$

Resistivity

$$\rho = R_s \times epilayer\ thickness \qquad (4)$$

Specific contact resistance

$$\rho_c = R_c \times L_t \times width\ of\ contact \qquad (5)$$

Table 3.1: Extracted Electrical Parameters

Temp [°C]	Contact resistance [Ω]	Transfer length [μm]	Sheet resistance [Ω/□]	Resistivity [Ωcm]	Contact resistivity [Ωcm^2]
room	1.71E+09	0.126	1.37E+12	9.62E+07	2.17E+02
700	29.3E+03	3.33	8.89E+05	62.2	9.88E-02

Values of phosphorus concentration and contact resistivity for previous works are shown in Table 3.2 and plotted in Fig. 3.5.6 in order to observe any trends. It can be seen from Fig. 3.5.6 that over the years, for the same range of phosphorus doping, the contact resistivity has reduced significantly. This can be attributed to the fine-tuning of the doping process to attain more consistently doped films, the improvement of fabrication procedures such as cleaning, lithography, and low to high vacuum metal deposition.

Table 3.2: Comparison of Extracted Values from Work on Lightly Doped Diamond and Current Work

Work	**Phosphorus concentration [atoms/cm^3]**	**rho-c [Ωcm^2]**
Kato *et al.* [12]	8.00E+18	1.00E+05
Teraji *et al.* [13]	3.00E+18	4.80E+06
Teraji *et al.* [14]	1.00E+19	2.80E+06
Takemasa *et al.* [15]	5.00E+19	1.00E+00
This work	5.00E+18	9.88E-02

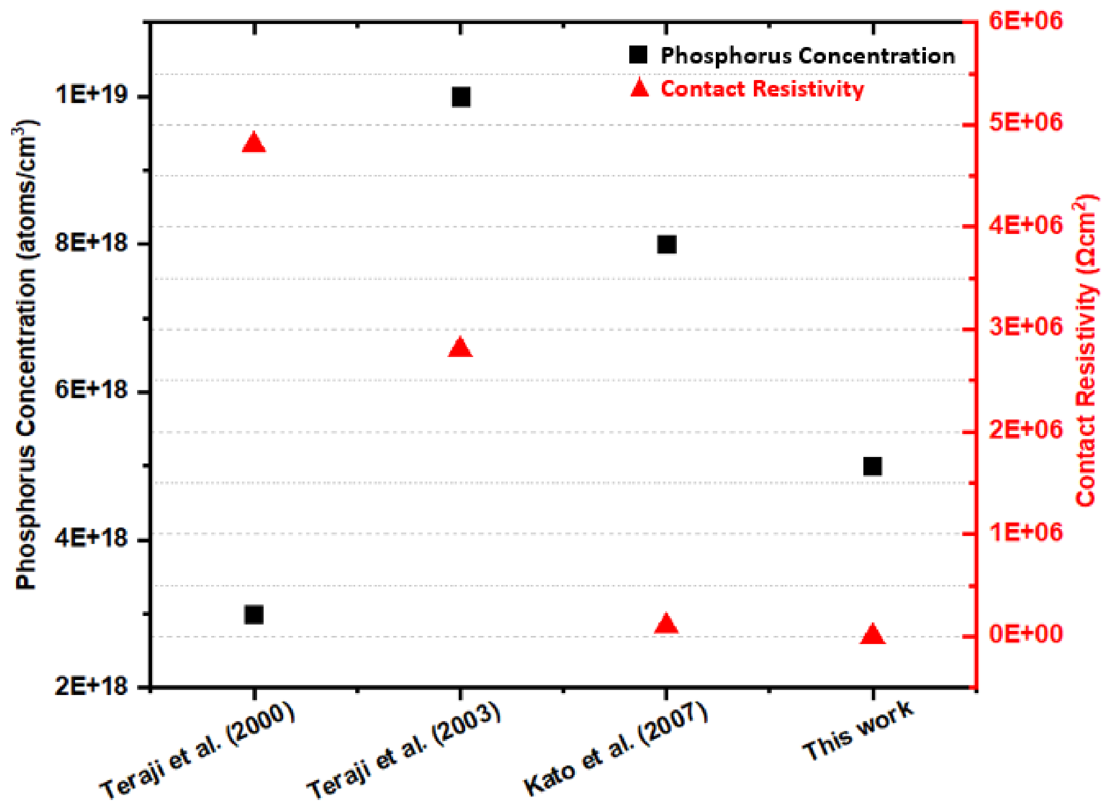

Figure 3.5.6: Plot comparing lightly doped diamond measurements with contact resistivity values over the years

3.5.3 Hall Effect Analysis

Four-point Hall effect measurement using the setup in Fig. 3.5.7 showed an average free carrier concentration of -1.11E+15 cm^{-3}. The negative sign is good evidence of n-type conduction in the diamond. The average Hall mobility was found to be 109 cm^2/Vs.

Figure 3.5.7**:** Van der Pauw measurement sample holder

3.6 Conclusions

A trilayer metal contact Ti/Pt/Au was studied on a lightly P-doped (111) diamond layer. SIMS analysis showed a uniform doping profile in the epilayer with an average concentration of 5E+18 atoms.cm^{-3}, and TLM measurements resulted in a low contact resistivity value of 9.88E−02 Ωcm^2 after annealing for an hour at 700 °C, which is close to values achieved for heavily doped layers [35]. This value is the lowest contact resistivity value achieved among lightly P-doped diamond layers. The low values are attributed to the improvements to the doping process to grow efficient surfaces, which were previously thought to be less conductive.

3.7 References

[1] Teraji, T., Koizumi, S., Mita, S., Sawabe, A., & Kanda, H. (1999). Electrical contacts for n-type diamond. *Japanese journal of applied physics*, *38*(10A), L1096

[2] Kato, H., Oyama, K., Makino, T., Ogura, M., Takeuchi, D., & Yamasaki, S. (2012). Diamond bipolar junction transistor device with phosphorus-doped diamond base layer. *Diamond and related materials*, *27*, 19-22.

[3] Moazed, K. L., Nguyen, R., & Zeidler, J. R. (1988). Ohmic contacts to semiconducting diamond. *IEEE electron device letters*, *9*(7), 350-351.

[4] Kato, H., Umezawa, H., Tokuda, N., Takeuchi, D., Okushi, H., & Yamasaki, S. (2008). Low specific contact resistance of heavily phosphorus-doped diamond film. *Applied Physics Letters*, *93*(20), 202103

[5] Shimaoka, T., Liao, M., & Koizumi, S. (2022). n-Type Diamond Metal-Semiconductor Field-Effect Transistor with High Operation Temperature of 300° C. *IEEE Electron Device Letters*, *43*(4), 588-591.

[6] Kato, H., Takeuchi, D., Tokuda, N., Umezawa, H., Okushi, H., & Yamasaki, S. (2009). Characterization of specific contact resistance on heavily phosphorus-doped diamond films. *Diamond and Related Materials*, *18*(5-8), 782-785

[7] Arora, N. D., Hauser, J. R., & Roulston, D. J. (1982). Electron and hole mobilities in silicon as a function of concentration and temperature. *IEEE Transactions on electron devices*, *29*(2), 292-295.

[8] Gross, W. J., Vasileska, D., & Ferry, D. K. (1999). A novel approach for introducing the electron-electron and electron-impurity interactions in particle-based simulations. *IEEE Electron Device Letters*, *20*(9), 463-465.

[9] Nesladek, M. (2005). Conventional n-type doping in diamond: state of the art and recent progress. *Semiconductor Science and Technology*, *20*(2), R19.

[10] Koizumi, S., Kamo, M., Sato, Y., Ozaki, H., & Inuzuka, T. (1997). Growth and characterization of phosphorous doped {111} homoepitaxial diamond thin films. *Applied Physics Letters*, *71*(8), 1065-1067.

[11] Katagiri, M., Isoya, J., Koizumi, S., & Kanda, H. (2004). Lightly phosphorus-doped homoepitaxial diamond films grown by chemical vapor deposition. *Applied physics letters*, *85*(26), 6365-6367.

[12] Kato, H., Makino, T., Yamasaki, S., & Okushi, H. (2007). n-type diamond growth by phosphorus doping on (0 0 1)-oriented surface. *Journal of Physics D: Applied Physics*, *40*(20), 6189.

[13] Teraji, T., Koizumi, S., & Kanda, H. (2000). Ga Ohmic contact for n-type diamond by ion implantation. *Applied Physics Letters*, *76*(10), 1303-1305.

[14] Teraji, T., Katagiri, M., Koizumi, S., Ito, T., & Kanda, H. (2003). Ohmic contact formation for N-type diamond by selective doping. *Japanese journal of applied physics*, *42*(8A), L882.

[15] Takemasa, A., Kakushima, K., Sugii, N., Nishiyama, A., Tsutsui, K., Natori, K., & Iwai, H. (2014). Electrical characteristics of n-type

[16] Schroder, D. K. (2015). *Semiconductor material and device characterization*. John Wiley & Sons.

[17] Chen, Y., Ogura, M., Yamasaki, S., & Okushi, H. (2005). Ohmic contacts on p-type homoepitaxial diamond and their thermal stability. *Semiconductor science and technology*, *20*(8), 860

[18] Kato, H., Futako, W., Yamasaki, S., & Okushi, H. (2004). Homoepitaxial growth and characterization of phosphorus-doped diamond using tertiarybutylphosphine as a doping source. *Diamond and related materials*, *13*(11-12), 2117-2120.

[19] Mircea, A., Ougazzaden, A., & Mellet, R. (1989). Very uniform epitaxy. *Progress in crystal growth and characterization*, *19*(1-2), 39-49.

[20] Benda, H., & Spenke, E. (1967). Reverse recovery processes in silicon power rectifiers. *Proceedings of the IEEE*, *55*(8), 1331-1354.

[21] Hu, C. (1979). Optimum doping profile for minimum Ohmic resistance and high-breakdown voltage. *IEEE Transactions on Electron Devices*, *26*(3), 243-244.

[22] Todeschini, M., Bastos da Silva Fanta, A., Jensen, F., Wagner, J. B., & Han, A. (2017). Influence of Ti and Cr adhesion layers on ultrathin Au films. *ACS applied materials & interfaces*, *9*(42), 37374-37385.

[23] Cordill, M. J., Bahr, D. F., Moody, N. R., & Gerberich, W. W. (2004). Recent developments in thin film adhesion measurement. IEEE Transactions on Device and Materials Reliability, 4(2), 163-168.

[24] Agarwal, S., Prajapati, Y. K., & Maurya, J. B. (2016). Effect of metallic adhesion layer thickness on surface roughness for sensing application. IEEE Photonics Technology Letters, 28(21), 2415-2418.

[25] Werner, M. (2003). Diamond metallization for device applications. Semiconductor science and technology, 18(3), S41.

[26] Tachibana, T., Williams, B. E., & Glass, J. T. (1992). Correlation of the electrical properties of metal contacts on diamond films with the chemical nature of the metal-

diamond interface. II. Titanium contacts: A carbide-forming metal. Physical Review B, 45(20), 11975.

[27] Lavrenko, V. A., Glebov, L. A., Pomitkin, A. P., Chuprina, V. G., & Protsenko, T. G. (1975). High-temperature oxidation of titanium carbide in oxygen. Oxidation of Metals, 9(2), 171-179.

[28] Leroy, W. P., Detavernier, C., Van Meirhaeghe, R. L., Kellock, A. J., & Lavoie, C. (2006). Solid-state formation of titanium carbide and molybdenum carbide as contacts for carbon-containing semiconductors. Journal of applied physics, 99(6), 063704.

[29] Gildenblat, G. S., Grot, S. A., Hatfield, C. W., Badzian, A. R., & Badzian, T. (1990). High-temperature Schottky diodes with thin-film diamond base. IEEE electron device letters, 11(9), 371-372.

[30] Fullman, R. L., & Fisher, J. C. (1951). Formation of annealing twins during grain growth. Journal of Applied Physics, 22(11), 1350-1355.

[31] Ralph, B. (1990). Grain growth. Materials Science and Technology, 6(11), 1136-1144.

[32] Thompson, C. V. (1990). Grain growth in thin films. Annual review of materials science, 20(1), 245-268.

[33] Sarah, M. S. P., Musa, M. Z., Asiah, M. N., & Rusop, M. (2010, April). Electrical conductivity characteristics of TiO 2 thin film. In 2010 International Conference on Electronic Devices, Systems and Applications (pp. 361-364). IEEE.

[34] Tenny, K. M., & Keenaghan, M. (2017). Ohms Law.

[35] Kato, H., Makino, T., Ogura, M., Tokuda, N., Okushi, H., & Yamasaki, S. (2009). Selective growth of buried n+ diamond on (001) phosphorus-doped n-type diamond film. Applied Physics Express, 2(5), 05550

CHAPTER 4

HAFNIUM AS A SUBSTITUTE CONTACT TO (100) NANOCARBON SURFACES

4.1 Introduction to Transition Metal Carbides

The criteria for selecting metal contacts for devices include the ability to be inert/passive during operation, good electrical conductivity and compatibility with the different processing steps[1]. As compared to other semiconductor materials, the main challenges in developing metal contacts for diamond include the material hardness and the nonuniformity of natural diamond, challenges from metal-semiconductor adhesion issues where there is a difficulty in finding materials that adhere well to the non-uniform diamond surface and do not delaminate during subsequent processing [2-5]. It is found in the literature however, that metal carbides may have increased adhesion over non-carbide forming materials systems and can act as a diffusion barrier as well [6-7]. Transition metal carbides typically combine desired properties such as high melting points, hardness, good conductivity, and good adhesion [8-10]. Most of the work done on doped diamond-related work have mostly employed the use of titanium as the adhesion layer contact due to its excellent ability to form a conductive carbide at the interface after annealing and its high strength-to-density ratio [10-12]. Others have used combinations of titanium and other metals such as platinum (Pt), gold (Au), palladium (Pd), rhodium (Rh), ruthenium (Ru), nickel (Ni), tungsten (W), cobalt (Co), tantalum (Ta), chromium (Cr), yttrium (Y), molybdenum (Mo), zirconium (Zr), and many other transition metals[13] as the contact to diamond directly, or as passivating layers and capping layers in bi-layer or tri-layer configurations. Besides carbide forming metals, contacts have also been achieved by using

silver paint or by damaging the surface of diamond to create electrically active defects. This also leads to the formation of weak graphitic structures at the interface, which reduces adhesion and compromises the strength of the device and so carbide formation is the most preferred route for obtaining both good Schottky and Ohmic contacts.

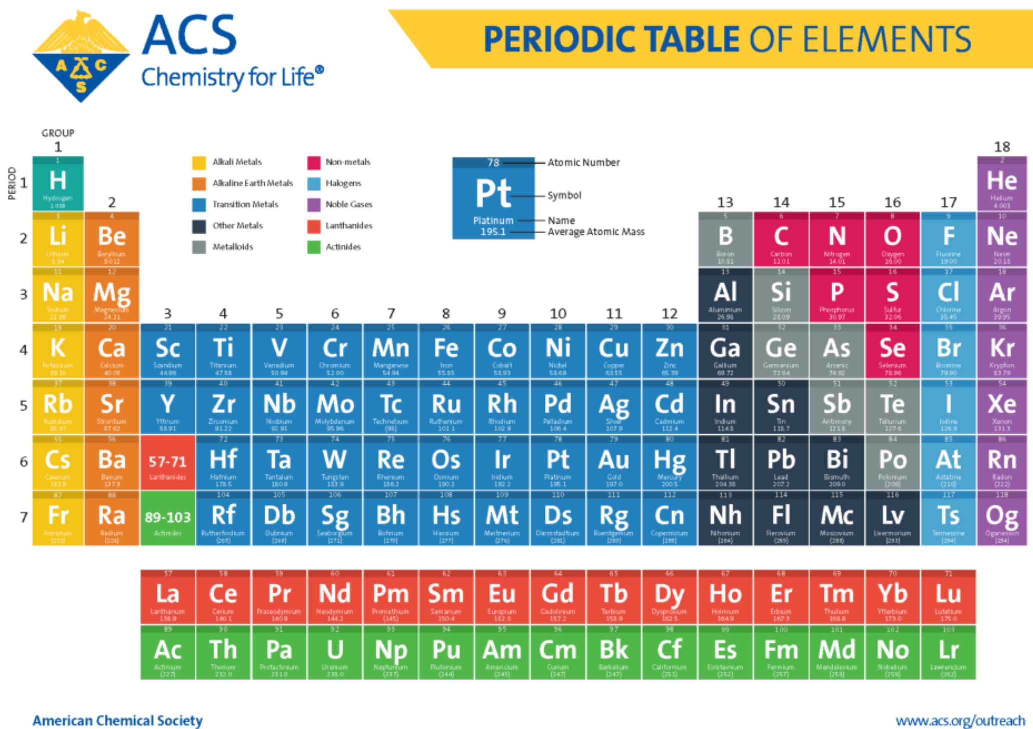

Figure 4.1.1: Periodic table of elements[13]

4.2 Previous Work on Carbide Forming Contacts

Prior work by Cappelli *et al.* developed a method for using tungsten carbide (WC) as a stable Schottky contact on p-type diamond due to beneficial properties such as good electrical conductivity, thermal stability, and high melting temperature[14]. Vardi *et al.* in their work also reported the creation of self-aligned Ohmic contacts to hydrogen-terminated p-type diamond; reporting a contact resistance of about 2.6 Ωmm after a thermal process leads to the formation of the very conductive WC[15]. Further, Teraji et al. used vacuum ultraviolet light irradiation to fabricate room-temperature Schottky diodes for boron-doped diamond with Au contacts[16]. Xing *et al.* studied Pd as a contact down to cryogenic temperatures of about 4K and discovered that it forms an Ohmic contact on hydrogen-terminated p-type diamond and reported contact resistivity values in the range of 10^{-4} to 10^{-3} Ωcm^2 between 300K and 4K and values of 10^{-6} Ωcm^2 at 700°C where there is the possibility of carbide formation[17]. Ion beam mixing at 700°C was attributed to the formation of SiC at the interface between silicon and diamond, which was an ohmic contact in work by Fang *et al.*[18]. Drozdov *et al.* also formed Ohmic contacts using Mo/Ti where carbide formation between titanium and diamond occurs during laser annealing[19]. Finally, Das *et al.* [20], Venkatesan *et al.* [21], and Jingu *et al.* [22] utilized Ti/Au metallization for contact formation and report contact resistivities of $\sim10^{-6}$ Ωcm^2 , $\sim10^{-6}$ Ωcm^2 at 850 °C, and $\sim10^{-7}$ Ωcm^2, respectively. Even though the use of carbide-forming transition metals been very attractive avenue, it can be seen that the eutectic reactions that lead to the formation of the metal carbides occur at a much higher temperature compared to the eutectic reactions for silicides for instance, and at such high temperatures, the risk of interdiffusion between the different metals and the formation of metal oxides instead of

carbides[19] becomes more apparent. Prior to this work, for example, it was confirmed that Ti/Au contacts typically suffer from poor adhesion and at annealing temperatures, interdiffusion of the metals occurred just as demonstrated in some literature [19-22]. The use of Ti/Al/Au layers also risked the formation of the high-resistance compound TiAl at the interface [23, 24]. Another metallization that was tried was Ti/Cr/Au, and it was discovered that Cr was very mobile in Au at high anneal temperatures via grain boundary diffusion and forms a high-resistance oxide Cr_2O_3[1].

4.3 The Choice of Hafnium as a Contact

In the quest to test a carbide-forming transition metal as a contact to nanocrystalline diamond, we first looked at correlations drawn for transition metal silicides to determine the factors involved. Previous studies done by Ottaviani *et al.* [25] for silicides showed a linear relationship between silicide barrier height and both enthalpy of formation and eutectic temperature. In their work, they investigated a property that dominates the barrier height, which was found to be the interfacial layer attained as a result of the reaction between the two solids: the substrate and the metal contact. This observation led to the correlation of the barrier height to the eutectic temperature instead of a bulk property like the enthalpy of formation. For transition metal silicide contacts, it was found by Andrews *et al.* [26] that the change in the heat of formation is proportional to the barrier height. This data is shown in Figure 4.3.1.

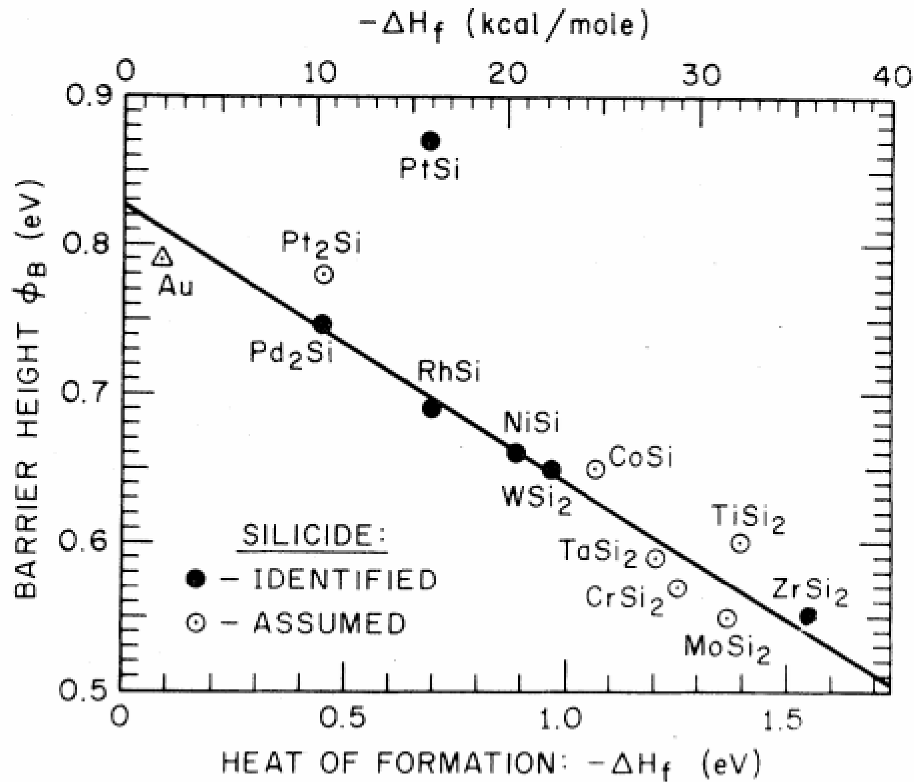

Figure 4.3.1: Plot of barrier height vs. ΔH_f for silicide formation [26].

To narrow it down further, since titanium has been extensively used and found to be a good contact, a transition metal with similar properties to titanium was desired. Since elements in the same group share similar properties, Zr, Hf, and Rf were of interest. However, Rf is radioactive so that was eliminated from the search leaving Zr and Hf. Comparing their predicted heats of formation of the different types of possible carbides (metal rich, 1:1 and carbon rich), a table (Table 4.1) can be generated which leads to the selection of hafnium and zirconium as good candidates for metal contact studies since they have the lowest values[27]. Hafnium is the 45th most abundant element on earth and is a high melting point (2233 °C), corrosion resistant, ductile metal typically used in the fabrication of nuclear

control rods, in plasma welding torches, and in integrated circuits[28]. Zirconium on the other hand is chemically similar to hafnium with a high melting point of about 1852 °C, usually used in refractory and opacifier applications [29]. In practice however, due to the chemical similarities between the two metals and the fact that they are usually found contaminated with each other, hafnium and zirconium are very difficult to separate [28]. Further, the carbide formed between hafnium and carbon is known to be the most refractory binary compound with a melting point of about 3928 °C [30]. As a result of these desirable properties, hafnium was selected as the transition metal to be tested as a possible contact on nanocarbon diamond to investigate its contact properties.

Table 4.1: Enthalpy of Formation for Transition Metal Carbides Found in the Ti-Zr-Hf Group. *No Data Found for Rf Carbides.

Metal	M_2C [kJ/mol]	MC [kJ/mol]	MC_2 [kJ/mol]
Ti	-56	-81	-97
Hf	-57	-85	-91
Zr	-61	-92	-101

Hence, just like was done for the contact study of Ti/Pt/Au on nanoC as shown in Fig 4.3.2, a trilayer metal contact was formed for the first-time using hafnium, platinum, and gold (Hf/Pt/Au) and was deposited on nanocrystalline diamond using the transfer length method (Fig 4.3.3). Initial XPS measurements are done to confirm the deposition of hafnium, SEM and optical microscopy images are presented. Electrical measurements are discussed which show the possibility of using hafnium as a contact and limitations suggestions for future tests are outlined.

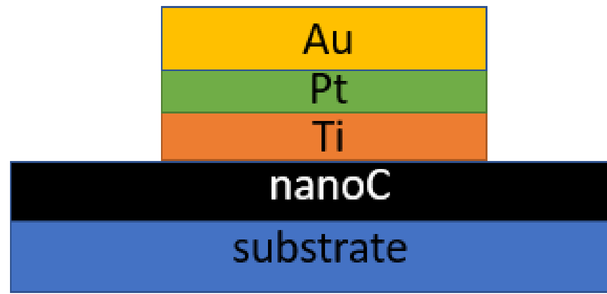

Figure 4.3.2: Schematic of previous study of the contact Ti/Pt/Au on nanoC

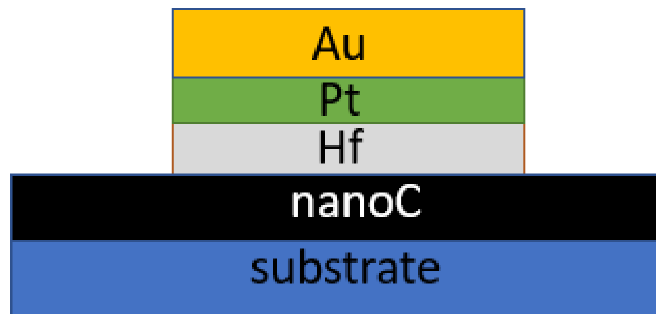

Figure 4.3.3: Schematic of study of Hf/Pt/Au on nanoC in this work

4.4 Materials Used

Cleaning materials were sourced from the Nanofab cleanroom and were sulfuric acid (H_2SO_4), hydrogen peroxide(H_2O_2), ammonium hydroxide (NH_4OH), hydrofluoric acid (HF), acetone, isopropyl alcohol (IPA) and deionized (DI) water. LOR 3A, AZ 3312, MIF 300, and AZ 400T were used for the lithography process and the metals hafnium, platinum and gold were used for the deposition process.

4.5 Experimental Tools

Tools used for the fabrication, characterization and testing of the samples include:

- PECVD system
- Hall effect measuring system
- Dektak profilometer
- Secondary Ion Mass Spectrometer
- Spin coater
- Photolithography Aligner
- TLM mask
- Barrel asher
- Lesker e-beam evaporator
- Lesker sputterer
- Scanning electron Microscope
- Hot plate
- X-ray Photoelectron Spectrometer
- Electrical Probe station
- Optical microscope

4.6 Experimental Process

The experimental process was in two parts: first to confirm the deposition of hafnium on the diamond surface and second to repeat the TLM contact formation process on nanoC diamond. To begin, undoped 5mm x 5mm samples were obtained from Element 6 and cleaned aggressively with 3:1 acid piranha solution ($H_2SO_4 + H_2O_2$) for 20 mins, followed by a 20 mins HF dip, then a clean in 80 °C base piranha solution ($NH_4OH + H_2O_2$) for 20 mins and finally with a boiling mixture of HNO3 + H_2SO_4 for 20 mins at 150 °C. An image of the cleaned surface is shown in Fig 4.6.1. Next, half of one sample was masked as a reference for the thickness, and another bare sample were loaded into Lesker Sputtering tool and pumped down to 3.6 E-07 Torr after about 12 hours. This was to eliminate as much oxygen as possible from the chamber to reduce the likelihood of the formation of hafnium oxide during deposition. 5nm of hafnium was deposited using a DC gun at a rate of 1.0 A/sec. The previously bare sample was then quickly put under vacuum in a desiccator to avoid air exposure, and a profilometer was used to confirm the thickness of the hafnium film. The hafnium-deposited film and another clean bare sample were then loaded into a Kratos Axis Supra$^+$ XPS system and measurements were taken to investigate the elements present and their chemical states.

Separately, the nanocarbon growth was done as follows: intrinsic diamond substrates obtained once again from Element 6 were cleaned using a boiling mixture of 3:1:1 $H_2SO_4/H_2O_2/H_2O$ at 220°C for 15 min, then a 5 min treatment in HF and finally boiling for 15 min in a mixture of 1:1:5 $NH_4OH:H_2O_2: H_2O$. The substrate was rinsed in DI water between each acid boiling step. The nanoC layers were grown using a plasma-enhanced

CVD system. The ASTeX AX5000 reactor had an inductively heated sample stage. Samples were grown at a microwave power of 900 W, pressure of ~20 Torr and the deposition process occurred at temperatures around 900°C read by optical pyrometer. For the gas flow rates, 100 sccm of nitrogen, 10 sccm of argon, 20 sccm of methane, and 5 sccm of hydrogen were used. After a 30 min deposition, the resulting nanoC layer had a thickness of about 300 nm. The nitrogen incorporation of about ~6×10^{20} cm^{-3} [31, 32] attained by secondary ion mass spectroscopy (SIMS) using a Cameca 4F tool. The incident Cs^{+} ions were accelerated to an energy of 10 keV. The ion beam had an incident angle of 24.5° from the surface normal and a beam current of 1 μA. The raster scan area was approximately 220 μm by 220 μm.

These nanoC samples were measured with an Ecopia Hall Effect HMS 5000 system to extract the Hall properties using the Van der Pauw configuration using the ECOPIA SPCB-001 sample mount shown in Fig 4.6.2. Since some of the samples from the same batch of grown nanocarbon samples were tested using XRD and Raman, it was skipped for these experimental samples. Preliminary SEM micrographs were taken of the nanocarbon surface as well using a Phenom Pro tabletop SEM and a Zeiss Auriga SEM/EDS system as shown in Fig 4.7.6.

The TLM structures on the nanocarbon samples were fabricated as follows. Photoresist AZ3312 was spun on the surface and exposed for about 5.7 sec in an OAI 808 aligner with a mask containing TLM pad structures and developed with MIF 400 developer for about 40 seconds. The sample was treated in oxygen for about 60 seconds in a barrel Tegal asher to enhance metal contact adhesion. The sample was then loaded into the Lesker Sputtering

tool and 50 nm of hafnium was deposited. Afterward, the sample was transferred to the Lesker e-beam evaporator and 50 nm of platinum and 200 nm of Au were deposited at a vacuum of about 1 e-06 Torr to give the resulting tri-layer metal stack Hf/Pt/Au. Hf served as the adhesion layer, Pt as the diffusion barrier, and Au as the electrical contact as shown in the schematic in Fig 4.3.3. After all the metal deposition was done, lift-off was done with AZ 400T stripper to remove the remaining photoresist and metal, leaving the metals only at the TLM structures. A 30-minute rapid thermal anneal was done in nitrogen ambient at 800 °C to diffuse any excess oxygen out of the metals using an AS-One RTP system. Current-voltage *(I-V)* measurements were made using a Cascade probe station system with voltages between -5V and 5V. IC-Cap software was used for the I-V data acquisition.

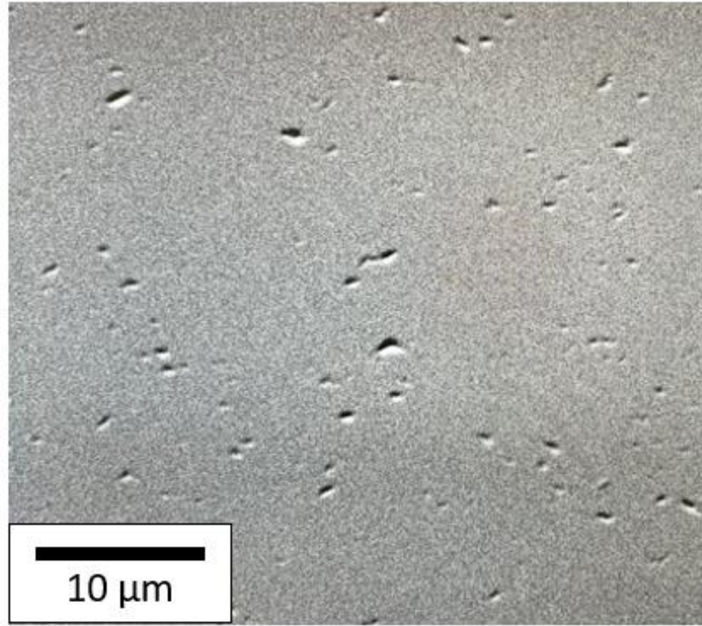

Figure 4.6.1: Surface of cleaned Element 6 diamond sample

Figure 4.6.2: Hall Effect ECOPIA SPCB-001 sample mount

4.7 Results and Discussion

4.7.1 XPS Results for Deposition of Hafnium

The XPS results before hafnium deposition (pre-deposition) and after hafnium deposition on the undoped samples are outlined in Figs 4.7.1 to 4.7.5. The wide scan comparing the two instances is shown in Fig 4.7.1 and Fig 4.7.2 shows the different peak labels for the comparison. The carbon Auger peak (C *KLL*) at 1223.69 eV, the oxygen Auger peak (O *KLL*) at 983 eV, Hf 4s at 538 eV, O 1s at 532 eV, Hf 4p peaks between 300 to 435 eV, C 1s at 284 eV, Hf 4d peaks between 214 -225 eV, O 2s at 24 eV, and Hf 5s, 5p, and 4f peaks between 18 eV and 65 eV. Straight away we can see that the bare substrate does not have any hafnium present, as seen in Fig 4.7.2, verified in Fig 4.7.5; where, there is no Hf 4f doublet on the bare diamond. The wide spectrum of the hafnium-deposited sample also shows more chemical bonding states than the bare diamond. Further, from Fig 4.7.3 it can be seen that prior to any hafnium deposition, there is a little amount of oxygen which usually comes from bonding states from contaminant particles from handling and cleaning. In contrast, the hafnium sample has a taller peak due to the presence of the native oxide of hafnium formed on the surface. It can be seen that the bonding state of the hafnium oxide is shifted to the right of the oxygen peak, which means most of the oxygen went into the formation of the oxide. Moving to the carbon 1s peak as shown in Fig 4.7.4, it can be seen prior to hafnium deposition that the intensity of the peak is high which signifies the presence of just diamond; whereas after hafnium deposition and annealing, the peak shrinks because of the layer of hafnium and the possible formation of the carbide of hafnium.

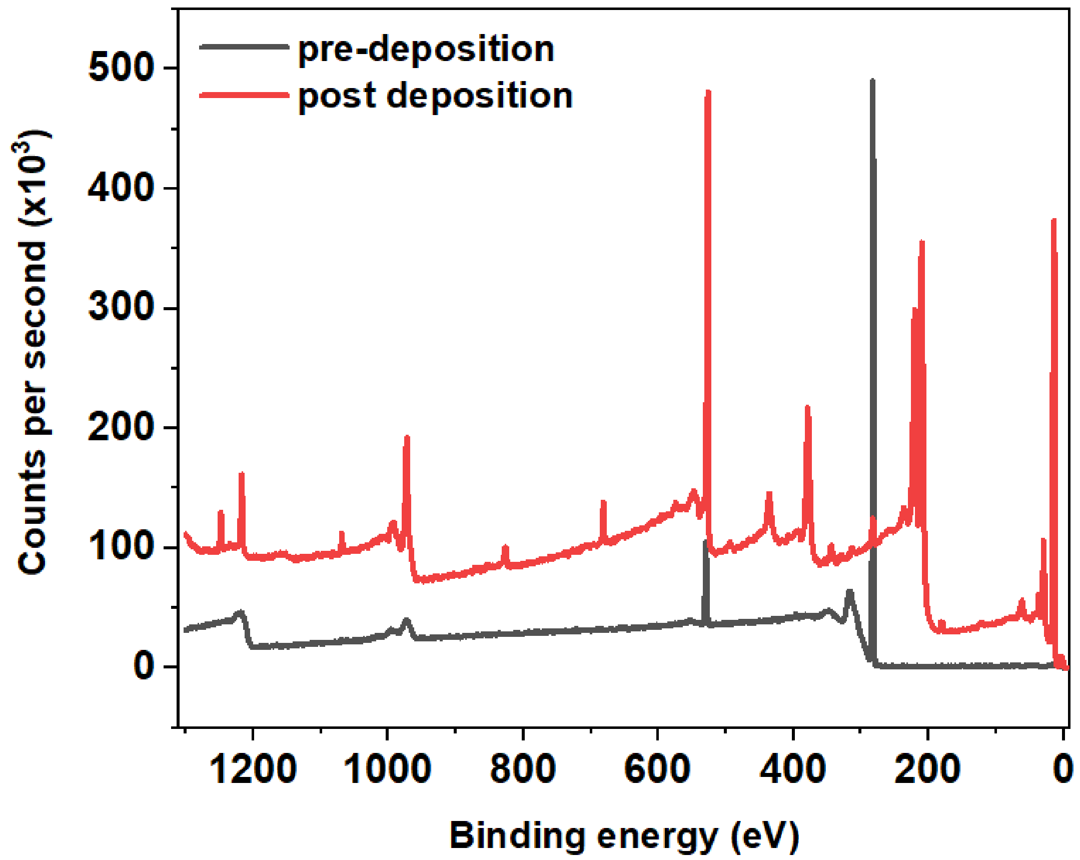

Figure 4.7.1: Wide XPS spectrum before and after deposition showing the presence of hafnium on the substrate surface

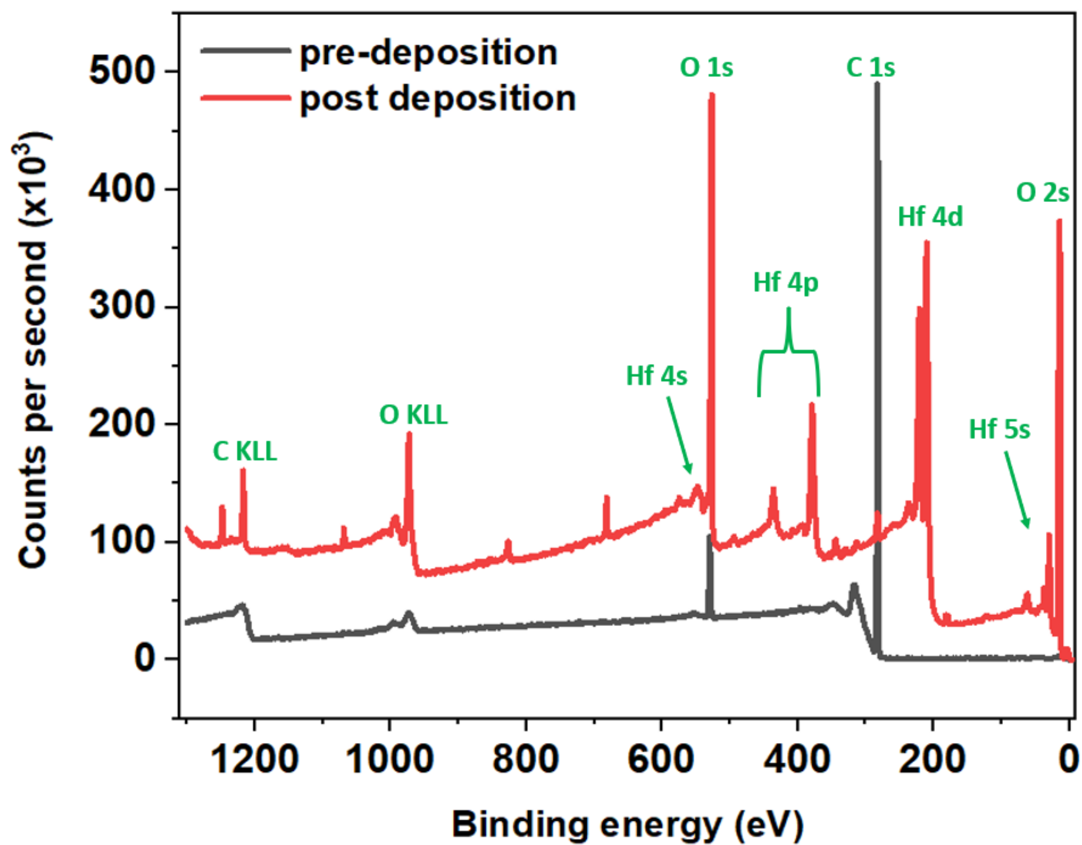

Figure 4.7.2: Wide XPS spectrum before and after deposition with peak labels showing the presence of hafnium on the substrate surface

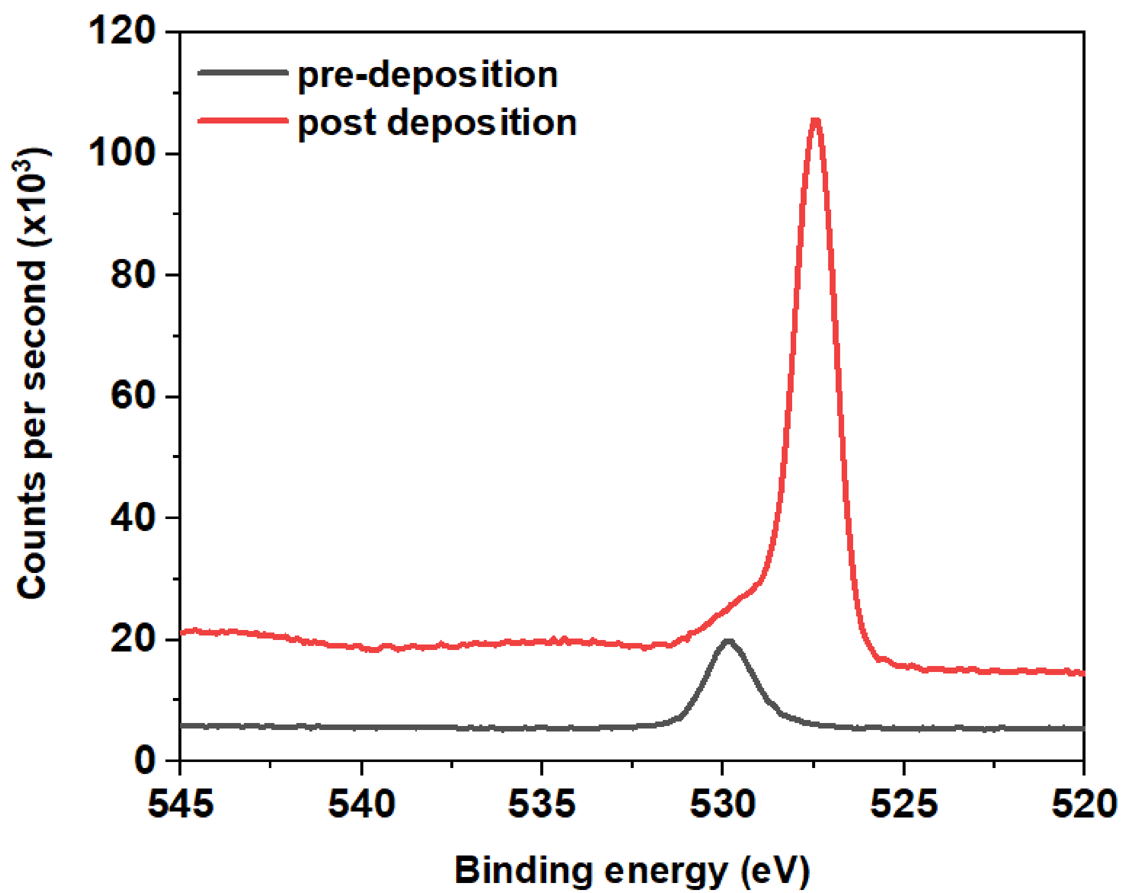

Figure 4.7.3: Oxygen 1s XPS spectrum before and after hafnium deposition where peak shift denotes hafnium oxide formation

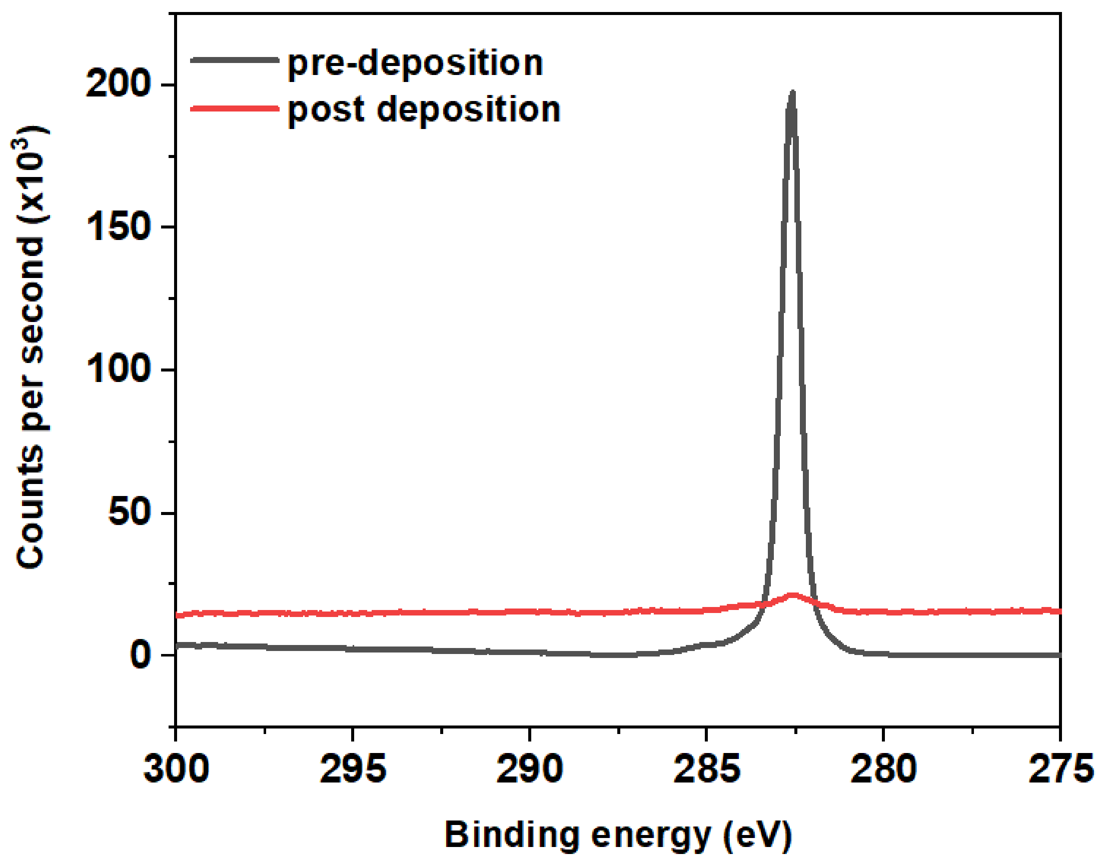

Figure 4.7.4: Carbon 1s XPS spectrum showing the bare diamond surface before deposition and the lowered peak due to hafnium

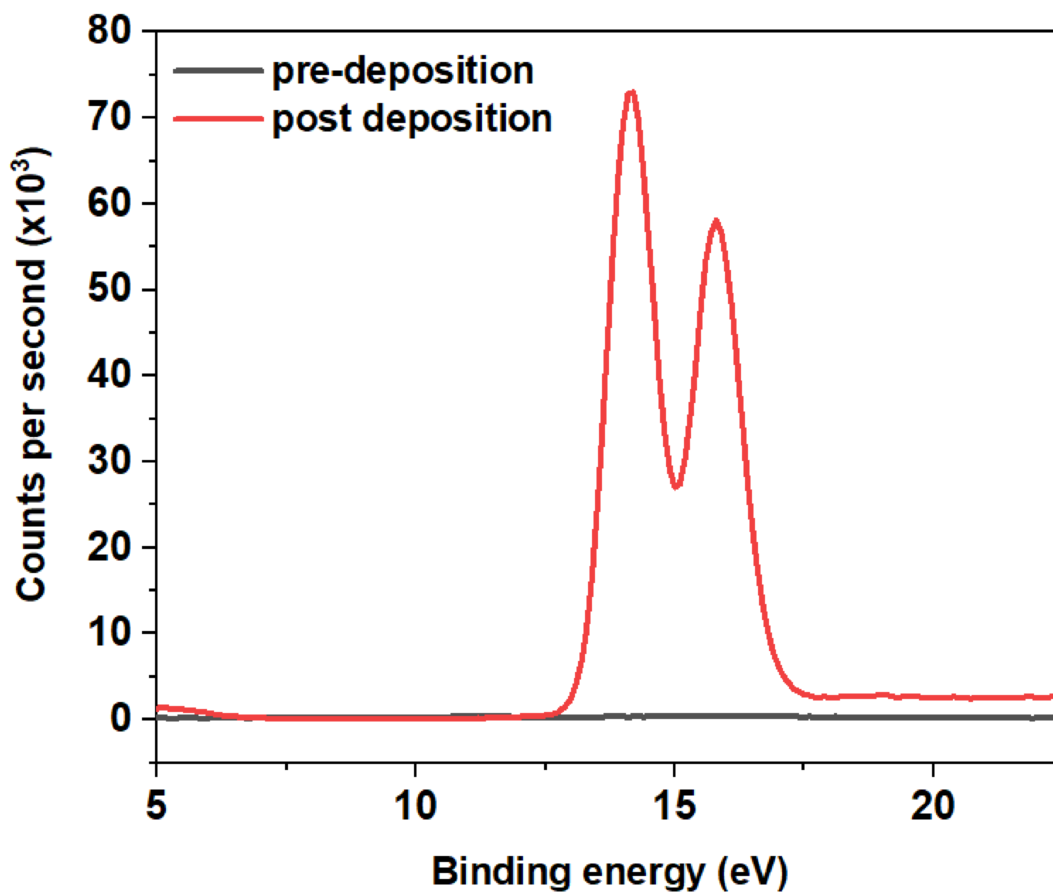

Figure 4.7.5: Hafnium 4f XPS spectrum before and after deposition. Peak shift denotes carbide formation.

4.7.2 SEM Results

Figure 4.7.6 shows an SEM image of nanocarbon which shows that there are some needle-like features resembling bundles within the matrix which have an orientation. High resolution SEM images of the nanocarbon surfaces previously shown the presence of needle-like structures on the order of about 2-5 nm of sp^3 bonded carbon(diamond) scattered and with wide grain boundaries where hopping conduction takes place [33]. The shape of the microneedles largely depends on the shear forces induced during growth and the presence of a nitrogen-rich environment, whereas the grain boundaries have disordered sp^2 bonded graphitic phases generated as a result of flowing methane in the deposition chamber during the growth[32]. The combination of the nitrogen environment leads to the increase in grain sizes and grain boundary widths and the methane causes more graphitic phases to be generated at the grain boundaries. The mixed sp^2/sp^3 bonded phases leads to mid bandgap states which aid in the conduction[34, 35].

SEM images of the rectangular TLM contacts after deposition and liftoff is shown in Fig. 4.7.7 above. The spacing ranges from 2 µm to 40 µm even though the 2 µm spacing was not developed properly during the fabrication process.

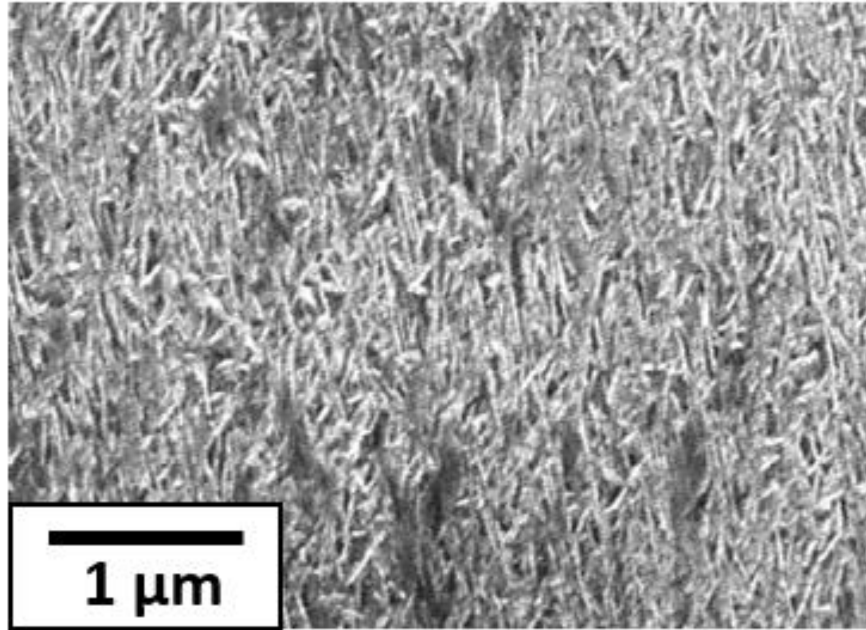

Figure 4.7.6: SEM image of nanocarbon diamond surface

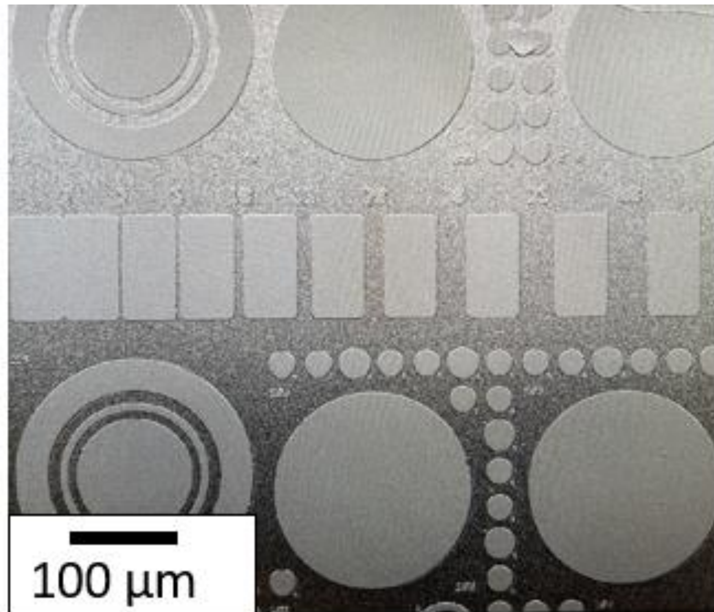

Figure 4.7.7: SEM of TLM contacts after metal deposition and lift off

4.7.3 Hall Effect Measurements

The results from the room temperature Hall effect measurements are tabulated below in Table 4.2. Several readings were taken for consistency. The bulk electron concentration was about 2.40×10^{20} cm^{-3} and a negative sign from the testing denoted a strong n-type conductivity, confirming the presence of abundant nitrogen dopants in the nanoC, which will contribute to the conductivity of the film. Consequently, the electron sheet concentration was 7.22×10^{15} cm^{-2}, sheet resistance was 380 $\Omega\square^{-1}$, the resistivity was 1.21×10^{-2} Ωcm which is similar to previous measurements [33] and finally, a mobility of 2.18 $cm^2V^{-1}s^{-1}$ was measured.

Table 4.2: Room Temperature Hall Effect Measurement Parameters

Parameter	**Average value**
Bulk electron concentration (cm^{-3})	2.40×10^{20}
Sheet electron concentration (cm^{-2})	7.22×10^{15}
Sheet resistance ($\Omega\square^{-1}$)	380
Resistivity (Ωcm)	1.21×10^{-2}
Mobility ($cm^2V^{-1}s^{-1}$)	2.18

4.7.4 Electrical Measurements

Electrical measurement results showed that the hafnium formed a contact with near Ohmic properties, as shown in Fig. 4.7.8 where the amount of current decreased as the spacing increased. Subsequent measurements for similar TLM structures showed similar behavior. The different resistances were extracted for the spacings and a plot of the total resistance vs spacing is shown in Fig. 4.7.9. From this plot, the TLM parameters were calculated from the equations below and the results tabulated in Table 4.3.

Contact resistance

$$R_c = \frac{y\ intercept}{2} \tag{1}$$

Transfer length

$$L_t = \frac{y\ intercept}{2 \times slope} = \frac{x\ intercept}{-2} \tag{2}$$

Sheet resistance

$$R_s = slope\ \times width\ of\ contact \tag{3}$$

Resistivity

$$\rho = R_s \times epilayer\ thickness \tag{4}$$

Specific contact resistance

$$\rho_c = R_c \times L_t \times width\ of\ contact \qquad (5)$$

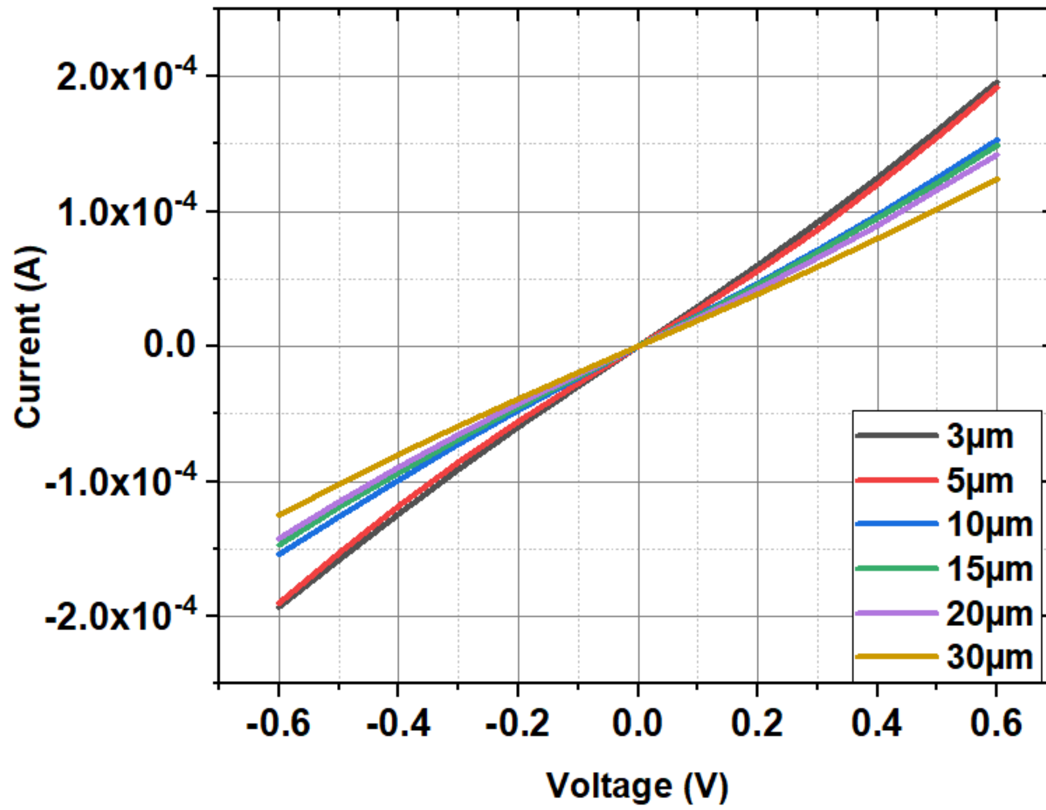

Figure 4.7.8: Plot of current-voltage measurements of TLM contacts over different spacings

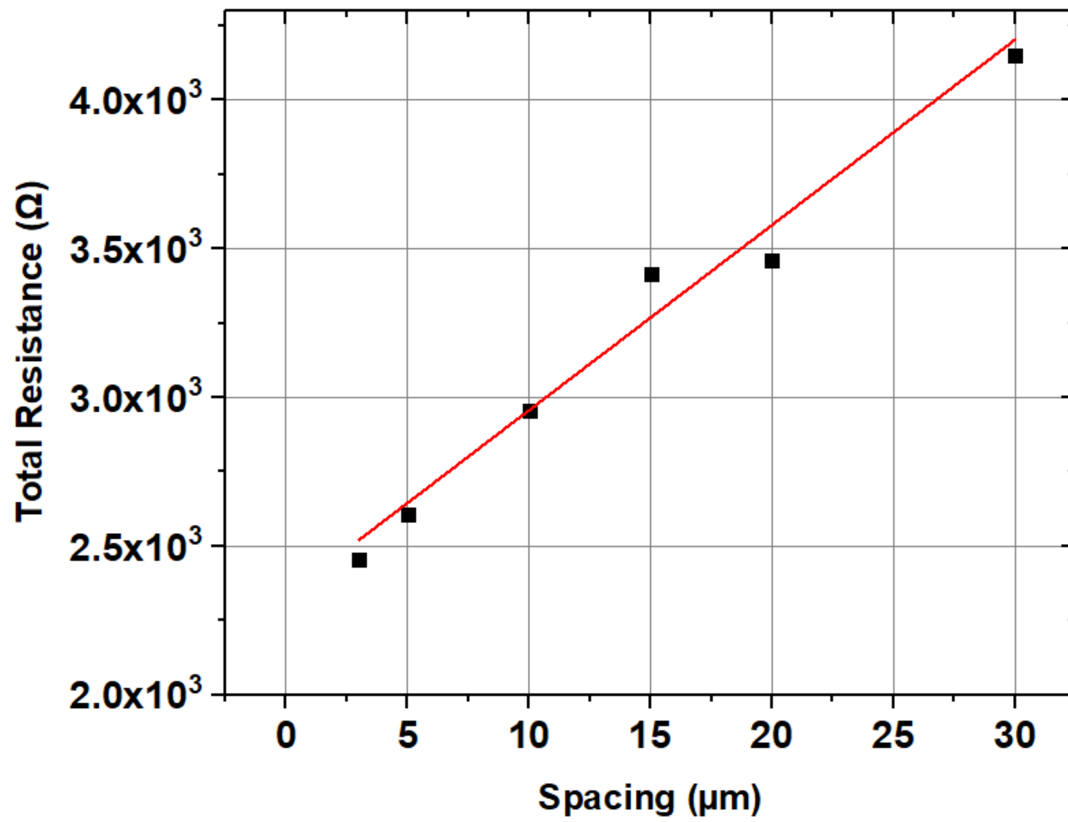

Figure 4.7.9: Plot of total resistance vs spacing

Table 4.3: Table Comparing Extracted Parameters for Ti/Pt/Au and Hf/Pt/Au Contacts on NanoC Diamond

Contact	Transfer Length µm	Contact resistance Ω	Sheet resistance Ω/□	Contact resistivity $\Omega.cm^2$
Ti/Pt/Au	5.7	17.2	305.7	9.92×10^{-5}
Hf/Pt/Au	18.7	1167	6290	2.21×10^{-2}

From Table 4.3 comparing the trilayer contact using Ti and that using Hf, it can be seen that the contact resistance and sheet resistance of the hafnium contact are orders of magnitude greater than the titanium contact, while the contact resistance is the reverse. The large discrepancy between the two experiments begins from the deposition of hafnium where after the sputtering tool is used to deposit hafnium, vacuum is broken, and the sample is transferred to the e-beam evaporator for the deposition of the platinum and gold. The process of breaking the vacuum exposes the sample to air for a few minutes, which leads to the formation of more native oxides of hafnium on the surface, which are hard to remove through annealing alone. The reason for this is due to the high melting temperature of hafnium, making it hard to be evaporated using an e-beam since that will require high energy. For the next experiments however, a sputtering tool that can deposit all three metals will be the best option to reduce the amounts of native hafnium oxide formed. Nevertheless, the this is the first time a tri-layer contact using hafnium on nanocrystalline diamond has been reported and the contact resistivity of 2.21×10^{-2} $\Omega.cm^2$ is a good start and future tests may improve on this.

4.8 Conclusions

A trilayer metal contact was formed using hafnium, platinum, and gold (Hf/Pt/Au) and was deposited on nanocrystalline diamond. Preliminary studies of hafnium on diamond show the possible formation of hafnium carbide after annealing at 800 °C. Hall effect measurements on the nanocrystalline diamond show a strong n-type conducting behavior. Current-voltage (I-V) results show a nearly Ohmic behavior of the contact and transmission line method measurements resulted in a sheet resistance of 6290 Ω/□ and a contact resistivity of 2.21×10^{-2} $\Omega.cm^2$ which is the lowest value attained for hafnium used in a trilayer metal contact on nanocrystalline diamond.

4.9 References

[1] Holloway, P. H. (1979). Gold/chromium metallizations for electronic devices: Manufacturing technology and behaviour. *Gold Bulletin*, *12*(3), 99-106.

[2] Saijo, K., Yagi, M., Shibuki, K., & Takatsu, S. (1990). The improvement of the adhesion strength of diamond films. *Surface and Coatings Technology*, *43*, 30-40.

[3] May, P. W., Regan, E. M., Taylor, A., Uney, J., Dick, A. D., & McGeehan, J. (2012). Spatially controlling neuronal adhesion on CVD diamond. *Diamond and related materials*, *23*, 100-104.

[4] Peng, X. L., & Clyne, T. W. (1997). Formation and adhesion of hot filament CVD diamond films on titanium substrates. *Thin solid films*, *293*(1-2), 261-269.

[5] Buccioni, E., Braca, E., Kenny, J. M., & Terranova, M. L. (1999). Processing–structure–adhesion relationship in CVD diamond films on titanium substrates. *Diamond and related materials*, *8*(1), 17-24.

[6] Biener, M. M., Biener, J., Kucheyev, S. O., Wang, Y. M., El-Dasher, B., Teslich, N. E., … & Wild, C. (2010). Controlled incorporation of mid-to-high Z transition metals in CVD diamond. *Diamond and related materials*, *19*(5-6), 643-647.

[7] Iacovangelo, C. D. (1996). Thermal stability of metallized CVD diamond. *Thin Solid Films*, *286*(1-2), 264-269.

[8] Hwu, H. H., & Chen, J. G. (2005). Surface chemistry of transition metal carbides. *Chemical reviews*, *105*(1), 185-212.

[9] Viñes, F., Sousa, C., Liu, P., Rodriguez, J. A., & Illas, F. (2005). A systematic density functional theory study of the electronic structure of bulk and (001) surface of transition-metals carbides. *The Journal of chemical physics*, *122*(17), 174709.

[10] Tachibana, T., Williams, B. E., & Glass, J. T. (1992). Correlation of the electrical properties of metal contacts on diamond films with the chemical nature of the metal-diamond interface. II. Titanium contacts: A carbide-forming metal. Physical Review B, 45(20), 11975.

[11] Lavrenko, V. A., Glebov, L. A., Pomitkin, A. P., Chuprina, V. G., & Protsenko, T. G. (1975). High-temperature oxidation of titanium carbide in oxygen. Oxidation of Metals, 9(2), 171-179.

[12] Leroy, W. P., Detavernier, C., Van Meirhaeghe, R. L., Kellock, A. J., & Lavoie, C. (2006). Solid-state formation of titanium carbide and molybdenum carbide as contacts for carbon-containing semiconductors. Journal of applied physics, 99(6), 063704.

[13] https://www.acs.org/education/whatischemistry/periodictable.html

[14] Cappelli, E., Bellucci, A., Orlando, S., Trucchi, D. M., Mezzi, A., & Valentini, V. (2013). PLD deposition of tungsten carbide contact for diamond photodiodes. Influence of process conditions on electronic and chemical aspects. *Applied surface science*, *278*, 111-116.

[15] Vardi, A., Tordjman, M., Kalish, R., & del Alamo, J. A. (2020). Refractory W ohmic contacts to H-terminated diamond. *IEEE Transactions on Electron Devices*, *67*(9), 3516-3521.

[16] Teraji, T., Garino, Y., Koide, Y., & Ito, T. (2009). Low-leakage p-type diamond Schottky diodes prepared using vacuum ultraviolet light/ozone treatment.

[17] Xing, K., Tsai, A., Rubanov, S., Creedon, D. L., Yianni, S. A., Zhang, L., … & Qi, D. C. (2020). Palladium forms Ohmic contact on hydrogen-terminated diamond down to 4 K. *Applied Physics Letters*, *116*(11), 111601.

[18] Fang, F. A. N. G., Hewett, C. A., Fernandes, M. G., & Lau, S. S. (1989). Ohmic contacts formed by ion mixing in the Si-diamond system. *IEEE transactions on electron devices*, *36*(9), 1783-1786.

[19] Drozdov, M. N., Arkhipova, E. A., Drozdov, Y. N., Kraev, S. A., Shashkin, V. I., Parafin, A. E. E., … & Bogdanov, S. A. (2020). The use of pulsed laser annealing to form ohmic Mo/Ti contacts to diamond. *Technical Physics Letters*, *46*, 551-555.

[20] Das, K., Venkatesan, V., Miyata, K., Dreifus, D. L., & Glass, J. T. (1992). A review of the electrical characteristics of metal contacts on diamond. *Thin Solid Films*, *212*(1-2), 19-24.

[21] Venkatesan, V., & Das, K. (1992). Ohmic contacts on diamond by B ion implantation and Ti-Au metallization. *IEEE electron device letters*, *13*(2), 126-128.

[22] Jingu, Y., Hirama, K., & Kawarada, H. (2010). Ultrashallow TiC source/drain contacts in diamond MOSFETs formed by hydrogenation-last approach. *IEEE transactions on electron devices*, *57*(5), 966-972.

[23] Mphahlele, M. R., Olubambi, P. A., & Olevsky, E. A. (2023). Advances in Sintering of Titanium Aluminide: A Review. *JOM*, 1-20.

[24] Imura, M., Hayakawa, R., Ohsato, H., Watanabe, E., Tsuya, D., Nagata, T., … & Amano, H. (2012). Development of AlN/diamond heterojunction field effect transistors. *Diamond and related materials*, *24*, 206-209.

[25] Ottaviani, G., Tu, K. N., & Mayer, J. W. (1980). Interfacial reaction and Schottky barrier in metal-silicon systems. *Physical Review Letters*, *44*(4), 284.

[26] Andrews, J. M., & Phillips, J. C. (1975). Chemical bonding and structure of metal-semiconductor interfaces. *Physical Review Letters*, *35*(1), 56.

[27] Niessen, A. K., & De Boer, F. R. (1981). The enthalpy of formation of solid borides, carbides, nitrides, silicides and phosphides of transition and noble metals. *Journal of the Less common Metals*, *82*, 75-80.

[28] Schemel, J. H. (1977). *ASTM manual on zirconium and hafnium* (No. 639). Astm International.

[29] H. Nielsen, R., H. Schlewitz, J., Nielsen, H., & Updated by Staff. (2000). Zirconium and zirconium compounds. *Kirk-Othmer Encyclopedia of Chemical Technology*, 1-46.

[30] Hans, K., Latha, S., Bera, P., & Barshilia, H. C. (2018). Hafnium carbide based solar absorber coatings with high spectral selectivity. *Solar Energy Materials and Solar Cells*, *185*, 1-7.

[31] F.A. Koeck, and R.J. Nemanich, "Contact structures for n-type diamond." U.S. Patent 11,380,763.

[32] Koeck, F. A., Benipal, M., & Nemanich, R. J. (2020). Electrical contact considerations for diamond electron emission diodes. *Diamond and Related Materials*, *101*, 107607.

[33] Amonoo E., Jha V., Thornton T, Koeck F. A, Nemanich R. J., and Alford T. L.(2023) Ohmic Contacts to Nitrogen-Doped Nanocarbon Layers on Diamond (100) Surfaces. *Diamond and Related Materials, 135, 109832.*

[34] Birrell, J., Carlisle, J. A., Auciello, O., Gruen, D. M., & Gibson, J. M. (2002). Morphology and electronic structure in nitrogen-doped ultrananocrystalline diamond. *Applied Physics Letters*, *81*(12), 2235-2237.

[35] Gerbi, J. E., Auciello, O., Birrell, J., Gruen, D. M., Alphenaar, B. W., & Carlisle, J. A. (2003). Electrical contacts to ultrananocrystalline diamond. *Applied Physics Letters*, *83*(10), 2001-2003.

CHAPTER 5

CONTACT FORMATION ON SELECTIVELY GROWN NANOCARBON ON DIAMOND

5.1 Introduction and Background

Selective area growth(SAG) or area-selective deposition(ASD) is the process of growing or depositing a material in a specific surface of a part of a substrate in the presence of another surface[1-3]. This growth process has found a wide range of applications in integrated circuits and semiconductor structures where it is used to deposit materials such as metals, semiconductors, and insulators by the use of two main pathways: Chemical vapor deposition(CVD) and atomic layer deposition(ALD) even though CVD has been recently more popular[2]. Parson *et al.* provide a comprehensive review of the ALD and CVD processes involved in area selective deposition of thin films and provides insights into the various mechanisms that take place, highlights some limitations of each method, and suggests improvements to make them better. Akiki *et al*. for instance have shown the selective growth of microcrystalline silicon on SiO_xN_y surfaces as opposed to Al and AlO_x surfaces due to the presence of fluorine bonds on the Al areas[1]. Ducati et al. have also described a temperature dependent selective growth of carbon nanotubes where the size and shape of the growing piece was founds to be directly linked to the process temperature[5]. Further he use of surface modification to control selectivity has been studied by Hampden-Smith *et al.* in the deposition of metal-based compounds using CVD[6]. In the field of semiconductors, Mokari *et al.* have successfully grown conducting gold tips on CdSe quantum rods which can serve as contact points for electrical devices[7].

Alam *et al*., Chang *et al*., and Liu *et al.* simulated and mapped many factors and parameters involved in selective grown samples used for semiconductor applications[8-10]. Furthermore, the formation mechanisms of preferentially growing $Al_xGa_{1-x}N$ and GaN on GaN/sapphire substrates using SiO_2 masks have been described by Kato *et al.* and the growth rate of the features were found to decrease with increasing growth time leading to changes in the morphology[11].

The use of nanocarbons on the other hand, have been found to be an effective way reducing contact resistivity on diamond films[12-17] with contact resistivities on the order of 10^{-5} $\Omega.cm^2$[18]. However, previous experiments incorporating nanoC have deposited it on the entire surface instead of isolating the material to the areas for contacts. The first method to address this issue involved a reactive-ion etching process after metal deposition to etch as much nanocarbon uncovered by the metals as shown in Fig 5.1.1 but this method made it hard to resolve the point where there was no nanocarbon left on the surface suing electrical probing alone. The second method was to use selective area growth to isolate the nanoC growth in trenches created for the metal contacts using SiO_2 as a mask as shown in Fig 5.1.2. This means that the growth will be selective to the exposed diamond surface as opposed to the SiO_2 surface. With this knowledge, TLM contacts are fabricated on a diamond/SiO_2 surface with lithography and trenches are etched out from the SiO_2 to the diamond surface and nanoC is grown in the trenches for contact formation. Optical microscopy, Raman spectroscopy, X-ray topography(XRT), Electron backscattering diffraction(EBSD), profilometry, Focused ion beam (FIB)-SEM are used to characterize the starting material and to investigate the success of the selective growth process.

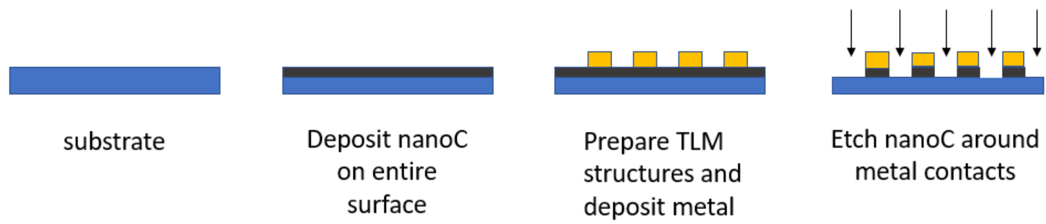

Figure 5.1.1: Etching procedure for first method of isolating nanoC underneath metal contacts

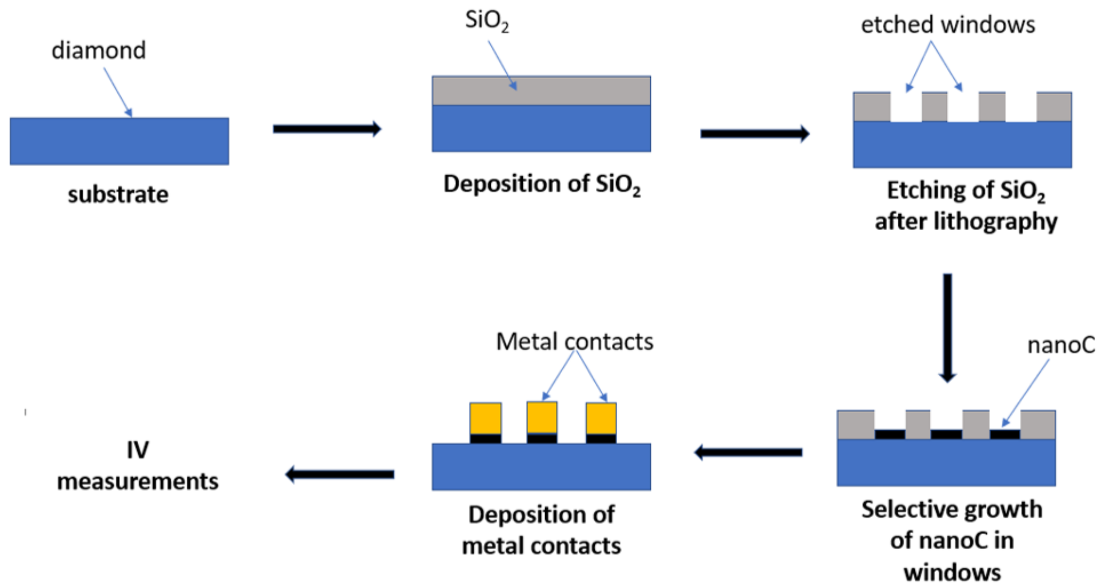

Figure 5.1.2: Proposed process flow for selective growth method of isolating nanoC

5.2 Experimental Tools

Tools used for the fabrication, characterization and testing of the samples include:

- PECVD system
- Dektak profilometer
- Spin coater
- Photolithography Aligner
- TLM mask
- Barrel asher
- X-ray topography system
- Optical pyrometer
- Reaction Ion Etcher
- Scanning electron Microscope
- Hot plate
- X-ray diffractometer
- Optical microscope
- Raman spectrometer

5.3 Experimental Process

Three intrinsic (100) diamond substrates were obtained from Element 6 and cleaned using a 3:1 acid piranha solution ($H_2SO_4 + H_2O_2$) for 20 mins, followed by a 20 mins HF dip, then a clean in 80 °C base piranha solution ($NH_4OH + H_2O_2$) for 20 mins and finally with a boiling mixture of HNO3 + H_2SO_4 for 20 mins at 150 °C. The samples were investigated using X-ray topography to map possible defects on the surface using a Rigaku XRT-100 system in transmission mode. The x-ray source was Mo $K\alpha_1$, a voltage of 50kV, a current of 40mA and a scanning speed was 2mm/sec. After this the grain orientation was investigated by the use of an Aztec EBSD system loaded and attached to a Zeiss Auriga SEM system to confirm the orientation of the sample. The beam energy was 20 keV, the working distance was ~10 mm and the step size was 5 µm. From these results, a suitable sample was selected and loaded into an Oxford PEVCD machine and about ~400 nm of SiO_2 was deposited on the surface at 350 °C and a mid-pressure of 1 Torr. The thickness was verified with a Dektak profilometer.

The photoresist AZ3312 was spin-coated on the surface of the sample and was exposed for 6 seconds in an OAI 808 aligner with a mask containing TLM pad structures. MIF 400 developer was used to develop the TLM structures. The resulting structure was baked at 100 °C for about 30 seconds and using the photoresist as a protective mask, the silicon dioxide was etched in the exposed regions in a PlasmaTherm RIE 790 system with a combination of SF_6, CHF_3, CF_4, O_2, and Ar gases. The etch rate was about 60 nm/min and after about 7 mins, the profilometer was used to confirm the depth of the trenches. The rest of the photoresist was then etched using a Tegal barrel asher and the sample was sent out

for selective area growth. Before the plasma enhanced ASTeX CVD reactor chamber grew, the sample was cleaned in a 3:1:1 mixture of $H_2SO_4/H_2O_2/H_2O$ at 220 °C for 15 minutes followed by a DI water rinse, then dried in nitrogen to remove any residual contamination that will interrupt the selective process. The sample was then exposed to hydrogen plasma for 1min at <700 °C. About 50 nm of nanoC was deposited into the trenches after about 5 mins using 5 sccm of H_2, 20 sccm of CH_4, 10 sccm of Ar, 100 sccm of N_2, a heater current of 73.5 A, a microwave power of 900W, at a pressure of 20 Torr and a temperature between ~800-900 °C.

After deposition, Raman spectrometry was performed on the samples to investigate the presence of nanoC, after which FIB-SEM and profilometry was used to estimate the thickness of the grown film. Further, a Keyence VHX 7000 optical microscope was used to perform elemental analysis on both the area of interest and the SiO_2 with its laser-induced breakdown spectrometry(LIBS) feature [19] and a probe diameter of 12 µm. Subsequently, the sample was etched in a 10:1 dilute mixture of H_2O/HF to etch the remaining SiO_2 and the surfaces were investigated with profilometry.

5.4 Results and Discussion

5.4.1 XRT Results

From Fig. 5.4.1, it can be seen that there is the presence of large defects resembling twinning in the middle of samples 1 and 2 as compared to sample 3. These defects are as a result of the growth process where there can be a misalignment of the diamond or a curve in the lattice. Sample 3 showed less misalignment and on the surface and fewer defects.

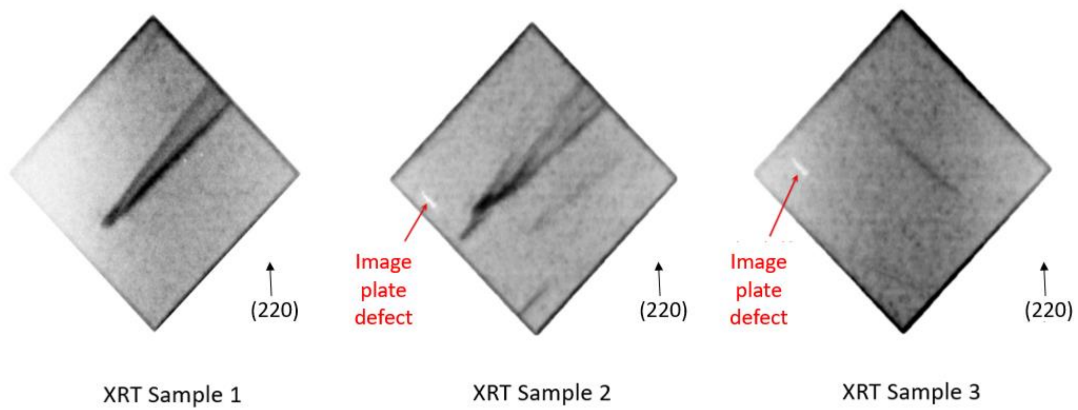

Figure 5.4.1: XRT images of three diamond samples showing defect analysis

5.4.2: EBSD and SEM Results

Due to large defects from Fig 5.4.1, the surface of the diamond samples was further investigated. The different results from the EBDS analysis are shown from Fig. 5.4.2 to 5.4.5. Fig 5.4.2 shows the mapping of the parts of the surface where diamond is detected

with a hit rate of about 50%, Fig 5.4.3 shows the Kikuchi pattern of the diamond and Fig 5.4.4 quantifies the orientation of the substrate. It can be seen that the sample is mostly (100) oriented, which was expected. SEM results showed a fairly smooth and clean surface as shown in Fig 5.4.5.

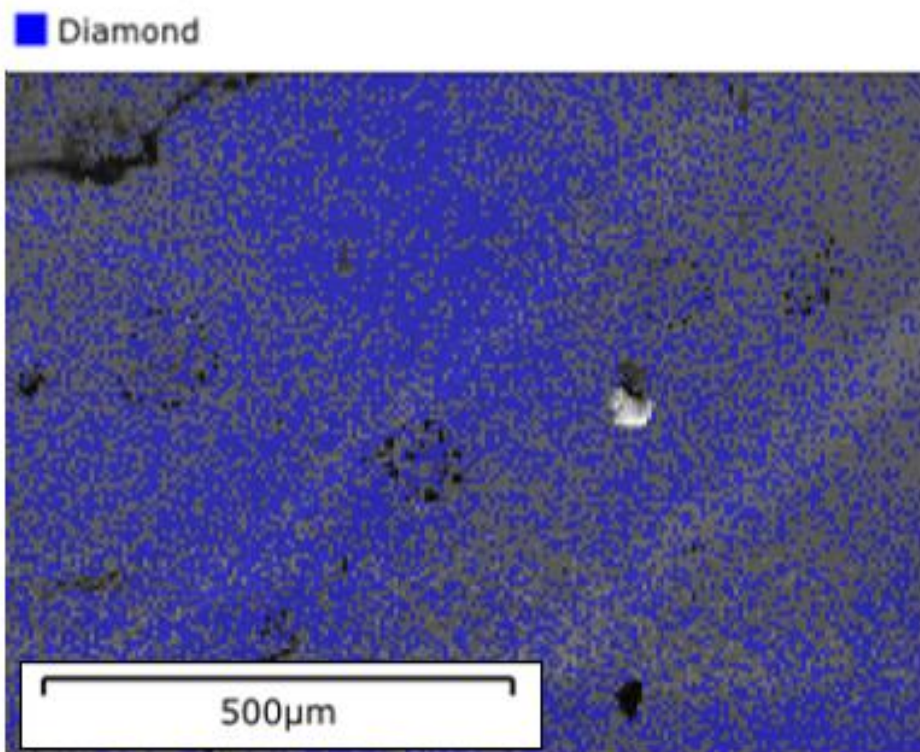

Figure 5.4.2: Site map of phases showing the presence of diamond on the sample

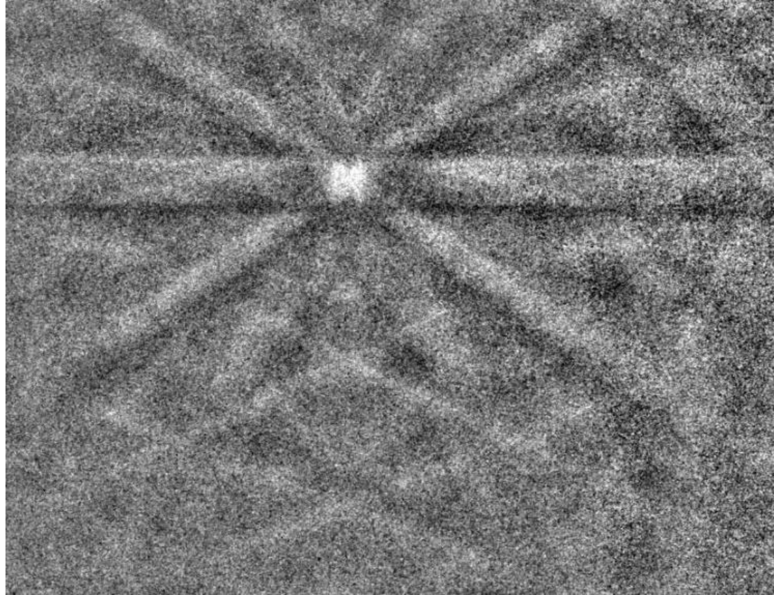

Figure 5.4.3: Kikuchi diffraction pattern of diamond

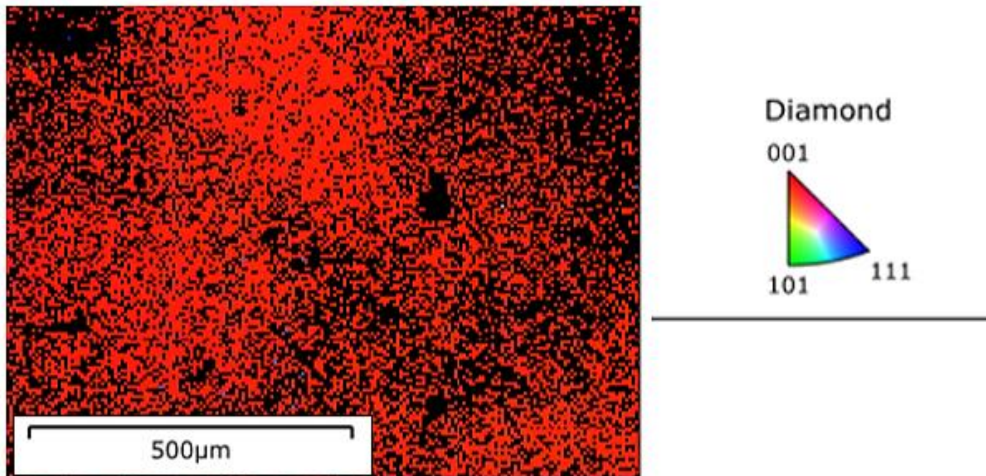

Figure 5.4.3: Site map of detected orientations on diamond surface

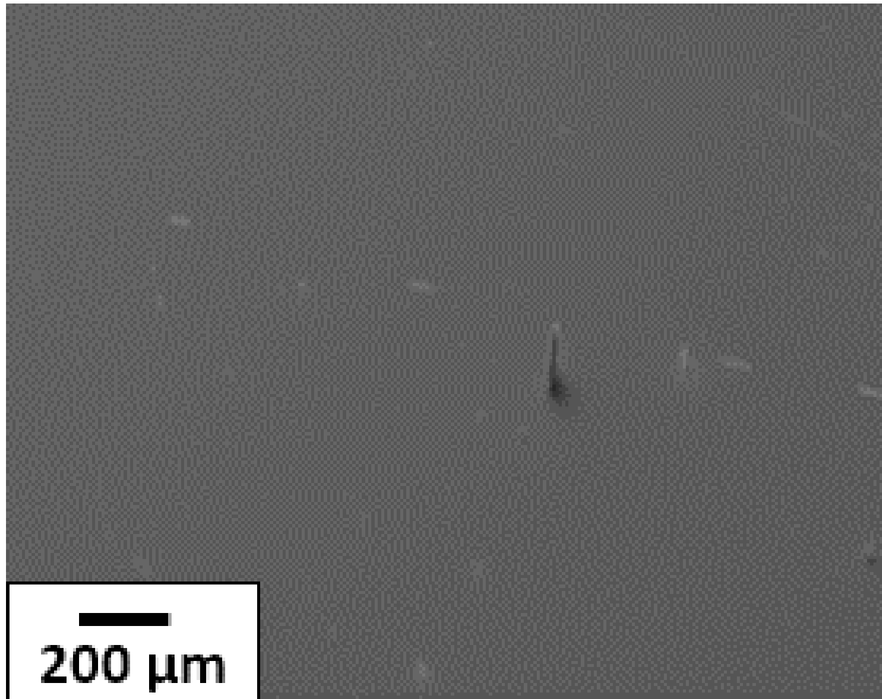

Figure 5.4.5: SEM of diamond surface

5.4.3 SiO_2 Deposition and Etching Process

The profile after silicon dioxide deposition is shown in Fig 5.4.6 below showing a average thickness of about 400 nm.

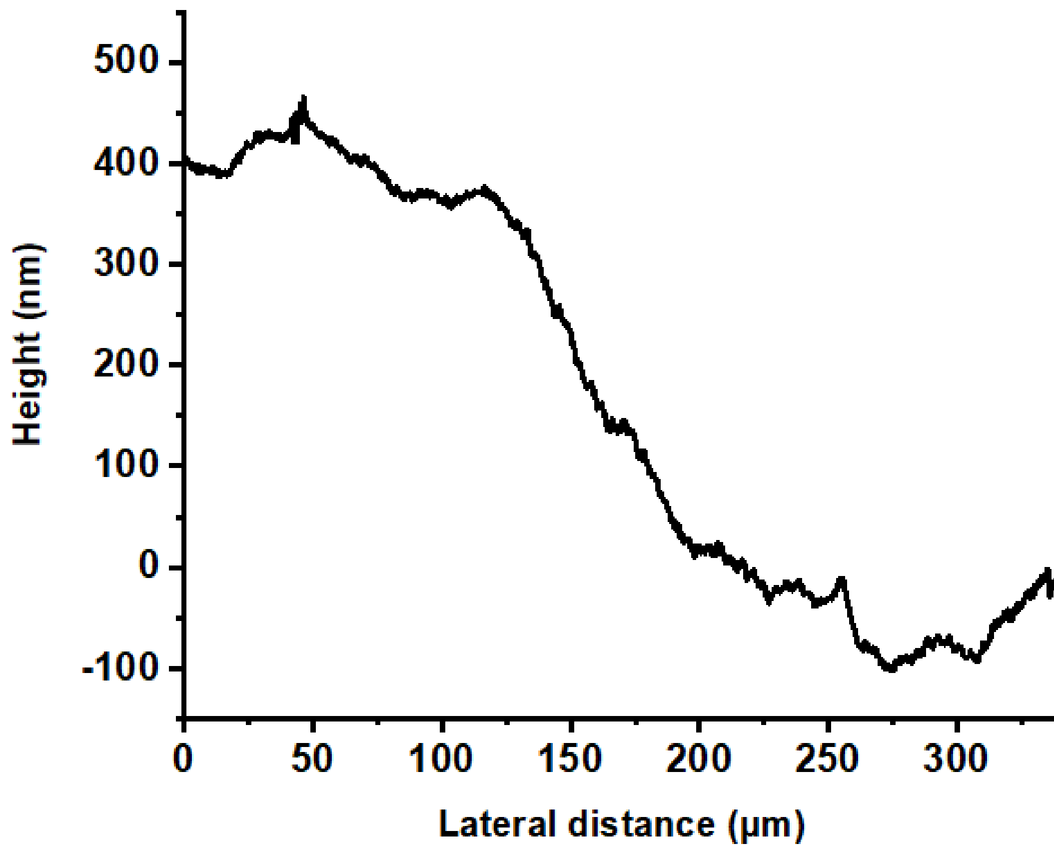

Figure 5.4.6: Profile of SiO_2 deposition in PECVD chamber showing 400 nm of deposited material for hard masking

Fig. 5.4.7 shows the microscopic transition before and after etching the silicon dioxide in the TLM exposed areas. It can be seen that prior to etching, the photoresist covers the entire surface of the diamond, and the opened areas are the surfaces of the SiO_2. After etching for about 7 minutes, there is a minimal amount of photoresist on the surface while the trenches are up to the diamond surface. The profile plot in Fig. 5.4.8 shows the thickness of the photoresist to be about 800 nm and in Fig 5.4.9, the comparison of the heights prior to and

after etching are outlined. After 7 minutes, about 400nm of the photoresist was etched while all of the SiO_2 in the TLM trenches has been removed.

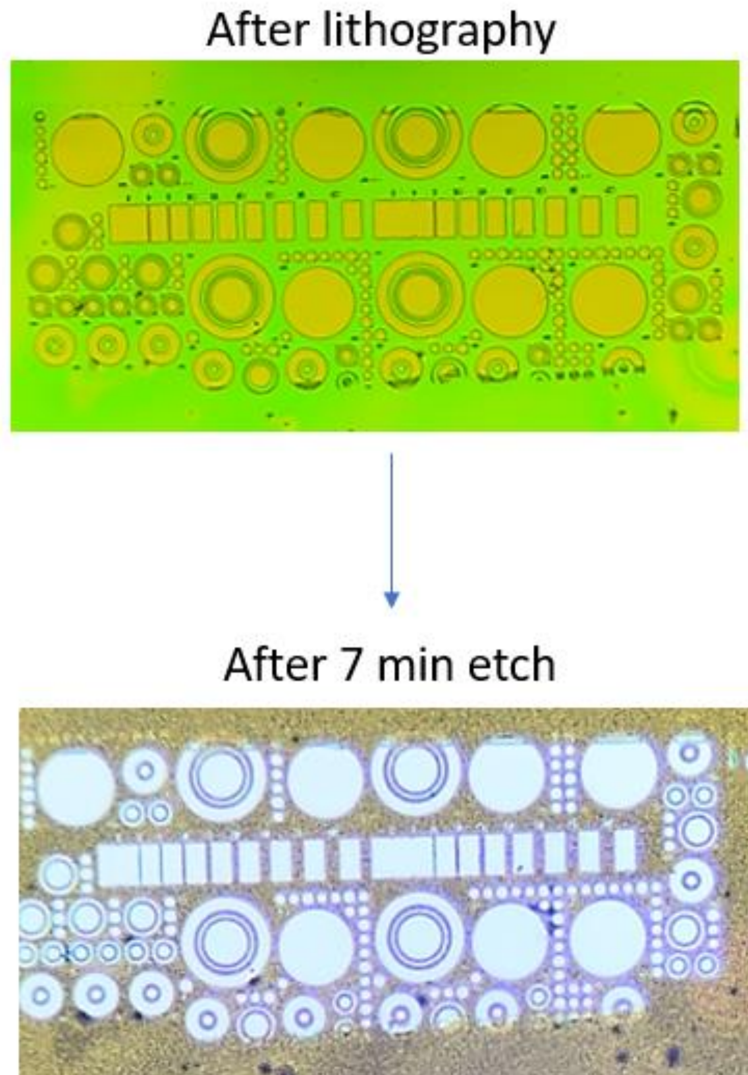

Figure 5.4.7: Microscopy of sample after lithography and after SiO_2 etching

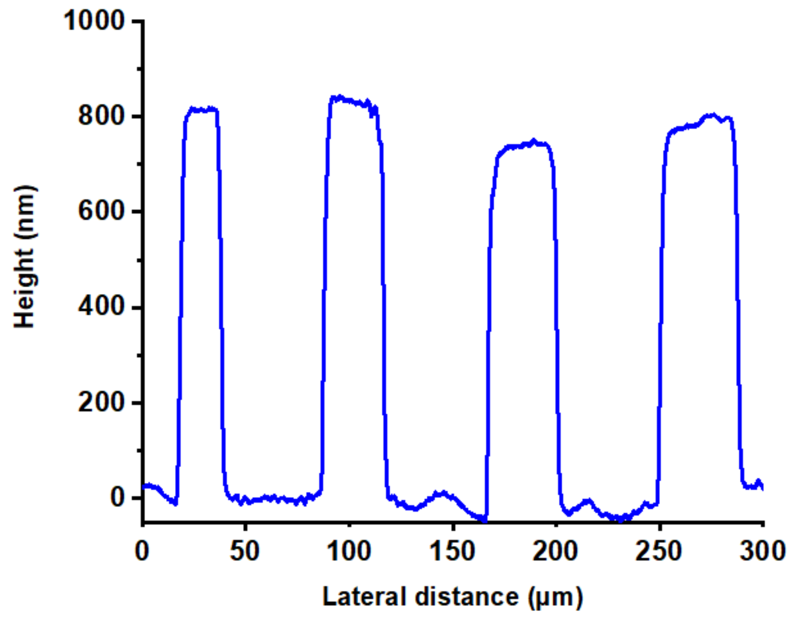

Fig 5.4.8: Profile of photoresist height after lithography

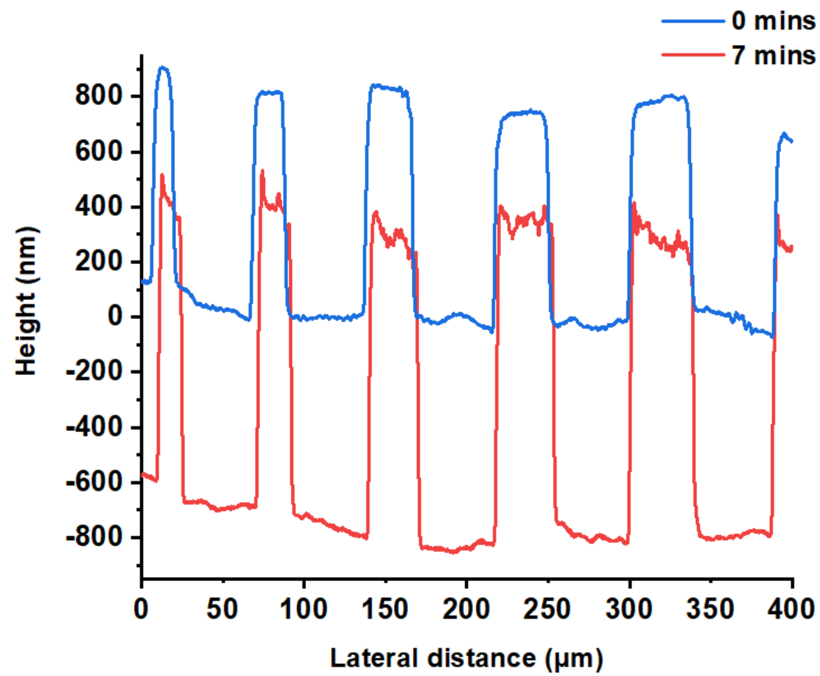

Figure 5.4.9: Profile comparison before and after etching of SiO_2

5.4.4 Selective Growth Results

The microscopic images in Fig. 5.4.10 and Fig 5.4.11 shows the as-received sample and after cleaning in the boiling acid solution, respectively. The dark areas prior to cleaning represent the excess baked photoresist that sits underneath the sample and after cleaning, it is wiped away and the sample is more transparent as shown in Fig 5.4.11.

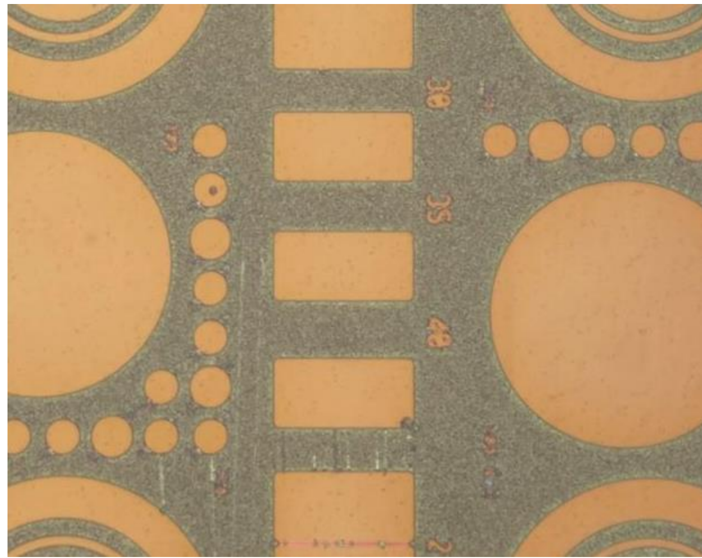

Figure 5.4.10: Optical microscopy of as-received diamond surface

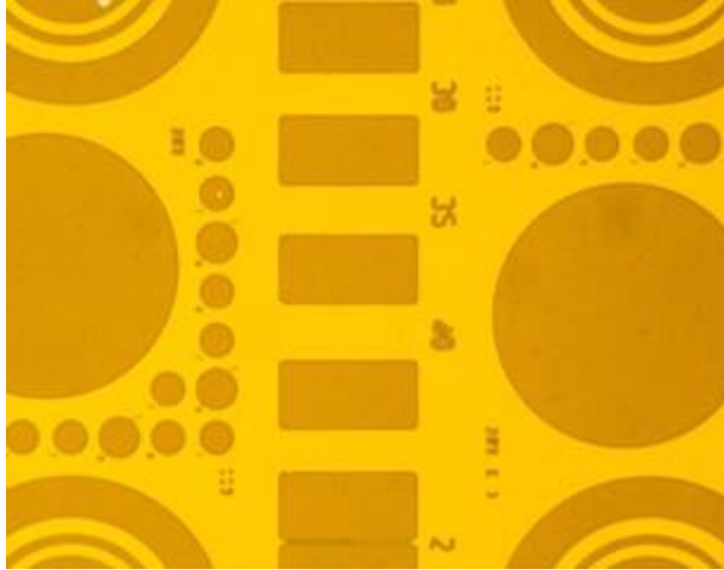

Figure 5.4.11: Optical micrograph of cleaned surface prior to growth

After the nanoC deposition process, it can be seen that the trenches look darker in Fig 5.4.12 as compared to Fig 5.4.11. This is the first indication that something has been deposited, but this result was not conclusive and further testing was required to prove the presence of the deposited material.

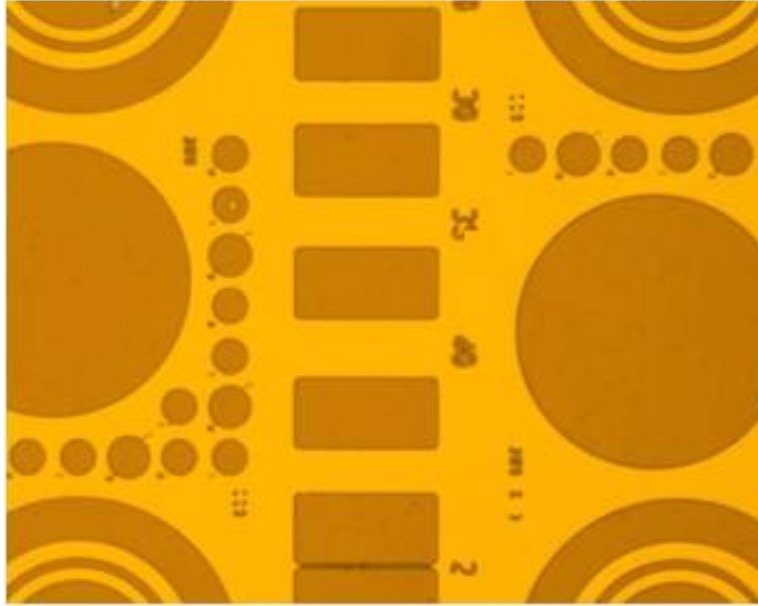

Figure 5.4.12: Optical micrograph after selective growth of nanoC

5.4.5 Raman Spectroscopy

The results from Raman spectroscopy at both the growth area and the SiO_2 region only showed the diamond peak at ~1332 cm^{-1} (Fig 5.4.13) which could be due to the film being too thin (~50 nm) and being overwhelmed by the diamond signal underneath. Therefore, other methods were further explored to confirm the presence of the nanoC.

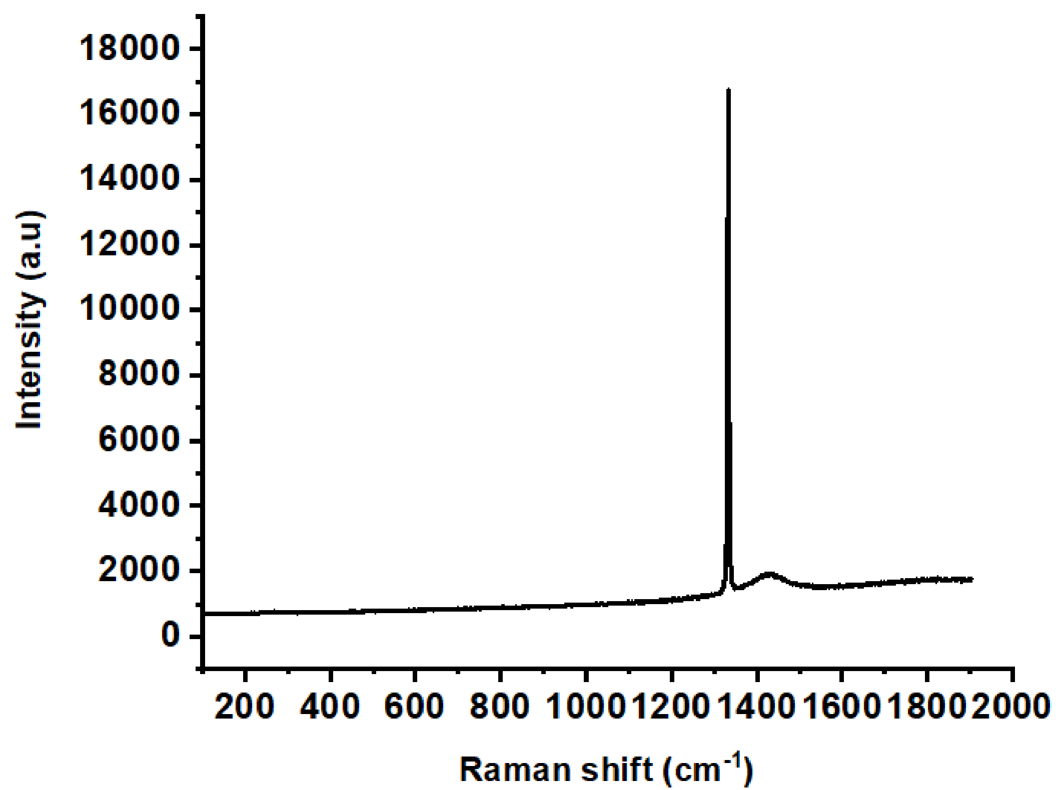

Figure 5.4.13: Raman spectroscopy of sample surface

5.4.6 Elemental Analysis (LIBS)

Results from the elemental analysis show a strong presence of about 16.6% silicon and 83.4% of oxygen in the areas outside the growth region and about 99.1% of carbon in the growth area as shown in Fig 5.4.14 and Fig. 5.4.16. This presence of carbon in the area of interest suggested evidence for some carbon-based material in the TLM pattern trenches but since the material underneath is also a form of carbon(diamond), further testing needed to be carried out.

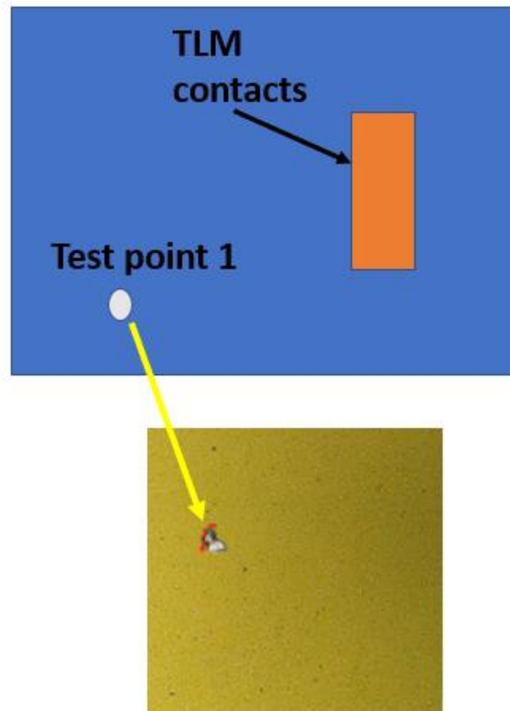

Detected	%
O	83.4
Si	16.6

Figure 5.4.14: Elemental analysis results surface outside growth region

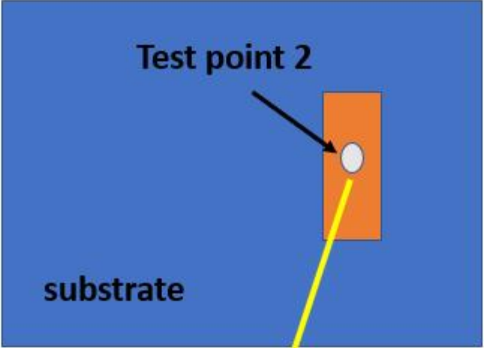

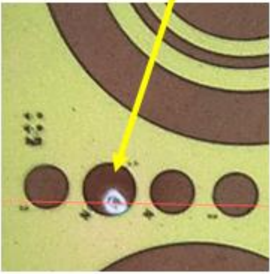

Detected	%
C	99.1
Si	0.1

Figure 5.4.15: Elemental analysis results of growth surface

5.4.7 FIB-SEM Results

The schematic diagram in Fig 5.4.16 outlines the processes carried out on the sample up to the FIB-SEM point with the respective predicted profiles to guide on what to expect from the experiment. The SEM of the experiment shown in Fig 5.4.17 shows the Pt protective layer and the cut a few microns away from it instead of right next to it, proving that the FIB process was imperfect, and the beam drifted a bit from the target area. The color differences in the image also conveys a difference in the heights to further prove that some amount of material has been removed from surface of the area of interest.

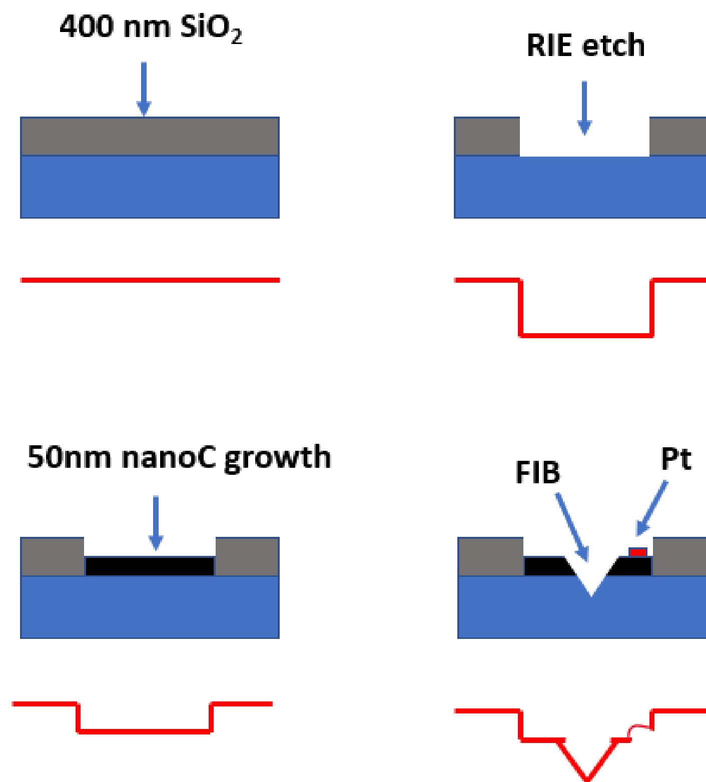

Figure 5.4.16: Schematic diagram of expected FIB profile

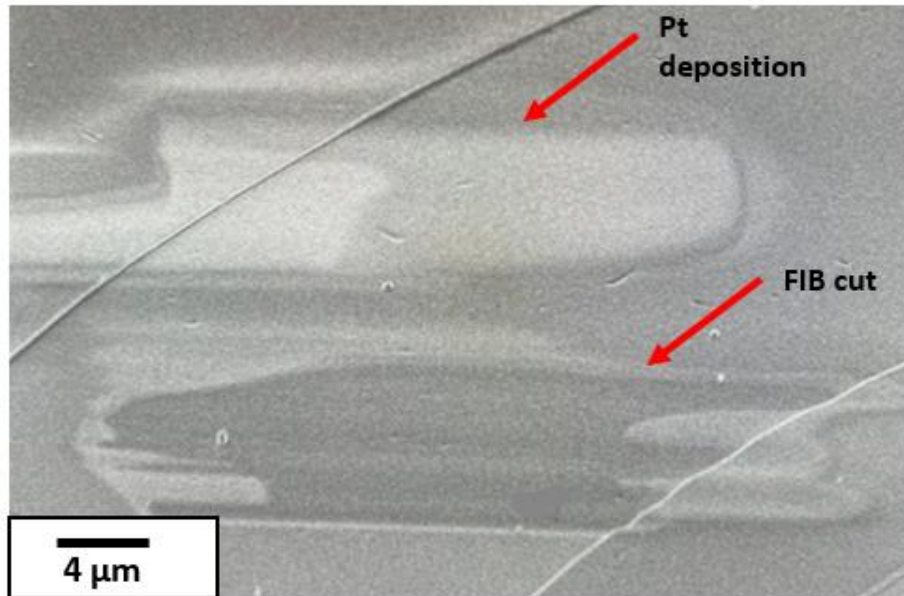

Figure 5.4.17: FIB-SEM of surface tilted to 70°

Additionally, the images in Fig 5.4.18 show the location of the FIB experiments on the sample and the profile area along the dotted line. The profile starts from an area having SiO_2, cuts across the ion beam cut then over the Pt deposit. The result from the profilometry is shown in Fig 5.4.19. From this it can be seen that the profile matches up with what is expected from the schematic(Fig 5.4.16) which is a good indication of a successful beam cut into the diamond. Section 1 depicts the area of deposited silicon dioxide which measures about 350 nm in height even though the originally deposited amount was about 400 nm(Fig 5.4.6). This meant that there was the presence of ~50 nm of another material in the trench, further proving the success of the selective growth of nanoC, which is shown in Section 2. Moving on, Section 3 along the profile displays a cut through the nanocarbon and diamond surface and the 50 nm heights on both sides of the cut reflect that. Section 4 illustrates the platinum deposited before the ion beam cut. Even though the Raman

spectrometry failed to yield results on the selective growth area, the combination of the analysis of the ion beam cut, the elemental analysis, and microscopic color changes provided a strong corroboration for the presence of nanoC growth on the sample.

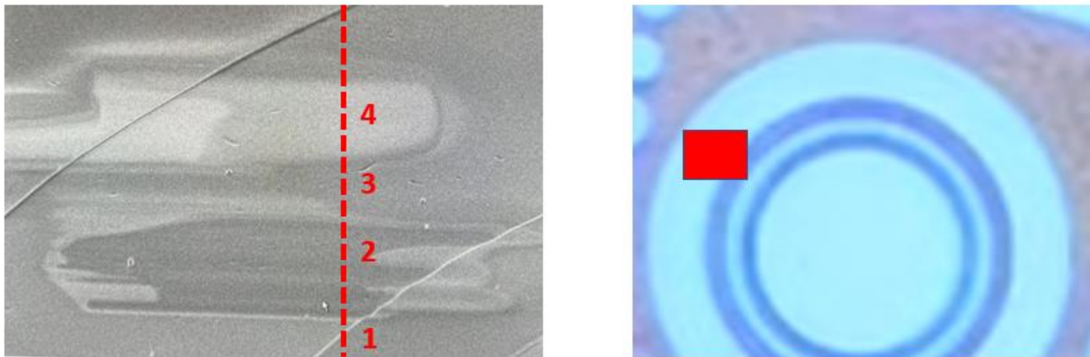

Figure 5.4.18: Location of profile measurements

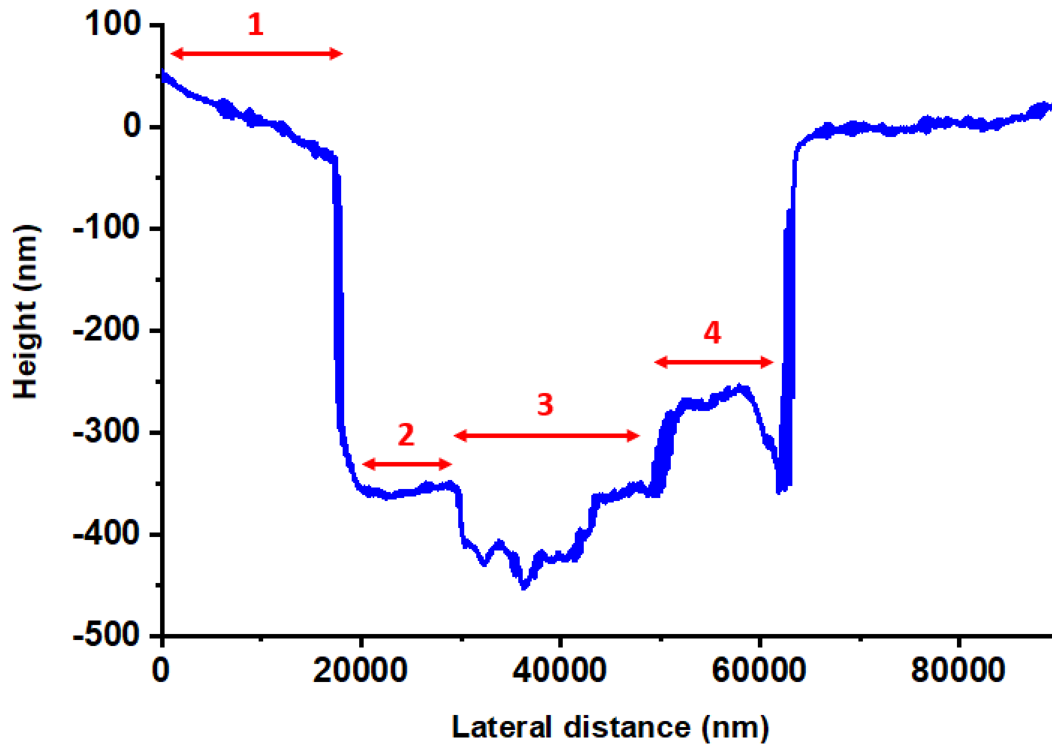

Figure 5.4.19: Profile of FIB area showing different regions

5.4.8 HF Dip Studies

The evolution of the surface of the sample after subsequent etching in Hf is outlined in Fig. 5.4.20 and the microscopic images after each step are shown in Figs 5.4.21 to 5.4.24. Before deposition, about ~350 nm of oxide was outside the trenches to be removed. After about 9 mins the amount of oxide reduced to about 250 nm, and after 15 mins of dipping in HF, there was about 50 nm of oxide left. A subsequent dip (25 mins) brought the amount of oxide left on the same level as the deposited nanoC. From the images, after the last etch(Fig 5.4.24), it was difficult to see the contacts to measure so there was no successive etching. The nanocarbon is thought to have delaminated during the acid dip process which

raised a concern about the possible adhesion problems of the grown film as a result of the thickness. Therefore, further study is required and a thicker nanoC film is recommended for future testing.

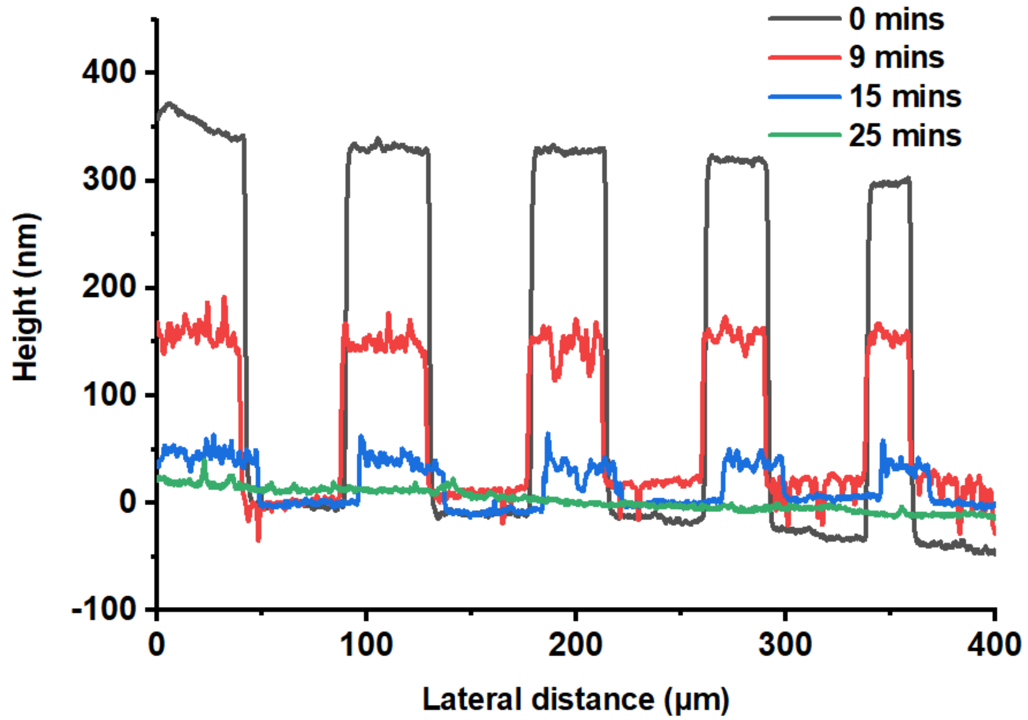

Figure 5.4.20: Plot of HF dip progression

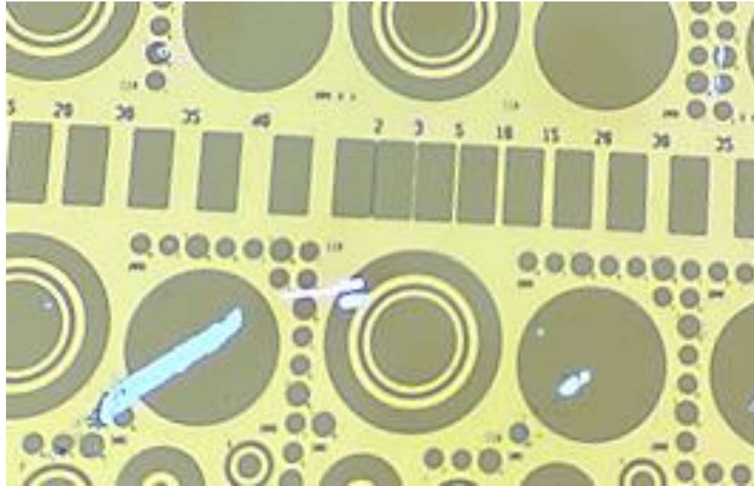

Figure 5.4.21: Optical microscopy of sample surface prior to wet etching

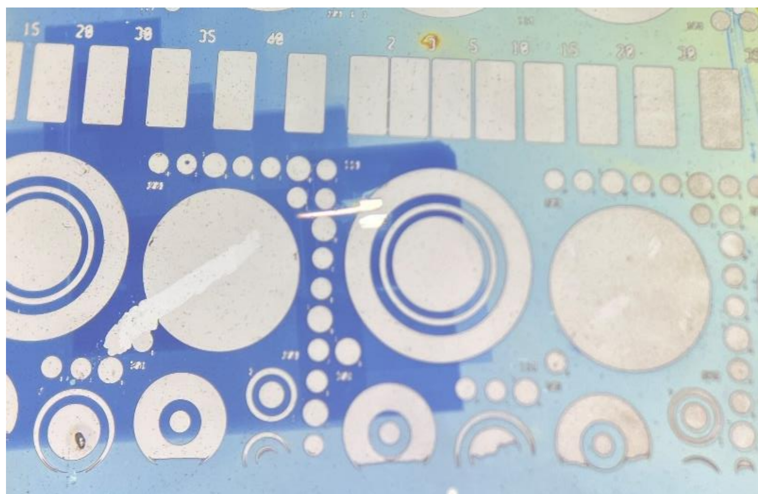

Figure 5.4.22: Optical microscopy of sample surface after 9 mins etch

Figure 5.4.23: Optical microscopy of sample surface after 15 mins etch

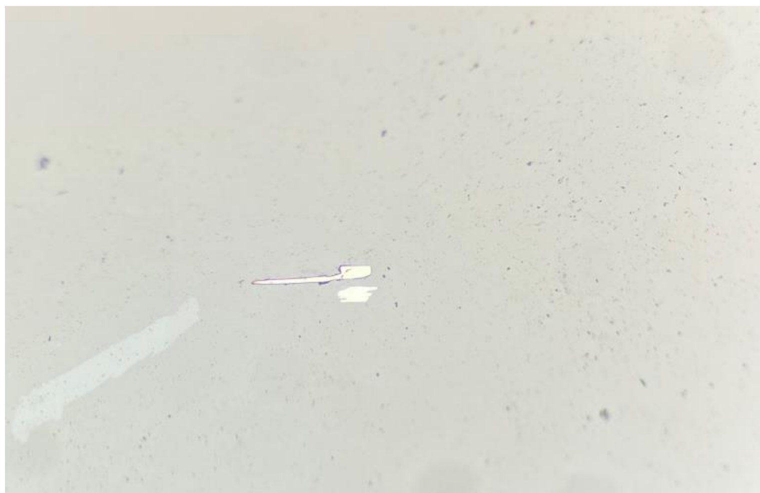

Figure 5.4.24: Optical microscopy of sample surface after 25 mins etch

5.5 Conclusions

Cleaned diamond substrates were first investigated to reveal the presence of any surface defects, and to confirm the orientation. About 400 nm of silicon dioxide was deposited on the sample and trenches were etched in the oxide using a TLM contact mask in preparation for selective area deposition of nanocarbon. After deposition, color changes in the trenches

suggested the presence of the material in the cavities and elemental analysis confirmed that it was some form of carbon. FIB-SEM results and etching provided further evidence that the nanoC had been selectively grown even though the results from Raman spectroscopy were inconclusive due to issues with the thickness of the film.

5.6 References

[1] Akiki, G., Frégnaux, M., Florea, I., Bulkin, P., Daineka, D., Filonovich, S., ... & Johnson, E. V. (2021). Origin of area selective plasma enhanced chemical vapor deposition of microcrystalline silicon. *Journal of Vacuum Science & Technology A: Vacuum, Surfaces, and Films*, *39*(1), 013201.

[2] Alam, M. A., People, R., Isaacs, E., Kim, C. Y., Evans-Lutterodt, K., Siegrist, T., ... & Hybertsen, M. S. (1999). Simulation and characterization of the selective area growth process. *Applied physics letters*, *74*(18), 2617-2619.

[3] Gladfelter, W. L. (1993). Selective metalization by chemical vapor deposition. *Chemistry of materials*, *5*(10), 1372-1388.

[4] Parsons, G. N., & Clark, R. D. (2020). Area-selective deposition: Fundamentals, applications, and future outlook. *Chemistry of Materials*, *32*(12), 4920-4953.

[5] Ducati, C., Alexandrou, I., Chhowalla, M., Amaratunga, G. A., & Robertson, J. (2002). Temperature selective growth of carbon nanotubes by chemical vapor deposition. *Journal of Applied Physics*, *92*(6), 3299-3303.

[6] Hampden-Smith, M. J., & Kodas, T. T. (1995). Chemical vapor deposition of metals: Part 2. Overview of selective CVD of Metals. *Chemical Vapor Deposition*, *1*(2), 39-48.

[7] Mokari, T., Rothenberg, E., Popov, I., Costi, R., & Banin, U. (2004). Selective growth of metal tips onto semiconductor quantum rods and tetrapods. *Science*, *304*(5678), 1787-1790.

[8] Alam, M. A., People, R., Isaacs, E., Kim, C. Y., Evans-Lutterodt, K., Siegrist, T., ... & Hybertsen, M. S. (1999). Simulation and characterization of the selective area growth process. *Applied physics letters*, *74*(18), 2617-2619.

[9] Chang, A. S., Li, B., Wang, S., Frisone, S., Goldman, R. S., Han, J., & Lauhon, L. J. (2022). Unveiling the influence of selective-area-regrowth interfaces on local electronic properties of GaN pn junctions for efficient power devices. *Nano Energy*, *102*, 107689.

[10] Liu, F., Shi, J., Xu, J., Han, N., Cheng, Y., & Huang, W. (2022). Site-selective growth of two-dimensional materials: strategies and applications. *Nanoscale*, *14*(28), 9946-9962.

[11]Kato, Y., Kitamura, S., Hiramatsu, K., & Sawaki, N. (1994). Selective growth of wurtzite GaN and AlxGa1− xN on GaN/sapphire substrates by metalorganic vapor phase epitaxy. *Journal of crystal growth*, *144*(3-4), 133-140.

[12] Umeno, M., & Adhikary, S. (2005). Diamond-like carbon thin films by microwave surface-wave plasma CVD aimed for the application of photovoltaic solar cells. *Diamond and Related Materials*, *14*(11-12), 1973-1979.

[13] Dwivedi, N., Kumar, S., Carey, J. D., Malik, H. K., & Govind. (2012). Photoconductivity and characterization of nitrogen incorporated hydrogenated amorphous carbon thin films. *Journal of Applied Physics*, *112*(11), 113706.

[14] Carey, J. D., Smith, R. C., & Silva, S. R. P. (2006). Carbon based electronic materials: applications in electron field emission. *Journal of Materials Science: Materials in Electronics*, *17*(6), 405-412.

[15] Silva, S. R. P., & Carey, J. D. (2003). Enhancing the electrical conduction in amorphous carbon and prospects for device applications. *Diamond and Related Materials*, *12*(2), 151-158.

[16] Carey, J. D., & Henley, S. J. (2007). Clustering in nanostructured carbon: Evidence of electron delocalization. *Diamond and Related Materials*, *16*(10), 1782-1787.

[17] Wang, F. M., Chen, M. W., & Lai, Q. B. (2010). Metallic contacts to nitrogen and boron doped diamond-like carbon films. *Thin Solid Films*, *518*(12), 3332-3336.

[18] Amonoo E., Jha V., Thornton T, Koeck F. A, Nemanich R. J., and Alford T. L.(2023) Ohmic Contacts to Nitrogen-Doped Nanocarbon Layers on Diamond (100) Surfaces. *Diamond and Related Materials, 135, 109832.*

[19] https://www.keyence.com/products/microscope/elemental-analyzer/ea-300/

CHAPTER 6

SUMMARY AND FUTURE WORKS

In the final conclusion, a new nanocrystalline diamond material was characterized and found to be an avenue for reducing the contact resistivity of phosphorus diamond films. The excellent conductivity of the film was largely attributed to the high concentration of nitrogen dopants, the presence of sp2 phases and defects and the formation of the carbide at the interface with titanium. However, a fundamental question which needs to be answered is the influence of annealing on the nanocarbon. Hence, a thorough study of the effect of annealing temperature on the grain size, morphology, and extent of possible graphitization is required to investigate the annealed nanocarbon's role in improving the contact resistivity.

Further, the contact properties of a lightly doped phosphorus-doped diamond sample was looked at and the lowest values were reported using Ti/Pt/Au. For future studies, it would be of interest to test different ranges of the concentration of lightly phosphorus-doped diamond samples to investigate if there is a critical concentration beyond which the mobility becomes undesirable and to investigate through SIMS, other contaminants during the doping process that limit/improve upon the conductivity of such films.

From the experiments done with hafnium as an alternative contact, it was largely realized that there was a significant amount of oxygen phases present on the surface which largely stemmed from the vacuum break when depositing hafnium and the subsequent metals platinum and gold. Therefore, it is recommended that a single tool, preferably a sputtering

tool capable of depositing all three metals under high vacuum, be used to prevent environmental exposure prior to encapsulation. Other studies to investigate hafnium include combinations of Hf/Au and the study of hafnium alone on the substrate to record the differences. Since hafnium and zirconium were suggested to have similar properties, it would be instructive to pursue a further look at how zirconium as a contact compares to titanium and hafnium and where its advantages can be utilized.

Lastly, nanoC was selectively grown in cavities created on a diamond substrate and many tests were carried out to confirm the presence of the nanocarbon. There was some proof for the material, but other tests were inconclusive since the film's thickness limited the study's evidence. Therefore, a more detailed analysis is recommended by repeating the experiment for a thicker nanoC film to eliminate the problems arising from thickness. After a thick film is used to confirm the growth, a doped diamond substrate needs to be used, contact metals deposited on it after the growth, and electrical studied be carried out to extract the properties on the doped diamond.

REFERENCES

Chapter 1

[1] Siu, C. (2022). Semiconductor physics. In *Electronic Devices, Circuits, and Applications* (pp. 35-39). Springer, Cham.

[2] Wort, C. J., & Balmer, R. S. (2008). Diamond as an electronic material. *Materials today*, *11*(1-2), 22-28.

[3] Geis, M. W. (1991). Diamond transistor performance and fabrication. *Proceedings of the IEEE*, *79*(5), 669-676.

[4] Matsumoto, T., Kato, H., Tokuda, N., Makino, T., Ogura, M., Takeuchi, D., ... & Yamasaki, S. (2014). Reduction of n-type diamond contact resistance by graphite electrode. *physica status solidi (RRL)–Rapid Research Letters*, *8*(2), 137-140.

[5] Kato, H., Umezawa, H., Tokuda, N., Takeuchi, D., Okushi, H., & Yamasaki, S. (2008). Low specific contact resistance of heavily phosphorus-doped diamond film. *Applied Physics Letters*, *93*(20), 202103

[6] Kato, H., Takeuchi, D., Tokuda, N., Umezawa, H., Okushi, H., & Yamasaki, S. (2009). Characterization of specific contact resistance on heavily phosphorus-doped diamond films. *Diamond and Related Materials*, *18*(5-8), 782-785

[7] Kato, H., Makino, T., Ogura, M., Tokuda, N., Okushi, H., & Yamasaki, S. (2009). Selective growth of buried n+ diamond on (001) phosphorus-doped n-type diamond film. *Applied Physics Express*, *2*(5), 055502.

[8] Teraji, T., Katagiri, M., Koizumi, S., Ito, T., & Kanda, H. (2003). Ohmic contact formation for N-type diamond by selective doping. *Japanese journal of applied physics*, *42*(8A), L882.

[9] Teraji, T., Koizumi, S., & Kanda, H. (2000). Ga ohmic contact for n-type diamond by ion implantation. *Applied Physics Letters*, *76*(10), 1303-1305.

[10] https://www.msesupplies.com/products/10-x-10-x-0-5-mm-n-type-p-doped-prime-grade-silicon-wafer-100-ssp-1-10-ohm-cm?variant=32215176249402

[11] Kalish, R. (1999). Doping of diamond. *Carbon*, *37*(5), 781-785.

[12] Teraji, T., Koizumi, S., Mita, S., Sawabe, A., & Kanda, H. (1999). Electrical contacts for n-type diamond. *Japanese journal of applied physics*, *38*(10A), L1096

[13] Dani, I., Mäder, G., Grabau, P., Dresler, B., Linaschke, D., Lopez, E., ... & Beyer, E. (2009). Atmospheric-Pressure Plasmas for Solar Cell Manufacturing. *Contributions to Plasma Physics*, *49*(9), 662-670.

[14] Nastasi, M. A., & Mayer, J. W. (2006). *Ion implantation and synthesis of materials* (Vol. 80). Berlin: Springer

[15] Kalish, R. (1997). Ion implantation in diamond; damage, annealing and doping. In *The Physics of Diamond* (pp. 373-409). IOS Press.

[16] Ran B. Technion-Israel Institute of Technology, M.Sc. thesis, 1997, unpublished

[17] Koizumi, S., Teraji, T., & Kanda, H. (2000). Phosphorus-doped chemical vapor deposition of diamond. *Diamond and Related Materials*, *9*(3-6), 935-940.

[18] Suzuki, M., Yoshida, H., Sakuma, N., Ono, T., Sakai, T., & Koizumi, S. (2004). Electrical characterization of phosphorus-doped n-type homoepitaxial diamond layers by Schottky barrier diodes. *Applied physics letters*, *84*(13), 2349-2351.

[19] Kato, H., Makino, T., Yamasaki, S., & Okushi, H. (2007). n-type diamond growth by phosphorus doping on (0 0 1)-oriented surface. *Journal of Physics D: Applied Physics*, *40*(20), 6189.

[20] Umeno, M., & Adhikary, S. (2005). Diamond-like carbon thin films by microwave surface-wave plasma CVD aimed for the application of photovoltaic solar cells. *Diamond and Related Materials*, *14*(11-12), 1973-1979.

[21] Dwivedi, N., Kumar, S., Carey, J. D., Malik, H. K., & Govind. (2012). Photoconductivity and characterization of nitrogen incorporated hydrogenated amorphous carbon thin films. *Journal of Applied Physics*, *112*(11), 113706.

[22] Carey, J. D., Smith, R. C., & Silva, S. R. P. (2006). Carbon based electronic materials: applications in electron field emission. *Journal of Materials Science: Materials in Electronics*, *17*(6), 405-412.

[23] Silva, S. R. P., & Carey, J. D. (2003). Enhancing the electrical conduction in amorphous carbon and prospects for device applications. *Diamond and Related Materials*, *12*(2), 151-158.

[24] Carey, J. D., & Henley, S. J. (2007). Clustering in nanostructured carbon: Evidence of electron delocalization. *Diamond and Related Materials*, *16*(10), 1782-1787.

[25] Wang, F. M., Chen, M. W., & Lai, Q. B. (2010). Metallic contacts to nitrogen and boron doped diamond-like carbon films. *Thin Solid Films*, *518*(12), 3332-3336.

[26] Schroder, D. K. (2015). *Semiconductor material and device characterization*. John Wiley & Sons.

Chapter 2

[1] Umeno, M., & Adhikary, S. (2005). Diamond-like carbon thin films by microwave surface-wave plasma CVD aimed for the application of photovoltaic solar cells. *Diamond and Related Materials*, *14*(11-12), 1973-1979.

[2] Dwivedi, N., Kumar, S., Carey, J. D., Malik, H. K., & Govind. (2012). Photoconductivity and characterization of nitrogen incorporated hydrogenated amorphous carbon thin films. *Journal of Applied Physics*, *112*(11), 113706.

[3] Carey, J. D., Smith, R. C., & Silva, S. R. P. (2006). Carbon based electronic materials: applications in electron field emission. *Journal of Materials Science: Materials in Electronics*, *17*(6), 405-412.

[4] Silva, S. R. P., & Carey, J. D. (2003). Enhancing the electrical conduction in amorphous carbon and prospects for device applications. *Diamond and Related Materials*, *12*(2), 151-158.

[5] Carey, J. D., & Henley, S. J. (2007). Clustering in nanostructured carbon: Evidence of electron delocalization. *Diamond and Related Materials*, *16*(10), 1782-1787.

[6] Wang, F. M., Chen, M. W., & Lai, Q. B. (2010). Metallic contacts to nitrogen and boron doped diamond-like carbon films. *Thin Solid Films*, *518*(12), 3332-3336.

[7] Inaba, M., Seki, A., Sato, K., Kushida, T., Kageura, T., Yamano, H., ... & Kawarada, H. (2017). Vertical edge graphite layer on recovered diamond (001) after high-dose ion implantation and high-temperature annealing (Phys. Status Solidi B 9/2017). *physica status solidi (b)*, *254*(9), 1770249.

[8] Mizuno, Y., Ito, Y., & Ueda, K. (2021). Optoelectronic synapses using vertically aligned graphene/diamond heterojunctions. *Carbon*, *182*, 669-676.

[9] Melezhyk, A. V., Yanchenko, V. V., & Sementsov, Y. I. (2007). Nanocarbon *Materials. In Hydrogen Materials Science and Chemistry of Carbon Nanomaterials (pp. 529-537). Springer, Dordrecht.*

[10] Awasthi, K., Kumar, R., Raghubanshi, H., Awasthi, S., Pandey, R., Singh, D., & Srivastava, O. N. (2011). Synthesis of nano-carbon (nanotubes, nanofibres, graphene) materials. *Bulletin of Materials Science*, *34*(4), 607-614.

[11] Nambo, M., & Itami, K. (2009). Synthesis of new nano-carbon materials. *Access Science*.

[12] Williams, O. A. (2006). Ultrananocrystalline diamond for electronic applications. *Semiconductor Science and Technology*, *21*(8), R49.

[13] Gerbi, J. E., Auciello, O., Birrell, J., Gruen, D. M., Alphenaar, B. W., & Carlisle, J. A. (2003). Electrical contacts to ultrananocrystalline diamond. *Applied Physics Letters*, *83*(10), 2001-2003.

[14] Williams, O. A., Curat, S., Gerbi, J. E., Gruen, D. M., & Jackman, R. B. (2004). n-Type conductivity in ultrananocrystalline diamond films. *Applied Physics Letters*, *85*(10), 1680-1682.

[15] Birrell, J., Carlisle, J. A., Auciello, O., Gruen, D. M., & Gibson, J. M. (2002). Morphology and electronic structure in nitrogen-doped ultrananocrystalline diamond. *Applied Physics Letters*, *81*(12), 2235-2237.

[16] F.A. Koeck, and R.J. Nemanich, "Contact structures for n-type diamond." U.S. Patent 11,380,763.

[17] Koeck, F. A., Benipal, M., & Nemanich, R. J. (2020). Electrical contact considerations for diamond electron emission diodes. *Diamond and Related Materials*, *101*, 107607.

[18] Shimoda, N., Kato, Y., & Teii, K. (2016). Electrical contacts to nanocrystalline diamond films studied at high temperatures. *Journal of Applied Physics*, *120*(23), 235706.

[19] Liu, Y. K., Tso, P. L., Pradhan, D., Lin, I. N., Clark, M., & Tzeng, Y. (2005). Structural and electrical properties of nanocrystalline diamond (NCD) heavily doped by nitrogen. *Diamond and Related Materials*, *14*(11-12), 2059-2063.

[20] Chen, Q., Gruen, D. M., Krauss, A. R., Corrigan, T. D., Witek, M., & Swain, G. M. (2001). The structure and electrochemical behavior of nitrogen-containing nanocrystalline diamond films deposited from CH4/N2/Ar mixtures. *Journal of The Electrochemical Society*, *148*(1), E44.

[21] Segawa, Y., Levine, D. R., & Itami, K. (2019). Topologically unique molecular nanocarbons. *Accounts of chemical research*, *52*(10), 2760-2767.

[22] Schroder, D. K. (2015). *Semiconductor material and device characterization*. John Wiley & Sons.

[23] Cullity, B. D., & Stock, S. R. (2001). *Elements of X-ray Diffraction, Third Edition*. Prentice-Hall.

[24] Yu, J., Liu, G., Sumant, A. V., Goyal, V., & Balandin, A. A. (2012). Graphene-on-diamond devices with increased current-carrying capacity: carbon sp2-on-sp3 technology. *Nano letters*, *12*(3), 1603-1608.

[25] Kaniyoor, A., & Ramaprabhu, S. (2012). A Raman spectroscopic investigation of graphite oxide derived graphene. *Aip Advances*, *2*(3), 032183.

[26] Tuinstra, F., & Koenig, J. L. (1970). Raman spectrum of graphite. *The Journal of Chemical Physics*, *53*(3), 1126-1130.

[27] Kudin, K. N., Ozbas, B., Schniepp, H. C., Prud'Homme, R. K., Aksay, I. A., & Car, R. (2008). Raman spectra of graphite oxide and functionalized graphene sheets. *Nano Letters*, *8*(1), 36-41.

[28] Nemanich, R. J., & Solin, S. A. (1979). First-and second-order Raman scattering from finite-size crystals of graphite. *Physical Review B*, *20*(2), 392.

[29] Tachibana, T., Williams, B. E., & Glass, J. T. (1992). Correlation of the electrical properties of metal contacts on diamond films with the chemical nature of the metal-diamond interface. II. Titanium contacts: A carbide-forming metal. *Physical Review B*, *45*(20), 11975.

[30] H. M. Johnson, J. M. Brown, A. M. Zaniewski, R. J. Nemanich, Cleaning diamond surfaces via oxygen plasma inhibits the formation of a TiC interface, Diamond and Related Materials 126, 109058 (2022).

[31] Achatz, P., Williams, O. A., Bruno, P., Gruen, D. M., Garrido, J. A., & Stutzmann, M. (2006). Effect of nitrogen on the electronic properties of ultrananocrystalline diamond thin films grown on quartz and diamond substrates. *Physical Review B*, *74*(15), 155429.

[32] Grover, S., Sahu, S., Zhang, P., Davis, K. O., & Kurinec, S. K. (2020, May). Standardization of specific contact resistivity measurements using transmission line model (TLM). In *2020 IEEE 33rd International Conference on Microelectronic Test Structures (ICMTS)* (pp. 1-6). IEEE.

Chapter 3

[1] Teraji, T., Koizumi, S., Mita, S., Sawabe, A., & Kanda, H. (1999). Electrical contacts for n-type diamond. *Japanese journal of applied physics*, *38*(10A), L1096

[2] Kato, H., Oyama, K., Makino, T., Ogura, M., Takeuchi, D., & Yamasaki, S. (2012). Diamond bipolar junction transistor device with phosphorus-doped diamond base layer. *Diamond and related materials*, *27*, 19-22.

[3] Moazed, K. L., Nguyen, R., & Zeidler, J. R. (1988). Ohmic contacts to semiconducting diamond. *IEEE electron device letters*, *9*(7), 350-351.

[4] Kato, H., Umezawa, H., Tokuda, N., Takeuchi, D., Okushi, H., & Yamasaki, S. (2008). Low specific contact resistance of heavily phosphorus-doped diamond film. *Applied Physics Letters*, *93*(20), 202103

[5] Shimaoka, T., Liao, M., & Koizumi, S. (2022). n-Type Diamond Metal-Semiconductor Field-Effect Transistor with High Operation Temperature of 300° C. *IEEE Electron Device Letters*, *43*(4), 588-591.

[6] Kato, H., Takeuchi, D., Tokuda, N., Umezawa, H., Okushi, H., & Yamasaki, S. (2009). Characterization of specific contact resistance on heavily phosphorus-doped diamond films. *Diamond and Related Materials*, *18*(5-8), 782-785

[7] Arora, N. D., Hauser, J. R., & Roulston, D. J. (1982). Electron and hole mobilities in silicon as a function of concentration and temperature. *IEEE Transactions on electron devices*, *29*(2), 292-295.

[8] Gross, W. J., Vasileska, D., & Ferry, D. K. (1999). A novel approach for introducing the electron-electron and electron-impurity interactions in particle-based simulations. *IEEE Electron Device Letters*, *20*(9), 463-465.

[9] Nesladek, M. (2005). Conventional n-type doping in diamond: state of the art and recent progress. *Semiconductor Science and Technology*, *20*(2), R19.

[10] Koizumi, S., Kamo, M., Sato, Y., Ozaki, H., & Inuzuka, T. (1997). Growth and characterization of phosphorous doped {111} homoepitaxial diamond thin films. *Applied Physics Letters*, *71*(8), 1065-1067.

[11] Katagiri, M., Isoya, J., Koizumi, S., & Kanda, H. (2004). Lightly phosphorus-doped homoepitaxial diamond films grown by chemical vapor deposition. *Applied physics letters*, *85*(26), 6365-6367.

[12] Kato, H., Makino, T., Yamasaki, S., & Okushi, H. (2007). n-type diamond growth by phosphorus doping on (0 0 1)-oriented surface. *Journal of Physics D: Applied Physics*, *40*(20), 6189.

[13] Teraji, T., Koizumi, S., & Kanda, H. (2000). Ga Ohmic contact for n-type diamond by ion implantation. *Applied Physics Letters*, *76*(10), 1303-1305.

[14] Teraji, T., Katagiri, M., Koizumi, S., Ito, T., & Kanda, H. (2003). Ohmic contact formation for N-type diamond by selective doping. *Japanese journal of applied physics*, *42*(8A), L882.

[15] Takemasa, A., Kakushima, K., Sugii, N., Nishiyama, A., Tsutsui, K., Natori, K., & Iwai, H. (2014). Electrical characteristics of n-type

[16] Schroder, D. K. (2015). *Semiconductor material and device characterization*. John Wiley & Sons.

[17] Chen, Y., Ogura, M., Yamasaki, S., & Okushi, H. (2005). Ohmic contacts on p-type homoepitaxial diamond and their thermal stability. *Semiconductor science and technology*, *20*(8), 860

[18] Kato, H., Futako, W., Yamasaki, S., & Okushi, H. (2004). Homoepitaxial growth and characterization of phosphorus-doped diamond using tertiarybutylphosphine as a doping source. *Diamond and related materials*, *13*(11-12), 2117-2120.

[19] Mircea, A., Ougazzaden, A., & Mellet, R. (1989). Very uniform epitaxy. *Progress in crystal growth and characterization*, *19*(1-2), 39-49.

[20] Benda, H., & Spenke, E. (1967). Reverse recovery processes in silicon power rectifiers. *Proceedings of the IEEE*, *55*(8), 1331-1354.

[21] Hu, C. (1979). Optimum doping profile for minimum Ohmic resistance and high-breakdown voltage. *IEEE Transactions on Electron Devices*, *26*(3), 243-244.

[22] Todeschini, M., Bastos da Silva Fanta, A., Jensen, F., Wagner, J. B., & Han, A. (2017). Influence of Ti and Cr adhesion layers on ultrathin Au films. *ACS applied materials & interfaces*, *9*(42), 37374-37385.

[23] Cordill, M. J., Bahr, D. F., Moody, N. R., & Gerberich, W. W. (2004). Recent developments in thin film adhesion measurement. IEEE Transactions on Device and Materials Reliability, 4(2), 163-168.

[24] Agarwal, S., Prajapati, Y. K., & Maurya, J. B. (2016). Effect of metallic adhesion layer thickness on surface roughness for sensing application. IEEE Photonics Technology Letters, 28(21), 2415-2418.

[25] Werner, M. (2003). Diamond metallization for device applications. Semiconductor science and technology, 18(3), S41.

[26] Tachibana, T., Williams, B. E., & Glass, J. T. (1992). Correlation of the electrical properties of metal contacts on diamond films with the chemical nature of the metal-diamond interface. II. Titanium contacts: A carbide-forming metal. Physical Review B, 45(20), 11975.

[27] Lavrenko, V. A., Glebov, L. A., Pomitkin, A. P., Chuprina, V. G., & Protsenko, T. G. (1975). High-temperature oxidation of titanium carbide in oxygen. Oxidation of Metals, 9(2), 171-179.

[28] Leroy, W. P., Detavernier, C., Van Meirhaeghe, R. L., Kellock, A. J., & Lavoie, C. (2006). Solid-state formation of titanium carbide and molybdenum carbide as contacts for carbon-containing semiconductors. Journal of applied physics, 99(6), 063704.

[29] Gildenblat, G. S., Grot, S. A., Hatfield, C. W., Badzian, A. R., & Badzian, T. (1990). High-temperature Schottky diodes with thin-film diamond base. IEEE electron device letters, 11(9), 371-372.

[30] Fullman, R. L., & Fisher, J. C. (1951). Formation of annealing twins during grain growth. Journal of Applied Physics, 22(11), 1350-1355.

[31] Ralph, B. (1990). Grain growth. Materials Science and Technology, 6(11), 1136-1144.

[32] Thompson, C. V. (1990). Grain growth in thin films. Annual review of materials science, 20(1), 245-268.

[33] Sarah, M. S. P., Musa, M. Z., Asiah, M. N., & Rusop, M. (2010, April). Electrical conductivity characteristics of TiO 2 thin film. In 2010 International Conference on Electronic Devices, Systems and Applications (pp. 361-364). IEEE.

[34] Tenny, K. M., & Keenaghan, M. (2017). Ohms Law.

[35] Kato, H., Makino, T., Ogura, M., Tokuda, N., Okushi, H., & Yamasaki, S. (2009). Selective growth of buried n+ diamond on (001) phosphorus-doped n-type diamond film. Applied Physics Express, 2(5), 05550

Chapter 4

[1] Holloway, P. H. (1979). Gold/chromium metallizations for electronic devices: Manufacturing technology and behaviour. *Gold Bulletin*, *12*(3), 99-106.

[2] Saijo, K., Yagi, M., Shibuki, K., & Takatsu, S. (1990). The improvement of the adhesion strength of diamond films. *Surface and Coatings Technology*, *43*, 30-40.

[3] May, P. W., Regan, E. M., Taylor, A., Uney, J., Dick, A. D., & McGeehan, J. (2012). Spatially controlling neuronal adhesion on CVD diamond. *Diamond and related materials*, *23*, 100-104.

[4] Peng, X. L., & Clyne, T. W. (1997). Formation and adhesion of hot filament CVD diamond films on titanium substrates. *Thin solid films*, *293*(1-2), 261-269.

[5] Buccioni, E., Braca, E., Kenny, J. M., & Terranova, M. L. (1999). Processing–structure–adhesion relationship in CVD diamond films on titanium substrates. *Diamond and related materials*, *8*(1), 17-24.

[6] Biener, M. M., Biener, J., Kucheyev, S. O., Wang, Y. M., El-Dasher, B., Teslich, N. E., … & Wild, C. (2010). Controlled incorporation of mid-to-high Z transition metals in CVD diamond. *Diamond and related materials*, *19*(5-6), 643-647.

[7] Iacovangelo, C. D. (1996). Thermal stability of metallized CVD diamond. *Thin Solid Films*, *286*(1-2), 264-269.

[8] Hwu, H. H., & Chen, J. G. (2005). Surface chemistry of transition metal carbides. *Chemical reviews*, *105*(1), 185-212.

[9] Viñes, F., Sousa, C., Liu, P., Rodriguez, J. A., & Illas, F. (2005). A systematic density functional theory study of the electronic structure of bulk and (001) surface of transition-metals carbides. *The Journal of chemical physics*, *122*(17), 174709.

[10] Tachibana, T., Williams, B. E., & Glass, J. T. (1992). Correlation of the electrical properties of metal contacts on diamond films with the chemical nature of the metal-diamond interface. II. Titanium contacts: A carbide-forming metal. Physical Review B, 45(20), 11975.

[11] Lavrenko, V. A., Glebov, L. A., Pomitkin, A. P., Chuprina, V. G., & Protsenko, T. G. (1975). High-temperature oxidation of titanium carbide in oxygen. Oxidation of Metals, 9(2), 171-179.

[12] Leroy, W. P., Detavernier, C., Van Meirhaeghe, R. L., Kellock, A. J., & Lavoie, C. (2006). Solid-state formation of titanium carbide and molybdenum carbide as contacts for carbon-containing semiconductors. Journal of applied physics, 99(6), 063704.

[13] https://www.acs.org/education/whatischemistry/periodictable.html

[14] Cappelli, E., Bellucci, A., Orlando, S., Trucchi, D. M., Mezzi, A., & Valentini, V. (2013). PLD deposition of tungsten carbide contact for diamond photodiodes. Influence of process conditions on electronic and chemical aspects. *Applied surface science*, *278*, 111-116.

[15] Vardi, A., Tordjman, M., Kalish, R., & del Alamo, J. A. (2020). Refractory W ohmic contacts to H-terminated diamond. *IEEE Transactions on Electron Devices*, *67*(9), 3516-3521.

[16] Teraji, T., Garino, Y., Koide, Y., & Ito, T. (2009). Low-leakage p-type diamond Schottky diodes prepared using vacuum ultraviolet light/ozone treatment.

[17] Xing, K., Tsai, A., Rubanov, S., Creedon, D. L., Yianni, S. A., Zhang, L., … & Qi, D. C. (2020). Palladium forms Ohmic contact on hydrogen-terminated diamond down to 4 K. *Applied Physics Letters*, *116*(11), 111601.

[18] Fang, F. A. N. G., Hewett, C. A., Fernandes, M. G., & Lau, S. S. (1989). Ohmic contacts formed by ion mixing in the Si-diamond system. *IEEE transactions on electron devices*, *36*(9), 1783-1786.

[19] Drozdov, M. N., Arkhipova, E. A., Drozdov, Y. N., Kraev, S. A., Shashkin, V. I., Parafin, A. E. E., … & Bogdanov, S. A. (2020). The use of pulsed laser annealing to form ohmic Mo/Ti contacts to diamond. *Technical Physics Letters*, *46*, 551-555.

[20] Das, K., Venkatesan, V., Miyata, K., Dreifus, D. L., & Glass, J. T. (1992). A review of the electrical characteristics of metal contacts on diamond. *Thin Solid Films*, *212*(1-2), 19-24.

[21] Venkatesan, V., & Das, K. (1992). Ohmic contacts on diamond by B ion implantation and Ti-Au metallization. *IEEE electron device letters*, *13*(2), 126-128.

[22] Jingu, Y., Hirama, K., & Kawarada, H. (2010). Ultrashallow TiC source/drain contacts in diamond MOSFETs formed by hydrogenation-last approach. *IEEE transactions on electron devices*, *57*(5), 966-972.

[23] Mphahlele, M. R., Olubambi, P. A., & Olevsky, E. A. (2023). Advances in Sintering of Titanium Aluminide: A Review. *JOM*, 1-20.

[24] Imura, M., Hayakawa, R., Ohsato, H., Watanabe, E., Tsuya, D., Nagata, T., … & Amano, H. (2012). Development of AlN/diamond heterojunction field effect transistors. *Diamond and related materials*, *24*, 206-209.

[25] Ottaviani, G., Tu, K. N., & Mayer, J. W. (1980). Interfacial reaction and Schottky barrier in metal-silicon systems. *Physical Review Letters*, *44*(4), 284.

[26] Andrews, J. M., & Phillips, J. C. (1975). Chemical bonding and structure of metal-semiconductor interfaces. *Physical Review Letters*, *35*(1), 56.

[27] Niessen, A. K., & De Boer, F. R. (1981). The enthalpy of formation of solid borides, carbides, nitrides, silicides and phosphides of transition and noble metals. *Journal of the Less common Metals*, *82*, 75-80.

[28] Schemel, J. H. (1977). *ASTM manual on zirconium and hafnium* (No. 639). Astm International.

[29] H. Nielsen, R., H. Schlewitz, J., Nielsen, H., & Updated by Staff. (2000). Zirconium and zirconium compounds. *Kirk-Othmer Encyclopedia of Chemical Technology*, 1-46.

[30] Hans, K., Latha, S., Bera, P., & Barshilia, H. C. (2018). Hafnium carbide based solar absorber coatings with high spectral selectivity. *Solar Energy Materials and Solar Cells*, *185*, 1-7.

[31] F.A. Koeck, and R.J. Nemanich, "Contact structures for n-type diamond." U.S. Patent 11,380,763.

[32] Koeck, F. A., Benipal, M., & Nemanich, R. J. (2020). Electrical contact considerations for diamond electron emission diodes. *Diamond and Related Materials*, *101*, 107607.

[33] Amonoo E., Jha V., Thornton T, Koeck F. A, Nemanich R. J., and Alford T. L.(2023) Ohmic Contacts to Nitrogen-Doped Nanocarbon Layers on Diamond (100) Surfaces. *Diamond and Related Materials, 135, 109832.*

[34] Birrell, J., Carlisle, J. A., Auciello, O., Gruen, D. M., & Gibson, J. M. (2002). Morphology and electronic structure in nitrogen-doped ultrananocrystalline diamond. *Applied Physics Letters*, *81*(12), 2235-2237.

[35] Gerbi, J. E., Auciello, O., Birrell, J., Gruen, D. M., Alphenaar, B. W., & Carlisle, J. A. (2003). Electrical contacts to ultrananocrystalline diamond. *Applied Physics Letters*, *83*(10), 2001-2003.

Chapter 5

[1] Akiki, G., Frégnaux, M., Florea, I., Bulkin, P., Daineka, D., Filonovich, S., ... & Johnson, E. V. (2021). Origin of area selective plasma enhanced chemical vapor deposition of microcrystalline silicon. *Journal of Vacuum Science & Technology A: Vacuum, Surfaces, and Films*, *39*(1), 013201.

[2] Alam, M. A., People, R., Isaacs, E., Kim, C. Y., Evans-Lutterodt, K., Siegrist, T., ... & Hybertsen, M. S. (1999). Simulation and characterization of the selective area growth process. *Applied physics letters*, *74*(18), 2617-2619.

[3] Gladfelter, W. L. (1993). Selective metalization by chemical vapor deposition. *Chemistry of materials*, *5*(10), 1372-1388.

[4] Parsons, G. N., & Clark, R. D. (2020). Area-selective deposition: Fundamentals, applications, and future outlook. *Chemistry of Materials*, *32*(12), 4920-4953.

[5] Ducati, C., Alexandrou, I., Chhowalla, M., Amaratunga, G. A., & Robertson, J. (2002). Temperature selective growth of carbon nanotubes by chemical vapor deposition. *Journal of Applied Physics*, *92*(6), 3299-3303.

[6] Hampden-Smith, M. J., & Kodas, T. T. (1995). Chemical vapor deposition of metals: Part 2. Overview of selective CVD of Metals. *Chemical Vapor Deposition*, *1*(2), 39-48.

[7] Mokari, T., Rothenberg, E., Popov, I., Costi, R., & Banin, U. (2004). Selective growth of metal tips onto semiconductor quantum rods and tetrapods. *Science*, *304*(5678), 1787-1790.

[8] Alam, M. A., People, R., Isaacs, E., Kim, C. Y., Evans-Lutterodt, K., Siegrist, T., ... & Hybertsen, M. S. (1999). Simulation and characterization of the selective area growth process. *Applied physics letters*, *74*(18), 2617-2619.

[9] Chang, A. S., Li, B., Wang, S., Frisone, S., Goldman, R. S., Han, J., & Lauhon, L. J. (2022). Unveiling the influence of selective-area-regrowth interfaces on local electronic properties of GaN pn junctions for efficient power devices. *Nano Energy*, *102*, 107689.

[10] Liu, F., Shi, J., Xu, J., Han, N., Cheng, Y., & Huang, W. (2022). Site-selective growth of two-dimensional materials: strategies and applications. *Nanoscale*, *14*(28), 9946-9962.

[11]Kato, Y., Kitamura, S., Hiramatsu, K., & Sawaki, N. (1994). Selective growth of wurtzite GaN and AlxGa1− xN on GaN/sapphire substrates by metalorganic vapor phase epitaxy. *Journal of crystal growth*, *144*(3-4), 133-140.

[12] Umeno, M., & Adhikary, S. (2005). Diamond-like carbon thin films by microwave surface-wave plasma CVD aimed for the application of photovoltaic solar cells. *Diamond and Related Materials*, *14*(11-12), 1973-1979.

[13] Dwivedi, N., Kumar, S., Carey, J. D., Malik, H. K., & Govind. (2012). Photoconductivity and characterization of nitrogen incorporated hydrogenated amorphous carbon thin films. *Journal of Applied Physics*, *112*(11), 113706.

[14] Carey, J. D., Smith, R. C., & Silva, S. R. P. (2006). Carbon based electronic materials: applications in electron field emission. *Journal of Materials Science: Materials in Electronics*, *17*(6), 405-412.

[15] Silva, S. R. P., & Carey, J. D. (2003). Enhancing the electrical conduction in amorphous carbon and prospects for device applications. *Diamond and Related Materials*, *12*(2), 151-158.

[16] Carey, J. D., & Henley, S. J. (2007). Clustering in nanostructured carbon: Evidence of electron delocalization. *Diamond and Related Materials*, *16*(10), 1782-1787.

[17] Wang, F. M., Chen, M. W., & Lai, Q. B. (2010). Metallic contacts to nitrogen and boron doped diamond-like carbon films. *Thin Solid Films*, *518*(12), 3332-3336.

[18] Amonoo E., Jha V., Thornton T, Koeck F. A, Nemanich R. J., and Alford T. L.(2023) Ohmic Contacts to Nitrogen-Doped Nanocarbon Layers on Diamond (100) Surfaces. *Diamond and Related Materials, 135, 109832.*

[19] https://www.keyence.com/products/microscope/elemental-analyzer/ea-300/

APPENDIX A

PERMISSION STATEMENT FROM CO-AUTHORS

All co-authors that contributed to the different published and unpublished works have granted their full permission for the information to be included in this thesis document.